

# 國立交通大學

電子物理研究所

## 博士論文

運用掃描式探針微影技術研發製作矽質奈米元件結構

Silicon nanofabrication with scanning probe lithography technique

研究生：吳家豪

指導教授：許鈺宗 教授

趙天生 教授

中華民國九十六年六月

運用掃描式探針微影技術研發製作矽質奈米元件結構

Silicon nanofabrication with scanning probe lithography technique

研究生：吳家豪

Student : Chia-Hao Wu

指導教授：許鈺宗

Advisor : Jeng-Tzong Sheu

趙天生

Advisor : Tien-Sheng Chao

國立交通大學  
電子物理研究所  
博士論文



A Thesis  
Submitted to Institute of Electrophysics  
College of Science  
National Chiao Tung University  
in Partial Fulfillment of the Requirements  
for the Degree of  
Doctor of Philosophy  
in  
Electrophysics

June 2007

Hsinchu, Taiwan, Republic of China

中華民國 九十六 年 六 月

# 運用掃描式探針微影技術研發製作矽質奈米元件結構

學生：吳家豪

指導教授：許鈺宗 博士  
趙天生 博士

國立交通大學

電子物理研究所 博士班

摘 要



『奈米科技』已然成為全世界科技發展的重點之一，它亦將引發本世紀在材料、生化、光電、能源等等技術的革命，人類將可從此一先進研發科技中獲得豐碩的實際效益。近年來，奈米科技製程技術的研發受到許多研究團隊的高度重視，其中包含了發展製造奈米級元件結構的先進製作技術，以及設計研究開發新穎的奈米結構以因應未來前瞻性的領域應用。在眾多先進的微影技術當中，例如：電子束微影技術(EBL)，X 光微影技術(XRL)，以及掃描式探針微影技術(SPL)等技術，其中又以掃描式探針微影技術最具有製造奈米結構元件的潛力，因為此一先進微影技術不僅可應用於奈米尺度下將試片表面的特性轉變改質，並且可應用於製造生產所需的奈米級元件結構。掃描式探針微影技術乃是利用探針接近試片表面的時候，利用外加的電場誘發局部陽極氧化試片(抑或者是利用探針針尖的穿隧電流，來致使試片表面化學官能基分子層結構特性改質)，來製備奈米級元件結構。此種微影技術具有較高的解析度、精確的對準特性、以及可靠度高，也沒有一般微影的輻射熱損害，再加上製作簡易而且有著較低成本等等的優勢。本論文研究也將利用原子力顯微鏡掃描式探針沾附有機分子溶液，並藉由空氣中水分子當媒介，直接在矽質試片上進行奈米級分子層結構圖案的微影塗佈。此種奈米微影方式，探針就如同一隻筆，而有機溶液就如同墨水一般。

我們可以藉由此方式來塗佈製造出小於 100 奈米解析度的各式化學官能基分子層結構圖案。因此，掃描式探針微影技術被視為發展奈米元件的前瞻關鍵技術。在本論文中研究，我們在一維的矽質奈米導線上選擇性沈積金奈米粒子，並且將其應用於生物分子及相關的化學物質的感測研究，並將此一前瞻性的技術平台建構完成。矽質奈米導線乃是利用掃描式探針微影技術並結合非等向式四-甲基-氫氧化鈉 (TMAH) 濕式蝕刻 (或 RIE 乾式蝕刻) 來完成的。而 15 奈米粒徑大小的金奈米粒子乃是利用化學鹽類還原的方式來製備的。然後，我們結合運用掃描式探針微影技術與自我組裝分子層技術在矽質奈米導線的表面進行金奈米粒子的選擇性沈積。我們使用已沾附了 2-胺基-乙基-3-胺基丙烷三甲氧基矽化合物(AEAPTMS) 有機分子的掃描式探針，並藉由空氣中的水膜分子當作有機分子傳遞擴散的媒介，然後在矽質奈米導線上圖佈沈積有機分子層薄膜，當胺基的有機團修飾在矽質導線表面上時，便會使得矽質導線表面產生帶正離子的矽烷化改質效應。此外，本論文研究也成功地利用掃描式探針微影技術在二氧化矽表面利用 AFM 探針針尖的穿隧電流來致使試片表面 2-胺基乙基-3-胺基丙烷三甲氧基矽化合物(AEAPTMS)化學官能基有機分子層鍵結產生斷鍵而使試片表面改質。然後，藉由庫倫力的吸引作用，而與帶負電的金奈米粒子產生靜電吸附而沈積鍵結在矽質奈米導線上的矽烷化改質結構區域。我們深信此一前瞻性奈米製造技術藉由結合掃描式探針微影技術與自我組裝分子層技術所研發製造出的奈米結構元件，未來將可廣泛地應用於奈米電子元件與奈米生醫感測元件的研究領域，無論在學術及工業技術研究上皆極具價值。更重要的一點，本研究對於未來奈米級的電子元件製程技術的研發上，提供了一套操作容易且成本低廉的奈米元件製程研發技術。

# Silicon nanofabrication with scanning probe lithography technique

Student : Chia-Hao Wu

Advisors : Dr. Jeng-Tzong Sheu

Dr. Tien-Sheng Chao

Institute of Electrophysics

National Chiao Tung University

## ABSTRACT

One of the focal points that “nanotechnology” has already become development in science and technology of whole world. It will also cause the revolution in the technology, such as material, biochemistry, photo electricity, energy, etc. in this century. Mankind can obtain the actual benefit from this advanced nanotechnology. Recently, it is more interesting in research on nanotechnology, which includes the development of advanced manufacturing skills for fabricating nanometer size devices and the design and research of new nanometer structures for novel applications. Among these advanced lithography techniques, such as electron beam lithography, x-ray lithography and scanning probe lithography (SPL), etc., one potential approach for fabricating the nanostructures is the use of scanning probe lithography. SPL techniques have been used to perform nano-scaled surface modification, and dominated the research field of nano-structures fabrication. SPL, employing a conductive probe to induce electric-field-enhanced local anodic oxidation (or tunneling currents enhanced the surface modification of chemical functionality), provide its advantages of high resolution, alignment accuracy, high reliability, absence of radiation damage, simpler and lower-cost. We also utilize the AFM scanning tip as a “pen” to transport an “ink” containing organic molecules onto a substrate surface via a water meniscus to write nano structures and subsequently read patterns, it is possible to create nano-scale patterns with remarkable resolution (<100 nm) and simultaneously control the

chemical functionality of the written regions. This makes SPL a unique tool that has been considered as a crucial technology for nanometer scale structures.

In this research, we propose a novel platform based on one-dimensional silicon nano-wires (SiNWs) and gold nano-particles for detection of the biological molecular and chemical species. SiNWs were performed based on SPL technique and anisotropic tetra-methyl-ammonium hydroxide (TMAH) wet etching (or RIE dry etching). Gold nano-particles were obtained by chemical reduction methods, and the diameter size of gold nano-particles was controlled by the reaction time. Then, we will utilize a combination of scanning probe nanolithography and self-assembly monolayer (SAMs) techniques for realizing selective deposition of gold nanoparticles onto the SiNWs surface. AFM scanning tip was adopted to deposit organic N-(2-aminoethyl)-3-amino-propyl-tri-methoxysilane (AEAPTMS) molecules nanopatterns through a water meniscus onto the SiNWs surface. In addition, selective patterning of self-assembled AEAPTMS monolayer on the thin SiO<sub>2</sub> surface of SiNWs is realized by using SPL local field-induced bond breaking technique. Afterwards, amino silane molecules modification as linkers for selectively anchoring gold nano-particles onto silanation modification patterns on the SiNWs surface via Coulomb force. It is believed that the proposed nanofabrication technique combined SPL method with the SAMs process can be further applied in both nano-electronics and nano-biochemical sensors applications.

## 誌 謝

本研究論文得以順利完成，首先由衷的感謝交大奈米科技研究所教授許鈺宗博士以及交大電子物理所教授趙天生博士兩位指導教授多年來的關心照顧、悉心指導與啟發，使得作者在專業領域上受益良多，得以能夠順利地在職進修完成博士學位。

研究期間，由衷感謝國家同步輻射中心(NSRRC)梁耕三主任、陳家浩博士、人事趙平文先生以及臺灣師範大學化學系洪偉修教授等人的關心、協助與幫忙，加上國家奈米米元件實驗室(NDL)、交大奈米中心(SRC)所提供之完善優良的製程設備，使本人得以順利完成此研究論文。此外，感謝交大電子所文政學長、建豪學長、柏儀同學，電物所偉成學弟等人在實驗上提供許多寶貴的意見，也要感謝實驗室的諸多伙伴們：振嘉、柏鈞、泰瑞、皓恆、宥任、裕得、玠澤、學宏、振廷、錫波、奕貞、欣霖、子訓、昶龍等學弟的在實驗上的諸多幫忙與協助，在此一並致上誠摯的感激與謝意。

最後，謹以此一研究論文獻給我最敬愛的父母及家人。衷心感謝我最敬愛的父母以及兄、姐，感謝您們多年的提攜關心、鼓勵與幫助，同時也感謝愛妻碧琪與寶貝女兒芷瑀於求學期間給予我的關心與鼓勵，在您的支持與肯定下，使得我能全力以赴順利完成學業。

吳家豪 於交通大學

June 25, 2007

# Contents

Chinese abstract .....	i
English abstract .....	iii
Acknowledgement .....	v
Contents .....	vi
Figure Captions .....	ix
<b>1. Introduction</b> .....	<b>1</b>
1.1 Interesting nano-monde.....	1
1.2 Ultimate resolution limit of optical lithography.....	4
1.3 Introduction of next generation lithographies (NGLs) .....	4
1.3.1 Electron-beam lithography (EBL) .....	5
1.3.2 Focused ion beam lithography (FIB Litho) .....	5
1.3.3 Extreme ultraviolet lithography (EUV Litho) .....	5
1.3.4 X-ray lithography (XRL) .....	6
1.3.5 Micro contact printing ( $\mu$ CP).....	7
1.3.6 Scanning probe lithography (SPL) .....	7
1.4 Organization of this dissertation .....	8
Reference .....	10
<b>2. Scanning Probe Nanolithography</b> .....	<b>13</b>
2.1 The history of SPM invention .....	13
2.2 General principle of scanning probe microscopy (SPM). .....	15
2.3 The mechanism of SPL field-induced local oxidation .....	19
2.4 Orientation-dependent anisotropic wet Etching.....	21
2.5 Influenced parameters of SPL field-induced oxidation .....	23
2.5.1 Additional bias effect between tip and sample surface .....	23
2.5.2 SPM tip force effect between tip and sample surface .....	26
2.5.3 Effect of APM-tip scanning speed.....	27
2.5.4 Influence of ambient humidity .....	28
2.5.5 Influence of etching temperature .....	29



2.6	Nano filter structures fabrication on (100)-Si substrate by using SPL method .....	31
2.7	Linearity control of Scanning Probe Lithography on (110) Silicon Substrate.....	32
2.7.1	Linearity control experiment .....	33
2.7.2	Linear control of nanostructures transfer .....	34
2.8	Summary .....	41
	Reference .....	42
<b>3.</b>	<b>Dip-Pen Nanolithography</b> .....	<b>44</b>
3.1	Introduction of dip-pen lithography applications.....	45
3.2	Impact of UV-induced production of gold nanoclusters on the SiO <sub>2</sub> Surface of SiNWs by using DPN technique .....	47
3.2.1	Experiment details of the UV-induced production of gold nanoclusters with DPN lithography .....	48
3.2.2	Relationship of DPN Transport Mechanisms .....	49
3.2.3	X-ray photoelectron spectra of UV-induced reduction of gold nanoclusters .....	50
3.2.4	Electrical characteristics of influence of UV-induced reduction of gold nanoclusters. ....	55
3.3	Selective deposition of gold particles on Dip-pen Nanolithography patterns on silicon dioxide surfaces. ....	57
3.3.1	Generate the molecular monolayer by DPN technique .....	57
3.3.2	Colloidal gold nano particles synthesis and anchored onto the amino-terminal surface with the self-assembly method (SAMs) .....	59
3.3.3	Linear control patterning of the DPN lithography.....	61
3.4	Gold nanoparticles selective anchored on DPN AEAPTMS regions	64
3.5	Conclusions .....	67
	Reference .....	68
<b>4.</b>	<b>Low Electron Energies of Scanning Probe Electric-field-induced Bond Breaking Lithography</b> .....	<b>71</b>

4.1	The invention review of low-dimensional novel patterning.....	71
4.2	Experimental details of SPL bond breaking patterning of amino-silanation modified SiO <sub>2</sub> surface .....	74
4.3	Efficiency of SPL bond breaking with selective deposition.....	76
4.4	The mechanism of SPL field-induced bond breaking. ....	78
4.5	Low-dimensional patterning by using SPL bond breaking. ....	83
4.6	Interesting of SPL electric-field induced gray-level selective patterning.....	88
4.7	Gold nanoparticles selective anchored locally on SiNWs by using SPL bond breaking technique. ....	94
4.7.1	Modification of channel surface of silicon nanowires. ....	96
4.7.2	Electrical characteristic analysis of various modified P-SiNWs. ....	98
4.8	Photoresponse of surface plasmon resonance of SiNWs with desired gold nanoparticles.....	101
4.8.1	Physical principles of surface plasmon resonance. ....	102
4.8.2	Small amount of gold nanoparticles was controllable to selective anchored on the desired p-channel surface of SiNWs devices.....	104
4.8.3	Photoconductivity with p-channel of SiNWs with few amounts of AuNPs is enhanced by surface plasmon resonance. ....	107
4.9	Conclusions .....	112
	Reference .....	113
<b>5.</b>	<b>Summary .....</b>	<b>116</b>
<b>Appendix</b>		
	Autobiography .....	118
	Publications list of Chia-Hao Wu .....	121

## Figure Captions

Figure 1.1	IBM Millipede nanomechanical data storage systems. This system makes it possible to reach speeds of read/write of several Mbits/sec, and makes it possible to reach densities of 153 Gbits/in <sup>2</sup> .....	2
Figure 1.2	The Semiconductor Industry Association’s 2006 national technology roadmap for memory technologies and associated with the lithographic technologies that critical dimensions. ....	3
Figure 2.1	Principle of operation of the scanning tunneling microscope from the original article on the STM. The piezodrives $P_x$ and $P_y$ scan the metal tip M to traverse the surface. It describes the operation of the microscope for purpose tunnel effect. ....	14
Figure 2.2	The schematic of the position-sensitive photo detector (PSPD) .....	16
Figure 2.3	The relationship curves of interatomic force vs. distance between SPM tip and sample surface. ....	17
Figure 2.4	Distribution diagram of electric field exists between the apex of AFM-tip and the substrate surface. ....	19
Figure 2.5	Schematic principle of SPM-based electric-field induced local oxidation process. ....	21
Figure 2.6	Diagram of orientation-dependent anisotropic wet etching in various orientation silicon planes. (a) (100) crystallographic plane, (b) (110)-crystallographic plane. ....	22
Figure 2.7	Depth and height of SPL field-induced local oxide patterns varied with additional applied tip voltages from -6 V to -10 V. ....	24
Figure 2.8	Characteristics curve of linewidth and oxide height of SPL field-induced local oxide patterns varied with different tip voltages from -5 V to -10 V. ....	25
Figure 2.9	Tip force characteristics curve of local oxidation grid lines. The tip bias, tip scanning speed, and ambient humidity were maintained on -9 V, 1.0 $\mu\text{m}/\text{sec}$ , and $45 \pm 1\%$ , respectively. ....	26

Figure 2.10	Characteristic curves of oxidation grid lines of effect of scanning speed. The tip bias, tip force, and ambient humidity were maintained on -9 V, 15 nN, and 45 ± 1%, respectively. ....	27
Figure 2.11	Characteristic curves of oxidation grid lines of influence of ambient humidity. The tip bias, tip force, and scanning speed were maintained on -9 V, 10 nN, and 1.0 μm/sec, respectively. ....	28
Figure 2.12	Characteristic relationship curves of etching rate vs. etching temperature. ....	29
Figure 2.13	Characteristic relationship curves of selective etching ratio vs. etching temperature. ....	30
Figure 2.14	Influence of additional agitation for the surface roughness Rq (nm) as etching temperature increasing. ....	31
Figure 2.15	SEM images of nano-filter structures. ....	32
Figure 2.16	Nanostructure grid line patterns transfer on (110)-Si procedure by using the multipixel scanning method of scanning probe lithography. ....	34
Figure 2.17	AFM topographic height profiles along the local oxidation nanostructure grid line marked patterns by utilizing the multipixel scanning times and different line/space of the pitch. (a) Pitch = 40 nm ; (b) Pitch = 30 nm. ....	36
Figure 2.18	Linear control of pattern transfer of line nanostructure into (110) silicon substrate by SPM-based multipixel scanning local oxidation and wet etching in a 34 % KOH solution for 45 sec.....	37
Figure 2.19	Linearity characteristic curve of oxidation patterns transfer into (110)-silicon wafer by using the scanning probe lithography technique after aqueous KOH anisotropic wet etching process. The pitch of between each scanning pixel is 15 nm.....	38
Figure 2.20	Nanostructure pattern Gauss distribution illustration of transferred grid line nanostructure into (110) silicon wafer by the scanning probe lithography and anisotropic wet etching. (a) one pixel patterning; (b) two pixels patterning; (c) three pixels patterning; (d) four pixels patterning. The average linewidth is around 25.88 nm, 44.47 nm, 64.41 nm, and 77.76 nm, respectively. ....	39

Figure 2.21	SEM image of the high aspect ratio (9.71 : 1) Si nanostructure fabricated by SPM-based local oxidation and wet anisotropic etching. The pattern height is about 191.2 nm and the pattern width is about 19.69 nm. ....	40
Figure 3.1	Schematic representation of Dip-Pen Nanolithography (DPN). Transport mechanism of molecules to the surface via the water meniscus forms between the AFM-tip and the sample surface in air. ....	44
Figure 3.2	Characteristic curve between speed of the dip-pen lithography and relative humidity of environment at room temperature. ....	49
Figure 3.3	X-ray photoelectron spectroscopy (XPS) analysis spectra of the 365 nm UV-light irradiation process on the SiO <sub>2</sub> surface of the silicon substrate. ....	51
Figure 3.4	(a) Schematic diagram of the Dip-Pen Nanolithography directly patterning. (b)AFM images of a silicon nanowire device on (100) SOI substrate fabricated by using scanning probe microscope (SPM) local oxidation method and TMAH wet etching. Nanowire is about 100 nm wide and 2 μm long.....	52
Figure 3.5	XPS spectra of the AuCl / native oxide / Si system as function of UV exposure time. It was found that UV irradiation induced production of gold nanoclusters on the surface of a silicon dioxide sample. ....	53
Figure 3.6	(a) AFM images of the SiNWs. (b) LFM image of a silicon nanowire after DPN of HAuCl <sub>4</sub> ink in area of 0.5 by 2 μm across the SiNW at speed of 50 nm/sec and RH of 85 %. (c) Depth profile of A-A' section of a LFM image. A 2 μm LFM profile parallel to the SiNW and the thickness of gold nanoclusters is the less than 1 nm in thickness.....	54
Figure 3.7	(a) Electrical properties (I-V <sub>ds</sub> ) of three different samples (SiNWs, SiNWs + DPN HAuCl <sub>4</sub> , SiNWs + DPN HAuCl <sub>4</sub> + UV irradiation) at 300 K with sweep of source-drain bias V <sub>ds</sub> (-1.0 V and 1.0 V) at V <sub>g</sub> = 5 V. (b) I <sub>d</sub> -V <sub>g</sub> characteristics of SiNWs measured at 300 K with different source drain bias V <sub>ds</sub> (0.6 V and 1.0 V).....	56

Figure 3.8	(a) The mechanism of deposition of a monolayer of AEAPTMS molecules on the hydroxyl-terminal surface of an oxidized silicon substrate. (b) Citrate-coated gold nanoparticles were deposited selectively onto the AEAPTMS nanopattern via Coulombic force. ...	58
Figure 3.9	(a) High resolution TEM images of 15 nm gold nanoparticles. (b) SEM images of AuNPs self-assembled on the AEAPTMS-functionalized SiO <sub>2</sub> surface. (c) X-ray photoelectron spectra of AuNPs anchored on the AEAPTMS-functionalized SiO <sub>2</sub> surface. ...	60
Figure 3.10	Characteristic curves from dip-pen lithography for the AEAPTMS ink. (a) Relationship of DPN linewidth with respect to tip writing speed under different relative humidities. (b) Relationship of the contact width and diffusion coefficient estimated from Figure 3.10 (a) under different relative humidities. ....	62
Figure 3.11	LFM images of DPN-generated AEAPTMS monolayer patterns on silicon oxide surfaces. LFM images were recorded at a scan rate of 6 Hz. Parallel line AEAPTMS patterns on an oxidized silicon surface were generated at writing speeds of 0.1, 0.2, 0.3, 0.4, 0.5 and 0.6 μm/sec. The linewidth of 60 nm has been drawn via DPN technique.	63
Figure 3.12	(a) LFM images of DPN AEAPTMS monolayer patterns on SiO <sub>2</sub> surfaces. Dotted lines show the designed patterned area. (b) AC-mode AFM topographic image of gold nano-particles after selective deposition on the square patterns modified by silanation by DPN after immersion in the gold nano-particle solution for 1 h. ....	65
Figure 3.13	Spectra from x-ray photoelectron spectroscopy of the areas of DPN AEAPTMS patterns and outside the DPN AEAPTMS patterns to evaluate the selectivity of gold nanoparticles for the AEAPTMS patterns and for the SiO <sub>2</sub> surface. No Au4f signal was observed outside the DPN AEAPTMS patterned area. ....	66
Figure 4.1	(a) The mechanism of deposition of a monolayer of AEAPTMS molecules on the hydroxyl-terminal surface of an oxidized silicon substrate. (b) The schematic diagram of citrate-stabilized AuNPs was selectively anchored on the unexposed area .....	73

Figure 4.2	SEM images of the citrate-stabilized AuNPs were selectively anchored on the SPL bond breaking unexposed area.....	74
Figure 4.3	SEM images show that efficiency of SPL bond breaking with selective deposition of AuNPs under different tip-sample bias (4.0 V to 6.5 V) and a control drawing speed 0.5 $\mu\text{m}/\text{sec}$ onto 2.5 nm SiO <sub>2</sub> surface. Right-side inset shows lateral force microscopy (LFM) images of SPL bond breaking patterns on SiO <sub>2</sub> surface before AuNPs selective deposition process .....	76
Figure 4.4	Figure 4.4 Linearity relationship curves of linewidths with respect to SPL tip/sample bias for AEAPTMS SAMs bond breaking under a control relative humidity ( $58 \pm 1\%$ ) .....	78
Figure 4.5	Tunneling current densities for 2.5 nm silicon dioxide thicknesses as a function of the voltage across silicon dioxide ( $V_{\text{ox}}$ ). This figure shows that different tunneling effects dominate different voltage across silicon dioxide of regions. ....	79
Figure 4.6	AuNPs selective deposition on the SPL unexposed patterns for different bond breaking voltages as a function of the inverse tip scanning speed is exponential increased. For SPL tip bias is lower than 5 volts, the SPL bonds breaking energy is not enough to completely cleave N-H, C-N bonds on the SiO <sub>2</sub> surface so that AuNPs were able to assemble onto the SPL bonds breaking patterns with lower density .....	80
Figure 4.7	XPS analysis exhibits the regions of the SPL of AEAPTMS SAMs bond breaking for the nitrogen N1s peak under different tip / sample bias. For tip / sample bias of SPL bond breaking lower than 5 volts, the nitrogen N1s signals are still observable. It implies that SPL bond breaking energy is not enough to decompose N-H bonds efficiently on the SiO <sub>2</sub> surface.....	82
Figure 4.8	SEM images of 15-nm AuNPs deposition on the desired triangles and squares patterns of unexposed silanation modification regions by applied the low energies of bias 6.5 V after immersion in the AuNPs solution for 1.5 h .....	83

Figure 4.9	SEM images show that the amount of 15nm AuNPs are successfully controlled and selectively immobilized outside the SPL bon breaking desired grid line patterns on the SiO <sub>2</sub> surface by applied the low energies of bias 6.5 V after immersion in the AuNPs solution for 1.5 h. The details of line patterns composed of single AuNPs on the SiO <sub>2</sub> surface. (a)Gap = 300 nm; (b)Gap = 200 nm; (c)Gap = 100 nm .....	84
Figure 4.10	Spectra of x-ray photoelectron microscopy at the regions of SPL bond breaking patterns and outside the SPL bond breaking patterns to evaluate the selectivity of AuNPs. The Au4f signal was observed clearly outside the SPL bond breaking area, and no Au4f signal was observed inside the SPL bond breaking area. The SPL bias and tip scanning speed is 6.5 volts and 0.5 μm/sec, respectively.....	85
Figure 4.11	(a) SEM image shows that SPL bond breaking of AEAPTMS SAMs were successfully carried out by applying tip / sample bias from 6.0 to 10 V at scanning speed of 0.2 μm/sec onto 8 nm SiO <sub>2</sub> surface. Tip scanning speed in SPL bond breaking plays an important role as shown in (b) 0.3 μm/sec, (c) 0.2 μm/sec at tip / sample bias of 10 V.	86
Figure 4.12	SEM image shows deposition selectivity of 15-nm AuNPs on the regions of unexposed aminosilane modified surface. The SPL patterning pitches changed from 200 nm to 1 μm (left to right) with tip / sample bias of 6.5 volts and immersion the sample in the AuNPs solution for 1.5 h. The numbers of AuNPs are confined spatially with electrostatic force on the area of unexposed patterns on the SiO <sub>2</sub> surface down to single digit (circled) .....	87
Figure 4.13	SEM images of 15-nm AuNPs selective deposition on the desired squares patterns of unexposed silanation modification regions by applied the low energies of additional bias after immersion in the AuNPs solution for 1.5 h. (a) 5 Volts and (b) 3.5 Volts. ....	89
Figure 4.14	SEM images of the distribution densities of the 15-nm AuNPs selective deposition on the desired squares patterns of unexposed silanation modification regions by applied the low energies of additional bias after immersion in the AuNPs solution for 1.5 h. ....	91



Figure 4.15	Characteristic relationship curve between the distribution densities of the gold nanoparticles selective deposition on the SPL-exposed patterns and SPL bond breaking voltages at room temperature and the relative humidity was maintained on $60 \pm 1\%$ .	92
Figure 4.16	(a) Black and white gray-level photograph of the physicist Richard P. Feynman (Resolution: $512 \times 512$ ); (b) SEM images of the AuNPs selective gray-level patterning on the $\text{SiO}_2$ surface by applied the low energies of additional bias after immersion in the AuNPs solution for 1h. (Gray-level patterning voltages from 2.5 V to 5.5 V, the resolution of SPL bond breaking patterning is 11.71875 mV/grad and the pitch of pixel is about 97.66 nm) .....	93
Figure 4.17	SEM image shows selective deposition locally of 15-nm AuNPs on the desired regions of unexposed aminosilane modified surface of silicon nanowires. SPL bond breaking patterning with tip/sample bias of 6.5 volts and immersion the sample in the AuNPs solution for 1.5 h. (a) desired region = 850 nm, (b) desired region = 350 nm.....	95
Figure 4.18	SEM images of the p-type silicon nanowires were fabricated by E-beam nano-lithography with an anisotropic RIE dry etching process. The linewidth of nanowires was about 150 nm and 10 $\mu\text{m}$ long. ....	96
Figure 4.19	Schematic of different chemical molecular modifications of channel surface states of the p-type silicon nanowires devices at room temperature. (A) $\text{OH}^-$ -gated modification, (B) $\text{NH}_3^+$ -gated modification, (C) SPL decomposed amino bonds, (D) AuNPs with citrate ions ( $\text{COO}^-$ ) modification. ....	97
Figure 4.20	Electrical properties ( $I_{\text{DS}}\text{-}V_{\text{DS}}$ ) analysis of p-type silicon nanowires devices with different chemical molecular modifications capping at room temperature. The turn-on voltage and electrical conductance of p-type SiNWs devices have clear different with varies of the chemical modifications on the channel surface of p-type SiNWs.....	98

Figure 4.21	Schematic of band diagram of p-channel of SiNWs gated by (a) amine of AEAPTMS, (b) amino chemical bonds decomposed, and (c) gold nanoparticles selective deposition, respectively. Amine of AEAPTMS serves as a positive gate to the Si channel, which depletes holes in p-channel of SiNWs. SPL field-induced bond breaking modify the quantity of AEAPTMS on p-type Si nanowire which reduce AEAPTMS depletion effect in p-channel. Gold nano particles with citrate ions serve as a negative gate to the p-channel of SiNWs, which accumulate holes in p-type Si channel. ....	100
Figure 4.22	(a) Schematic diagrams of the surface plasmon resonance devices enhanced by gold metal surface. (b) Charge distribution for dipole-dipole coupling resonance.....	103
Figure 4.23	Decomposed efficiency of SPL bond breaking on the p-channel SiO <sub>2</sub> of SiNWs devices at a tip scanning speed from 0.5 μm/sec to 0.1 μm/sec. Tip bias, set point, and ambient humidity was maintained on -10 V, 0.5 V, and 60 ± 1%, respectively. ....	104
Figure 4.24	SEM images of gold nanoparticles selective deposition on the SPL unexposed silanation modification regions of (100) p-type silicon nanowires (SiNWs) devices. Nanowire is about 150 nm wide and 10 μm long. Inset shows the details of the small amount of gold nanoparticles are successfully controlled and selectively anchored on the small SPL unexposed region of SiO <sub>2</sub> surfaces of p-channel of SiNWs devices. ....	106
Figure 4.25	Electrical conductive properties (I-Vds) of bare SiNWs without AuNPs capping and without any irradiation process at room temperature with sweep of source-drain (Vds) bias 10 mV. It was found that the conductance was about 9.62 μS.....	107
Figure 4.26	Schematic diagrams of photoconductivity enhanced on the few AuNPs of p-channel surface of SiNWs devices by surface plasmon resonance effect.....	108

Figure 4.27	Photoconductive characteristics of p-type bare SiNWs without any AuNPs capping at five different light wavelength irradiation processes at room temperature with sweep of source-drain ( $V_{ds}$ ) bias 10 mV.....	109
Figure 4.28	Various photoconductivity characteristic measurements of p-type silicon nanowires devices. Photoconductivity is enhanced by surface plasmon resonance. After AuNPs selective deposition process, it was found that noticeable response at wavelength of 520 nm and wavelength of 720 nm, respectively. ....	110
Figure 4.29	Photoresponse measurements. The surface plasmon resonance characteristics of p-type SiNWs with AuNPs capping at five different light wavelength irradiation processes at 300 K with sweep of source-drain ( $V_{ds}$ ) bias 10 mV.....	111



# Chapter 1.

## Introduction

### 1.1 Interesting nano-monde

The 21<sup>st</sup> century has awaited the beginning to plunge in the nanomonde, the nano-science and technology is fundamentally changing the impression of everything for human being. Physicist Richard P. Feynman [1] said, “When we get to the very, very small world—say circuits of seven atoms---we have a lot of new things that would happen that represent completely new opportunities for design. Atoms on a small scale behave like nothing on a large scale, for they satisfy the laws of quantum mechanics.” In his famous lecture “*There’s Plenty of Room at the Bottom*” at the annual meeting of the American Physical Society at the California Institute of Technology in 1959. Dr. Feynman described a process by which the ability to manipulate individual atoms and molecules might be developed, using one set of precise tools to build and operate another proportionally smaller set, so on down to the needed scale.

Dr. Feynman considered a number of interesting ramifications of a general ability to manipulate matter on an atomic scale. He was particularly interested in the possibilities of denser computer circuitry, and microscopes which could see things much smaller than is possible with scanning electron microscopes. These ideas were later realized by the use of the scanning probe microscopy (scanning tunneling microscope (STM) / atomic force microscope (AFM)). The laboratories of IBM [2, 3] and Stanford [4] developed a system points in parallel. One of the emergent applications in the field of the storage systems of data such as “Millipede”, created by researchers at IBM group [1, 2], as shown in Figure 1. The read/write head is in fact a matrix of more than 1000 thermomechanical points operating simultaneously, manufactured on only one silicon substrate. All small holes in a polymer film carried out by the point of the heated AFM represent stored bits which can be read by the same point. This technique makes it possible to reach densities of 153 Gbits/in<sup>2</sup>, well above the limit envisaged by magnetic storage.

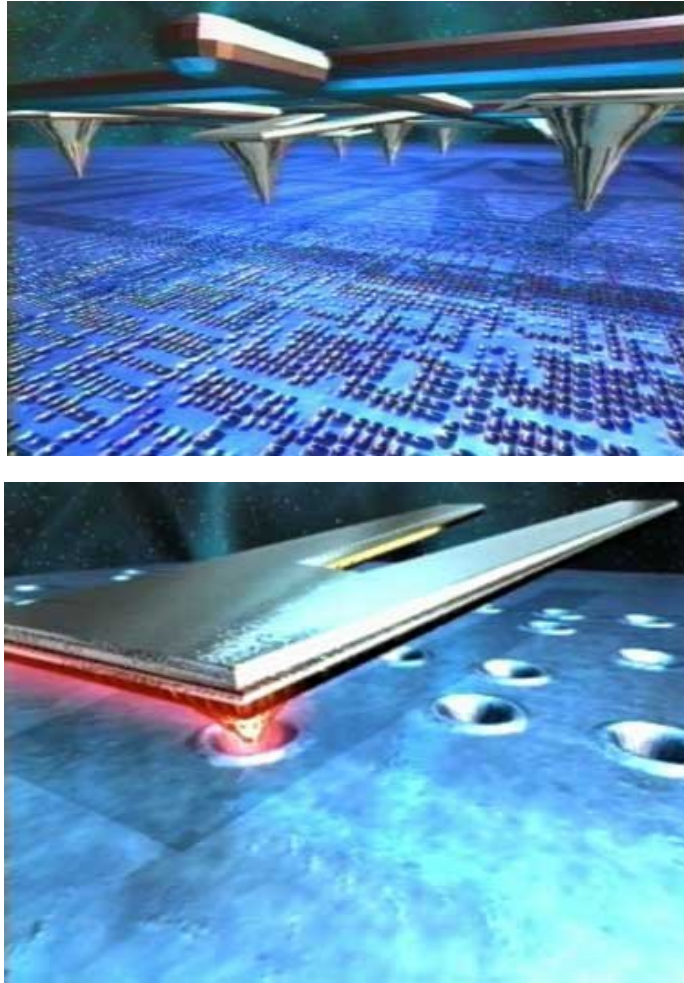
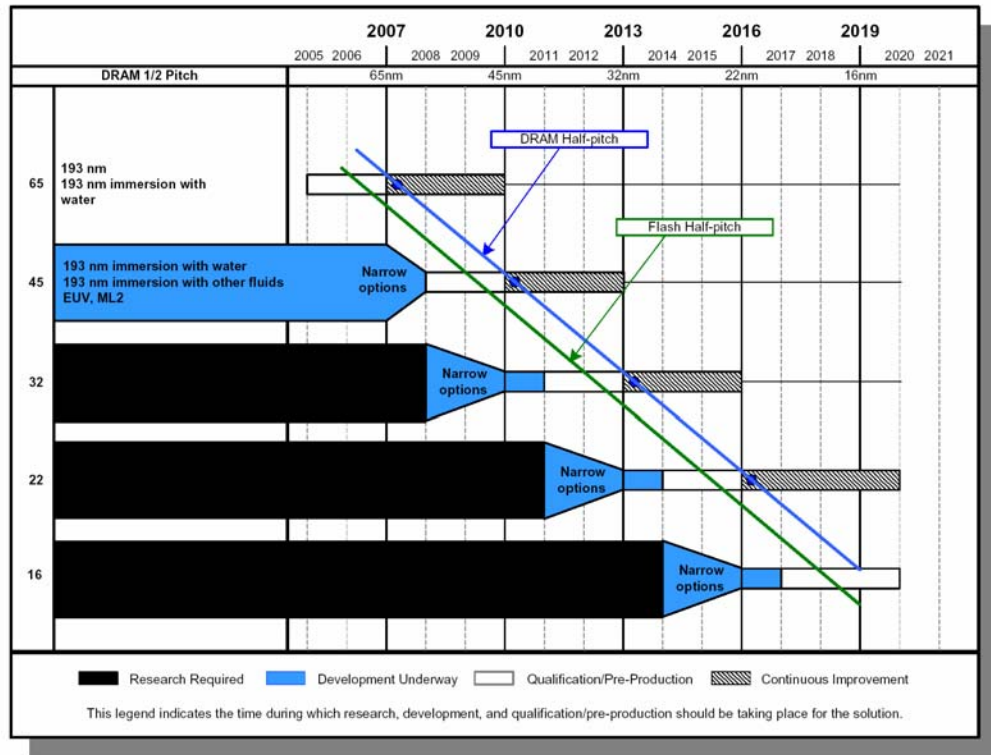


**Figure 1.1** IBM Millipede nanomechanical data storage systems. This system makes it possible to reach speeds of read/write of several Mbits/sec, and makes it possible to reach densities of 153 Gbits/in<sup>2</sup>. [2, 3]

As the electronic products are widely used today, smaller products with versatile functions are always desired. Recently, an enormous investment in research and development has resulted in the ability to fabricate structures with nanometer sizes. Since 1965, there has been an exponential decrease in the device dimensions of production transistors, a historical trend known as “Moore’s Law” [5]. As of 1998, the critical dimension in production integrated circuits is 250 nm. Figure 1.2 shows the Semiconductor Industry Association’s 2006 national technology roadmap for memory technologies and associated with the lithographic technologies that critical dimensions will shrink to 45 nm by 2010, to 32 nm in 2013, and to 22 nm by 2016. The conventional photolithography used for printing integrated circuit features is approaching fundamental limitations. An

alternative lithography technology may be required, we are investigating scanning probe lithography as a viable alternative for patterning 100 nm feature sizes and below.



Notes: RET and lithography friendly design rules will be used with all optical lithography solutions, including with immersion; therefore, they are not explicitly noted.

**Figure 1.2** The Semiconductor Industry Association’s 2006 national technology roadmap for memory technologies and associated with the lithographic technologies that critical dimensions will shrink to 45 nm by 2010, to 32 nm in 2013, and to 22 nm by 2016. [6]

The downscaling of electronic devices is also very interesting from a physical point of view. In general, the quantum confinement phenomena are usually only observed at very low temperatures. However, when the dimensions are sufficiently small, some of these quantum phenomena become observable even at room temperature. As the diameter of the nano particle was smaller than a Bohr exciton length, the energy bands with a quantum confinement effect become discontinuous. The size of the fabricated structures will at a certain point become comparable to the characteristic length scales for the coherent electron transport (ex: single electron charging effects). Traditionally, the IC devices industry relies on optical lithography for the fabrication of IC devices. However, optical lithography will reach its physical limits and at that point new techniques will be required

to fabricate devices with nanometer scale dimensions.

## **1.2 Ultimate resolution limit of optical lithography**

To obtain the desired feature size, the ultimate resolution of the optical lithography is mainly expressed by the Rayleigh's equation in terms of wavelength of exposure  $\lambda$  and numerical aperture of the optical system (NA): Resolution =  $K_1 \times \lambda / NA$ . The depth of focal (DOF) corresponding is given by  $DOF = K_2 \times \lambda / NA^2$ , where  $K_1$  and  $K_2$  are constants which depend on the selected photo-resists and the lithographic processes used.

In general, in order to obtain higher resolutions, the shorter optical wavelengths and objective with larger numerical aperture can be used, and caused the depth of focal to become lower. Furthermore, to obtain the nano-scaled resolution (<100nm), the traditional optical lithography will be reaching the physical-optical limits, and at that nanotechnology development aim the next generation novel lithography techniques will be required to fabricate devices with nanometer scale resolution.



## **1.3 Introduction of next generation lithographies (NGLs)**

As the semiconductor industry continues to shrink its design rules, new advanced metrology and lithography tools become increasingly important. While the dimensions of the very large scale integration devices are scaled down towards the nano-meter region, traditional lithography techniques employing visible light and ultraviolet light confront a serious barrier due to the far-field limitation of the wavelength of light. There has been much recent work on applying the well-known next generation lithography techniques of electron- beam lithography (EBL) [7-10], focused ion beam (FIB) lithography [11,12], extreme ultraviolet lithography (EUV Litho) [13,14], X-ray lithography (XRL) [15-18], microcontact printing ( $\mu$ CP) [19-21], and scanning probe lithography (SPL) [22-27] to solve these problems.

### **1.3.1 Electron-beam lithography (EBL)**

This lithography by electron beam, where an electron beam rather than of photons is used like source of exposure. Electron beam lithography is a well-know high resolution patterning technique in which high-accelerated energies (20 ~ 100 KeV) electron were focused into a narrow electron beam and used to expose electron-sensitive resists (ex: PMMA resist). An electron-beam direct writing system with a character projection aperture is a promising candidate as an effective maskless lithography tool to realize a system on the nano-fabrication process. It allows a very small resolution and a great depth of field. It was also used in the fabrication of conclusive devices making it possible to explore the nano-electronics. This technology can focus the charged electron beam to tha feature size as small as 10 nm. The principal disadvantage of this technique includes: the expensive equipment cost, the proximity effect, and the slowness of the manufacturing processes.

### **1.3.2 Focused ion beam lithography (FIB Litho)**

The focused ion beam lithography using a beam of ions is conceptually similar to E-beam lithography. In ion beam lithography, ions that are incident on the nominally opaque area of a stencil mask can scatter into the open windows and escape, exposing a wide area of the substrate. So, these ions can lose much of their initial energy in the mask, the scattered particle exposure is concentrated near the resist surface. In theory, the more important mass of the ions should result in possibilities from imagery which was less prone to distortion due to the stochastic space charge effect. So, the ion beam lithography systems with beam of ions of high resolution are developed still little compared to the systems with electron beams.

### **1.3.3 Extreme ultraviolet lithography (EUV Litho)**

Optical lithography will reach its resolution limit for semiconductor processing at the generation where half of the pitch between lines is about 40 nm. Extreme ultraviolet lithography (EUV Litho) is an advanced technology for making micro / nano processors a hundred times more powerful than those made today. EUV Litho is one technology vying to replace the traditional photolithograhly used to make today's nano-circuits. This method



uses the same principles as the optical lithography in which light is refracted through camera lenses onto the wafer by conventional projection and also obeys the equation of Rayleigh. EUV Litho, with a much shorter wavelength of 13.5 nm, can provide imaging with a higher contrast and larger depth of focus than even hyper-NA Argon Fluoride (ArF) lithography with a 193 nm wavelength. The Rayleigh depth of focus is significantly larger for the EUV Litho than for ArF immersion lithography.

However, the primary challenge for the EUV Litho is not imaging contrast, but developing the supporting infrastructure. The EUV masks, resists, and light sources for the EUV Litho are very different from those used for optical lithography. The very large nonrecurring engineering costs associated with the development of EUV Litho are possibly the single most important challenge facing this lithography technology.

#### **1.3.4 X-ray lithography (XRL)**

X-ray Lithography (XRL) is a next generation lithography that has been developed for the semiconductor industry. XRL has been well known since the early developmental stages that x-ray lithography has unique and excellent features, such as the ability to fabricate fine patterns. The short wavelengths of 0.8 nm X-rays overcome diffraction limits in the resolution of otherwise competitive optical lithography. The X-rays illuminate a mask placed in proximity to a resist-coated wafer. No lenses are used, and only rudimentary collimating mirrors. The X-rays are broadband, typically from a compact synchrotron radiation source, allowing rapid exposure. The mask consists of an X-ray absorber, typically of gold or compounds of tantalum or tungsten, on a membrane that is transparent to X-rays, typically of silicon carbide or diamond. The pattern on the mask is written by direct write electron beam lithography onto a resist that is developed by conventional semiconductor processes. The membrane can be stretched for overlay accuracy. Negligible spurious scattering is a unique quality of X-ray lithography. For nanolithography, the result of using XRL, as well as being wise about the selection of materials and wavelengths, is absorption without spurious scattering. Nevertheless, the masks preparation was very different and complex, and it was also the principal challenge of the X-ray lithography. In order to be candidate for the next generation of nano-circuits, this process must allow very great investments out of equipment and infrastructures such as the preparation of XRL masks.

### **1.3.5 Microcontact printing ( $\mu$ CP)**

The possibility to control the adsorption of a monolayer of molecules to specific locations of a surface with sub-micro resolution has become available in recent years with the advent of microcontact printing ( $\mu$ CP). This technique makes use of a rubber-elastic membrane with a relief pattern. Besides chemical patterning, microcontact printing ( $\mu$ CP) was used as a lithography tool. Simplicity, low cost, high throughput, at sub-100 nm resolution, makes microcontact printing technique an excellent candidate for a wide variety of applications. Nevertheless, the microcontact printing technique suffers from a few drawbacks. The main problem is the poor level of definition and stability of the stamp dimension.

### **1.3.6 Scanning probe lithography (SPL)**

Scanning probe lithography (SPL) uses the conductive tip of a scanning probe microscope to create a pattern. At its crudest, the AFM-tip can be used to produce marks by scratching, nanoindentation or by heating with the tip. Among these lithography techniques, one potential approach for fabricating the nanostructures is the use of scanning probe lithography. A more elegant method uses the tip to oxidise material in a specific pattern. When a voltage is applied between the sharp probe AFM-tip and sample surface, an intense electric field is created that can be used to oxidise material in the vicinity of the tip. Recently, scanning probe lithography (SPL) technique is an emerging area of research in which the scanning tunneling microscopy (STM) and the atomic force microscopy (AFM) have been used to perform nanometer-scale surface modification and dominated the field of nanometer structures fabrication. The advantages of the scanning probe lithography technique are its high resolution, alignment accuracy, high reliability, absence of radiation damage, simpler and lower-cost. The motivation for the study of SPL includes improved critical dimensions, the ability to image nano patterns in situ, and the practical elimination of electron backscattering effects compared with conventional E-beam lithography with polymeric resists.

## 1.4 Organization of this dissertation

In this thesis, the well-known next generation lithography techniques includes: electron-beam lithography, focused ion beam lithography, extreme ultraviolet lithography, x-ray lithography, microcontact printing, and scanning probe lithography will introduce in the chapter 1.

Chapter 2 describes the mechanism of electrical-field local oxidation of scanning probe nanolithography. In this section, we have investigated that the nanostructures fabrication on the silicon substrate. We have successfully demonstrated the ability of nanostructure patterns transfer of linearity lithography, and accurately defined the linewidth of nanostructure patterns by using SPL technique with anisotropic wet etching process. In this study, well-defined nano structures are fabricated by scanning probe lithography technique under properly control on tip bias, tip force, scanning speed and tip humidity of patterning environment will also be discussed.

Chapter 3 focused on the characterization and applications of the dip-pen nanolithography (DPN). We utilized an AFM-tip as a “nano-pen” to transport the “organic molecular ink” onto a substrate surface via the water meniscus. In this section, we report a successful technique for using DPN technique to write molecule ink ( $\text{HAuCl}_4$ ) structures directly onto oxidized surfaces of silicon nanowires (SiNWs). This novel method was performed based on scanning probe lithography technique and anisotropic wet etching process. Dip-pen nanolithography (DPN) was adopted to provide  $\text{HAuCl}_4$  ink (7.5 mM) on the surface of  $\text{SiO}_2/\text{Si}$  samples and followed by 365 nm UV light-induced reduction of gold ions on the area of interest such that gold nanoclusters formed selectively. Then, X-ray photoelectron spectroscopy (XPS) was adapted to analysis the surface chemical state of the sample surface. We proposed this nanofabrication technique combined DPN method with the self assembled monolayer (SAMs) process can be further applied in both nano-electronics and nano-biochemical sensors applications.

On the other hands, we also describe a novel platform to perform the selective deposition of gold nanoparticles on dip-pen nanolithographic patterns of  $\text{SiO}_2$  surfaces. We report an “inked” atomic force microscope (AFM) tip was adopted to deposit 2.2 mM organic *N*-(2-aminoethyl)-3-aminopropyltrimethoxysilane (AEAPTMS) molecules in nanopatterns through a water meniscus onto a  $\text{SiO}_2$  substrate under ambient conditions.

And, the molecules act as linkers for the selective deposition of gold nanoparticles on the SiO<sub>2</sub> surface. X-ray photoelectron spectroscopy (XPS) was then used to evaluate the presence of gold nanoparticles on the SiO<sub>2</sub> surface. Lateral force microscopy (LFM) was utilized to differentiate the surface between oxidized semiconductors and patterned areas with monolayer of AEAPTMS. Linewidths down to 60 nm have been successfully achieved by this method.

Chapter 4 describes a new approach that has successfully demonstrated for the facile patternwise deposition of AuNPs onto a SiO<sub>2</sub> surface with nanometer scale resolution by SPL field-induced bond breaking of AEAPTMS SAMs. Patterning of AEAPTMS SAMs is realized by local field-induced bond breaking using scanning probe lithography on the thin SiO<sub>2</sub> surface. AuNPs with negative-charged citrate surfaces were selectively anchored on the unpatterned area via electrostatic force between AEAPTMS SAMs and AuNPs. Different tip/sample biases were investigated for the bond breaking efficiency of AEAPTMS SAMs.

In this section, SPL bond breaking effect on amino-functional silanation modified SiO<sub>2</sub> surfaces of SiNWs was successfully demonstrated. Following SPL bond breaking of AEAPTMS, gold nanoparticles were selectively anchored on the unexposed area. It is found that the bond breaking efficiency is limited by the tunneling current through the thin SiO<sub>2</sub> film so that both the tip bias and tip scanning speed play the important roles. Single digit numbers of gold nanoparticles anchored onto unpatterned AEAPTMS SAMs were demonstrated. Moreover, we have also successfully demonstrated the binary and gray-level patterning with gold nanoparticles selective deposition by using the novel scanning probe lithography bond breaking technique. Electrical characteristics of SiNWs after different surface modifications were illustrated. Also, optical responses of SiNWs with selective binding of gold nanoparticles were demonstrated. We believed that the SPL bond breaking technique is provide a pathway to modify surface to link different functional group, enabling diverse and exciting application in bio-sensing technology and nanoelectronics.

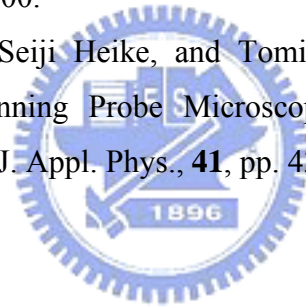
This thesis would be summarized in Chapter 5, where recommendations for future research are proposed.

## Reference

- [1] R. Feynmann, "There's plenty of room at the bottom", Eng. Sci., **23**, pp. 22-26, 1960.
- [2] M. I. Lutwyche, M. Despont, U. Drechsler, U. Dürig, W. Häberle, H. Rothuizen, R. Stutz, R. Widmer, G. K. Binnig, and P. Vettiger, "Highly parallel data storage system based on scanning probe arrays", Appl. Phys. Lett. **77**, pp. 3299-3301, 2000.
- [3] U. Drechsler, U. Durig, B. Gotsmann, W. Haberle, M. A. Lantz, H. E. Rothuizen, R. Stutz, and G. K. Binnig, "The "millipede"- nanotechnology entering data storage", IEEE Trans. on Nanotechnology, V1, pp. 39-55, 2002.
- [4] S. C. Minne, J. D. Adams, G. Yaralioglu, S. R. Manalis, A. Atalar, and C. F. Quate, "Centimeter scale atomic force microscope imaging and lithography", Appl. Phys. Lett., **73**, pp. 1742-1744, 1998.
- [5] Gordon E. Moore, Electronics, **38(8)**, 1965.
- [6] International Technology Roadmap for Semiconductors, 2006, Semiconductor Industry Association, USA. <[http:// public.itrs.net](http://public.itrs.net)>
- [7] Kathryn Wider, Calvin F. Quate, Bhanwar Singh, and David F. Kyser, "Electron beam and scanning probe lithography : A comparison", J. Vac. Sci. Technol., B16(6), pp. 3864-3873, 1998.
- [8] L. P. Muray, C. S. Silver, and J. P. Spallas, "Sub-100-nm lithography with miniature electron beam columns", J. Vac. Sci. Technol. B, **24** (6), pp. 2945-2950, 2006.
- [9] T. Tominaga, K. Nakamae, T. Matsuo, H. Fujioka, T. Nakasugi, and K. Tawarayama, "Electron-beam direct writing system employing character projection exposure with production dispatching rule", J. Vac. Sci. Technol. B, **23** (6), pp. 2780-2783, 2005.
- [10] XiaoMin Yang, Jianyun Zhou, Shuaigang Xiao, and Keith Mountfield, "Electron beam lithography for magnetic recording heads: Characterization and optimization of critical components", J. Vac. Sci. Technol. B, **24**(6), pp. 2920-2925, 2006.
- [11] N. S. Smith, W. P. Skoczylas, S. M. Kellogg, D. E. Kinion, and P. P. Tesch, O. Sutherland, A. Aanesland, and R. W. Boswell, "High brightness inductively coupled plasma source for high current focused ion beam applications", J. Vac. Sci. Technol. B, **24**(6), pp. 2902-2906, 2006.

- [12] V. Parekh, A. Ruiz, P. Ruchhoeft, H. Nounu, D. Litvinov, and J. C. Wolfe, "Estimation of scattered particle exposure in ion beam aperture array lithography", *J. Vac. Sci. Technol. B*, **24**(6), pp. 2915-2919, 2006.
- [13] Patrick Naulleau, Jason P. Cain, Erik Anderson, Kim Dean, Paul Denham, Kenneth A. Goldberg, Brian Hoef, and Keith Jackson, "Characterization of the synchrotron-based 0.3 numerical aperture extreme ultraviolet microexposure tool at the Advanced Light Source", *J. Vac. Sci. Technol. B*, **24** (6), pp. 2840-2843, 2005.
- [14] M. Nataraju, J. Sohn, S. Veeraraghavan, A. R. Mikkelsen, K. T. Turner, R. L. Engelstad, C. K. Van Peski, and K. J. Orvek, "Electrostatic chucking for extreme ultraviolet lithography: Simulations and experiments", *J. Vac. Sci. Technol. B*, **23** (6), pp. 2834-2839, 2006.
- [15] S. Balslev and F. Romanato, "Functionalized SU-8 patterned with x-ray lithography", *J. Vac. Sci. Technol. B*, **23** (6), pp. 2910-2913, 2005.
- [16] Eizi Morikawa, Jaewu Choi, Harish M. Manohara, Hisao Ishii, Kazuhiko Seki, Koji K. Okudaira, and Nobuo Ueno, "Photoemission study of direct photomachining in poly (vinylidene fluoride)", *J. Appl. Phys.*, **87**(8), pp. 4010-4016, 2000.
- [17] Yuichi Utsumi and Takefumi Kishimoto, "Large area and wide dimension range x-ray lithography for lithographite, galvanofomung, and abformung process using energy variable synchrotron radiation", *J. Vac. Sci. Technol. B*, **23** (6), pp. 2903-2909, 2005.
- [18] J. T. Sheu, M. H. Chiang, and S. Su, "Fabrication of intermediate mask for deep x-ray lithography", *Microsystem Technologies*, **4**(2), pp. 74-76, 1998.
- [19] J. Aizenberg, P. V. Braun, P. Wiltzius, "Patterned Colloidal Deposition Controlled by Electrostatic and Capillary Forces", *Phys. Rev. Lett.*, **84**, pp. 2997- 3000, 2000.
- [20] C. Thibault, V. Le Berre, S. Casimirius, E. Trevisiol, J Francois, and C. Vieu, "Direct microcontact printing of oligonucleotides for biochip applications", *Journal of Nanobiotechnology*, **3**, pp. 7-19, 2005.
- [21] C.-F. Chen, S. -D. Tzeng, M. -H. Lin, and S. Gwo, "Electrostatic Assembly of Gold Colloidal Nanoparticles on Organosilane Monolayers Patterned by Microcontact Electrochemical Conversion", *Langmuir* **22**, pp. 7819-7824, 2006.

- [22] E. S. Snow, D. Park, and P. M. Campbell, "Single-atom point contact devices fabricated with an atomic force microscope", *Appl. Phys. Lett.*, **69**(2), pp. 269-271, 1996.
- [23] C. F. Quate, "Scanning probes as a lithography tool for nanostructures", *Surface Science*, **386**(1-3), pp. 259-264, 1997.
- [24] S. Gwo, C.-L. Yeh, P. -F. Chen, Y. -C. Chou, T. T. Chen, T. S. Chao, S. -F. Hu, and T. -Y. Huang, "Local electric-field-induced oxidation of titanium nitride films", *Appl. Phys. Lett.*, **74**(8), pp. 1090-1092, 1999.
- [25] F. S. -S. Chien, C. -L. Wu, Y. -C. Chou, T. T. Chen, S. Gwo, and W. -F. Hsieh, "Nanomachining of (110)-oriented silicon by scanning probe lithography and anisotropic wet etching", *Appl. Phys. Lett.*, **75**(16), pp. 2429-2431, 1999.
- [26] F. S. -S. Chien, J. -W. Chang, S. -W. Lin, Y. -C. Chou, T. T. Chen, S. Gwo, T. -S. Chao, and W. -F. Hsieh, "Nanometer-scale conversion of  $\text{Si}_3\text{N}_4$  to  $\text{SiO}_x$ ", *Appl. Phys. Lett.*, **76**(3), pp. 1-3, 2000.
- [27] Masayoshi Ishibashi, Seiji Heike, and Tomihiro Hashizume, "Dot-Array Resist Patterning Using Scanning Probe Microscopy with a Hybrid Current-Voltage Control Method", *Jpn. J. Appl. Phys.*, **41**, pp. 4395- 4399, 2002.

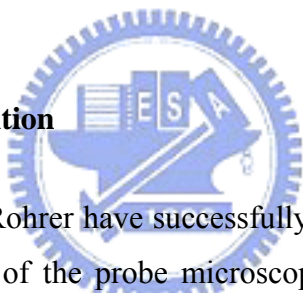


## Chapter 2.

### Scanning Probe Nanolithography

When the lithography skills of the semiconductor industry continues to shrink its design rules, the novel metrology and advanced lithography tools become increasingly important. While the dimensions of the very large scale integration devices are scaled down towards the nanometer region, traditional lithography techniques employing visible light and ultraviolet light confront a serious barrier due to the far-field limitation of the wavelength of light. Scanning probe lithography technique is a direct-writing and resistless novel method with a high resolution from sub-micrometers to nano-meters producing patterns on variety of materials [1, 2], where a conductive AFM probe tip biased with a negative electrical bias relative to the sample surface is used to provide an electric-field local oxidation of the sample surface and modify the chemical characteristics of the sample surface.

#### 2.1 The History of SPM Invention



Dr. G. Binnig and Dr. H. Rohrer have successfully built a scanning probe microscopy (SPM) unique technique, first of the probe microscopy local, called scanning tunneling microscopy (STM) with tunnel effect, which maintains the probe-sample distance with constant tunneling current was invented in 1982 [3, 4]. It was demonstrated that STM could explore the three-dimensional topography of surfaces on atomic scale in air. Its principle consists primarily with scanner a surface with a metal point with current constant as show in Figure 2.1. The tunneling current is an exponential function of the SPM tip-sample surface distance, so it is very sensitive to SPM tip-sample surface distance. The tunneling current is dominated by the single or few atoms at the top of SPM-tip. Therefore, atomic resolution can be reached by STM technique. Beyond the revolution that this invention caused in the field of microscopy and of the physics of surfaces, this new instrument brought the bases for the development of the local probe microscopes. Dr. Binnig and Dr. Rohrer opened a new field in surface science and changed the way to observe the material surface.

Therefore, in 1986, Dr. G. Binnig et al. introduced another apparatus for the surface



characterization microscope with atomic force (AFM) which presents the large one favour to be able to also study insulating materials. [5] Since atomic force microscopy can be applied to any types of material and environment, AFM has thus been used widely in surface characterization. Owing to its atomic scale resolution capability, to probe them mechanical properties, electric, magnetic, electrostatic of one surface, like carrying out local modifications as the lithography, AFM is also the powerful equipment for nano-structure fabrication. Due to Dr. Binnig, Dr. Rohrer and Dr. Ruska they created the remarkable achievements, they were awarded the Nobel Prize in physics in 1986.

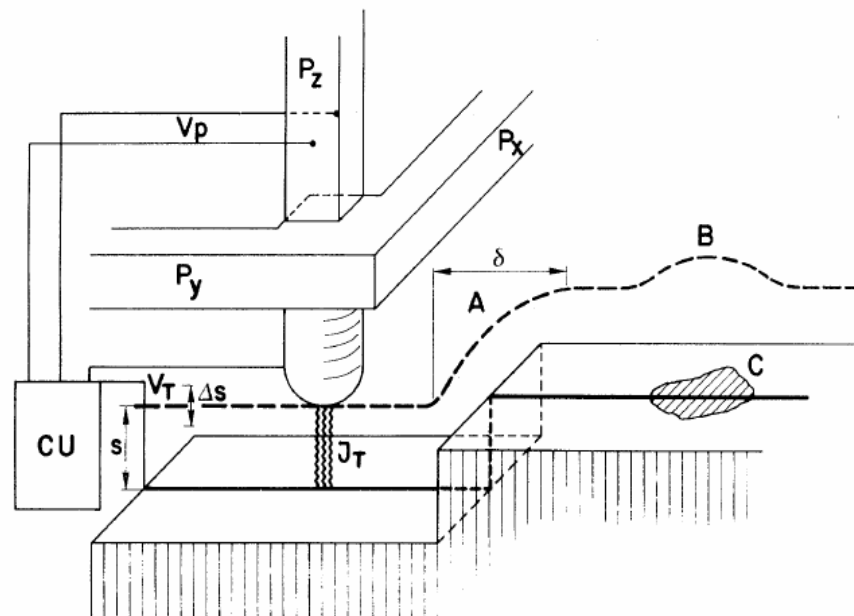


**Figure 2.1** Principle of operation of the scanning tunneling microscope from the original article on the STM [3]. The piezodrives  $P_x$  and  $P_y$  scan the metal tip M to traverse the surface. It describes the operation of the microscope for purpose tunnel effect. The control unit (CU) applies the appropriate voltage  $V_p$  to the piezodrive  $P_z$  for constant tunnel current  $J_T$  at constant tunnel voltage  $V_T$ .

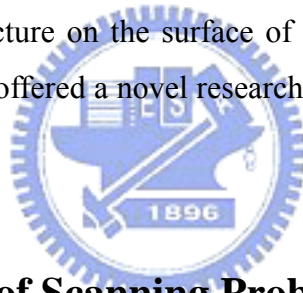
Afterward, the developments and applications of the novel SPM technique began rapidly. In 1990, Dr. J. A. Dagata et al. [6-8] reported that the chemical modification of hydrogen-passivated  $n$ -Si (111) surfaces by a scanning tunneling microscope (STM) operating in air, and direct writing of features with 100 nm resolution was demonstrated. Dagata suggested that field-enhanced oxidation / diffusion occurs at the tip-substrate

interface in the presence of oxygen.

In 1994, Dr. E. S. Snow and Dr. P. M. Campbell reported that an electrically conducting AFM-tip is used to oxidize regions of size 10 ~ 30 nm of the H-passivated Si (100) surface at write speeds up to 1  $\mu\text{m}/\text{sec}$ . This oxide serves as an effective mask for pattern transfer into the substrate by selective liquid etching.

Afterwards, in 1995, Dr. Dawen Wang et al. [10] demonstrated that writing of nanostructures on thin chromium films using atomic force microscopy (AFM). Protruded patterns of various shapes were formed only on the water-adsorbed chromium surface when applying a negative bias on the tip. The smallest feature size obtained is about 20 nm. In 1996, Dr. E. S. Snow et al. [11] also demonstrated that the fabrication of atomic point contacts by using anodic oxidation of thin aluminum films with an atomic force microscope.

Therefore, scanning probe lithography (STM / AFM) technique provides a powerful ability of patterning nano-structure on the surface of semiconductor or on the surface of conductor. SPL technique also offered a novel research theme of lithography process of the integrated circuits.

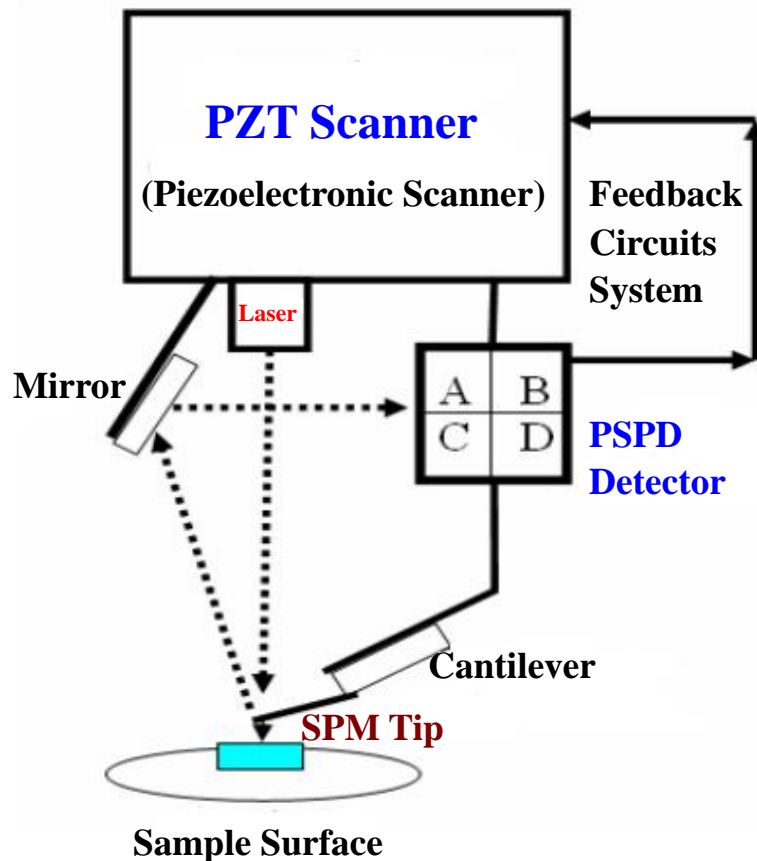


## **2.2 General Principle of Scanning Probe Microscopy (SPM)**

The scanning probe microscopy (SPM) consists of an extremely sharp tip mounted or integrated on the end of a tiny cantilever spring which is moved by a mechanical scanner over the surface to be observed. Every variation of the surface height varies the force acting on the tip and therefore varies the bending of the cantilever. This bending is measured by an integrated stress sensor at the base of the cantilever spring and recorded line by line in the electronic memory. The interaction between tip and sample surface can be compared with the systems pickup.

Most AFM currently detect the bending position of the cantilever with optical techniques as shown in Figure 2.2. The laser beam bounces off the back of the cantilever onto a position-sensitive photodetector (PSPD). As the cantilever bends, the position of the laser beam on the detector shifts. The PSPD itself can measure displacements of light as

small as  $10 \text{ \AA}$ . The ratio of the path length between the cantilever and the detector to the length of the cantilever itself produces a mechanical amplification. As a result, the system can detect sub-angstrom vertical movement of the cantilever tip. The interatomic forces acting on the SPM tip will cause the cantilever to deflect.



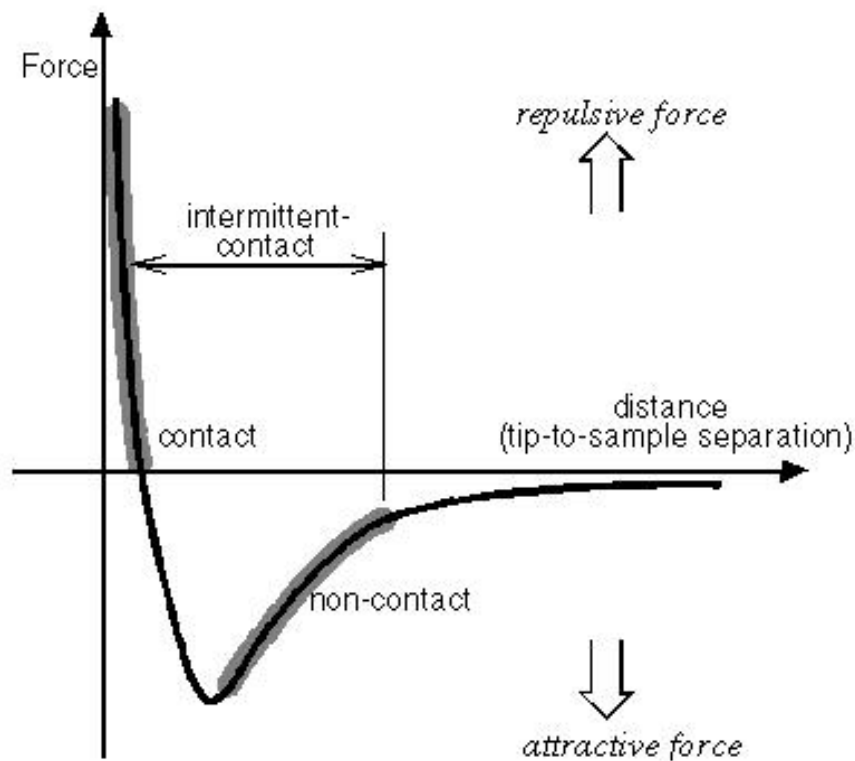
**Figure 2.2** Schematic of the position-sensitive photo detector (PSPD)

Figure 2.3 shows the relationship curves of force vs. distance between SPM tip and sample surface. It was observed that a force is attractive force when the SPM tip-to-sample surface distance was provided with a few micrometers. However, when the SPM tip-to-sample surface distance decreased to small that the force becomes repulsive force, and varied very violently with decreasing very small distance. In the contact regime, the cantilever is held less than a few angstroms from the sample surface, and the interatomic force between the cantilever and the sample is repulsive. In the non-contact regime, the cantilever is held on the order of tens to hundreds of angstroms from the sample surface, and the interatomic force between the cantilever and sample is attractive (largely a result of

the long-range Vander Waals interactions). Both contact and non-contact imaging techniques are described in detail in the following sections.

**Contact Mode:**

In contact-AFM mode, also known as repulsive mode, an AFM-tip makes soft “physical contact” with the sample surface. The AFM-tip is attached to the end of a cantilever with a low spring constant, lower than the effective spring constant holding the atoms of the sample together. As the scanner gently traces the tip across the sample (or the sample under the AFM-tip), the contact force causes the cantilever to bend to accommodate changes in topography.



**Figure 2.3** The relationship curves of interatomic force vs. distance between SPM tip and sample surface.

At the right side of the curve the atoms are separated by a large distance. As the atoms are gradually brought together, they first weakly attract each other. This attraction increases until the atoms are so close together that their electron clouds begin to repel each other

electro-statically. This electro-static repulsion progressively weakens the attractive force as the interatomic separation continues to decrease. The force goes to zero when the distance between the atoms reaches a couple of angstroms, about the length of a chemical bond. When the total Vander Waals force becomes positive (repulsive), the atoms are in contact. A capillary force exerted by the thin water layer often present in an ambient environment, and the force exerted by the cantilever itself. The capillary force arises when water wicks its way around the tip, applying a strong attractive force (about  $10^{-8}$  N) that holds the tip in contact with the surface. Typically, the interatomic force operating range from  $10^{-6}$  N to  $10^{-8}$  N. Contact AFM can record topographic, frictional and elasticity variations with close to atomic resolution, allowing surface measurements and images on a scale beyond the capabilities of conventional microscopes.

### **Non-Contact Mode:**

Non-contact mode AFM (NC-AFM) is one of several vibrating cantilever techniques in which an AFM cantilever is vibrated near the surface of a sample. The spacing between the tip and the sample for NC-AFM is on the order of tens to hundreds of angstroms as shown in Figure 2.3. NC-AFM is desirable because it provides a means for measuring sample topography with little or no contact between the tip and the sample surface. Like contact AFM, non-contact AFM can be used to measure the topography of insulators and semiconductors as well as electrical conductors.

The total force between the tip and the sample in the non-contact regime is very low, generally about  $10^{-12}$  N. This low force is advantageous for studying soft or elastic samples. A further advantage is that samples like silicon wafers are not contaminated through contact with the tip. Because the force between the tip and the sample in the non-contact regime is low, it is more difficult to measure than the force in the contact regime, which can be several orders of magnitude greater. The small force values in the non-contact regime and the greater stiffness of the cantilevers used for NC-AFM are both factors that make the NC-AFM signal small, and therefore difficult to measure. Thus, in non-contact mode, the system vibrates a stiff cantilever near its resonant frequency (typically from 100 to 400 KHz) with the amplitude of a few tens of angstroms. NC-AFM does not suffer from the tip or sample degradation effects that are sometimes observed after taking numerous

scans with contact AFM. So, the NC-AFM is also preferable to contact AFM for measuring soft samples.

### 2.3 The mechanism of SPL field-induced local oxidation

Since the AFM-based field induced oxidation is performed under ambient conditions, a water bridge layer is always present on the sample surface. Sample surface passivation by surface hydrogenation impedes oxidation during the sample exposure to ambient air. As the hydrogen passivation layer can be locally removed by the additional electric field between the tip and the surface. And, the AFM-tip is biased negatively with respect to the sample surface; the sample surface starts to be oxidized when the addition bias exceeded a threshold voltage. The high growth rates occur at extreme electric field strengths near the apex of the AFM-tip of up to  $\sim 10^8$  V/m. Field enhanced thin film oxidation can be modeled by Cabrera and Mott [12].

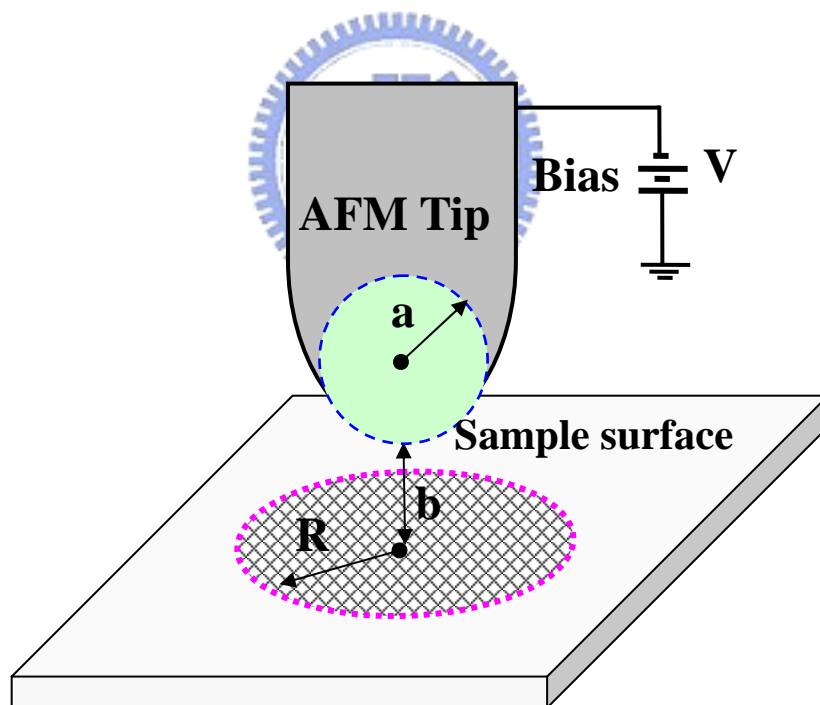


**Figure 2.4** Distribution diagram of electric field exists between the apex of AFM-tip and the substrate surface.

The electric-field within the AFM-tip area can be calculated, assuming that the AFM-tip is considered as a charged sphere above an infinite conducting plane as is done

for a STM tip. Figure 2.4 shows that the distribution diagram of electric field exists between the apex of AFM-tip and the substrate surface. The value of the electric field on the substrate surface located at a distance  $\mathbf{R}$  from the projection on the sample of the apex of the AFM tip, can be expressed as follows [13]:

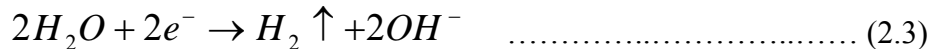
$$E(R) = \frac{a(a+b)(a+2b)}{2b[(a+b)^2 + R^2]^{3/2}} V \dots\dots\dots (2.1)$$

Where  $\mathbf{a}$  is the sphere radius (about 10~15 nm),  $\mathbf{b}$  is the AFM tip-sample surface distances, the electric field is strongly dependent on the AFM-tip-sample distance  $\mathbf{b}$ .

The scanning probe lithography technique is realized by an electro-chemical reaction between the apex of the AFM-tip and the substrate surface, as shown in the Figure 2.5. Two chemical reactions are responsible for oxide formation during scanning probe lithography. Below the breakdown, electrons migrate from the Fermi level of the electrically biased AFM-tip into the water meniscus thus electrochemically reducing the water at the tip-surface interface and yielding hydroxyl ions ( $OH^-$ ) and ( $H^\bullet$ ) radicals as follows [14]:



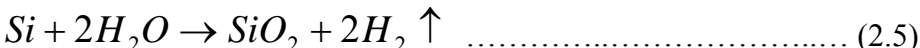
The hydroxyl ions ( $OH^-$ ) are electro-statically attracted to the silicon surface, and produce a silicon-oxide-like ( $SiO_x$ ) pattern. The ( $H^\bullet$ ) radicals may recombine rapidly and form the gas of molecular hydrogen ( $H_2$ ) escaping from the reaction area. The electrochemical reaction near the AFM-tip may be presented as follows:



Thus, an electric current during this reaction has a Faradiac character with conduction provided mainly by the migration of hydroxyl ions. The reaction at the silicon surface can be written as follows:



So, the net electro-chemical reaction of scanning probe lithography resulting in silicon oxidation as follows:



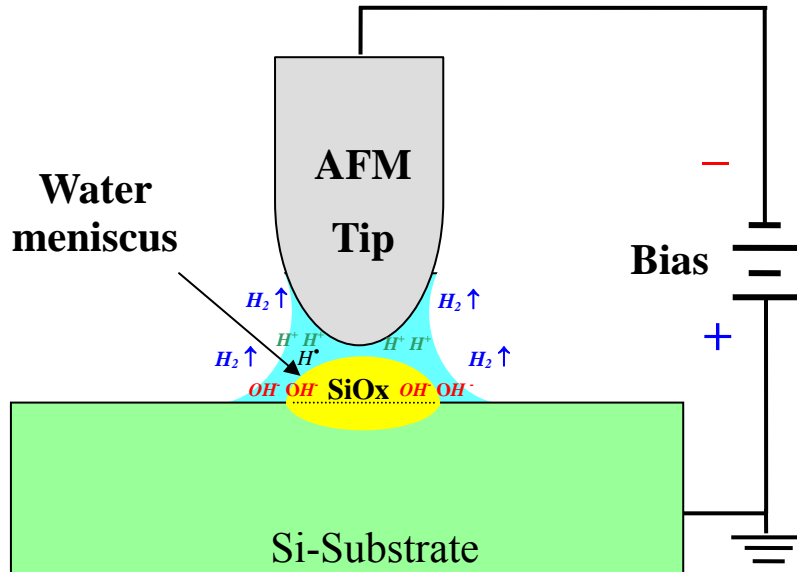


**Figure 2.5** Schematic principle of SPM-based electric-field induced local oxidation process.

## 2.4 Orientation-Dependent Anisotropic Wet Etching

Anisotropic etching of silicon has become an important technology in silicon semiconductor processing during the past ten years. It will continue to gain stature and acceptance as standard processing technology in the next few years. Anisotropic etching of (100) orientation silicon is being widely used today and (110) orientation technology is emerging. This section discusses the orientation-dependent etching of (100) and (110) silicon. Diamond cubic structure model of the silicon taken from three different crystal directions. The (111) direction shows a very high atomic packing density in the (111) plane.

The (100) direction is taken of the same model but moved around  $54.74^\circ$  from the (111) direction, so we can look at a (100) plane. It is readily evident that the atomic packing density is considerably less dense. The (110) direction photo is taken by moving around  $90^\circ$  from the original (111) direction. The atomic packing density is very low in this plane when compared to the {111} plane. From this information, one would expect that the etch rate, or epitaxial deposition growth rate, would be considerably faster in the (110) direction than in the (100) direction and even more so than in the (111) direction [i. e.  $(111) < (100) < (110)$ ].



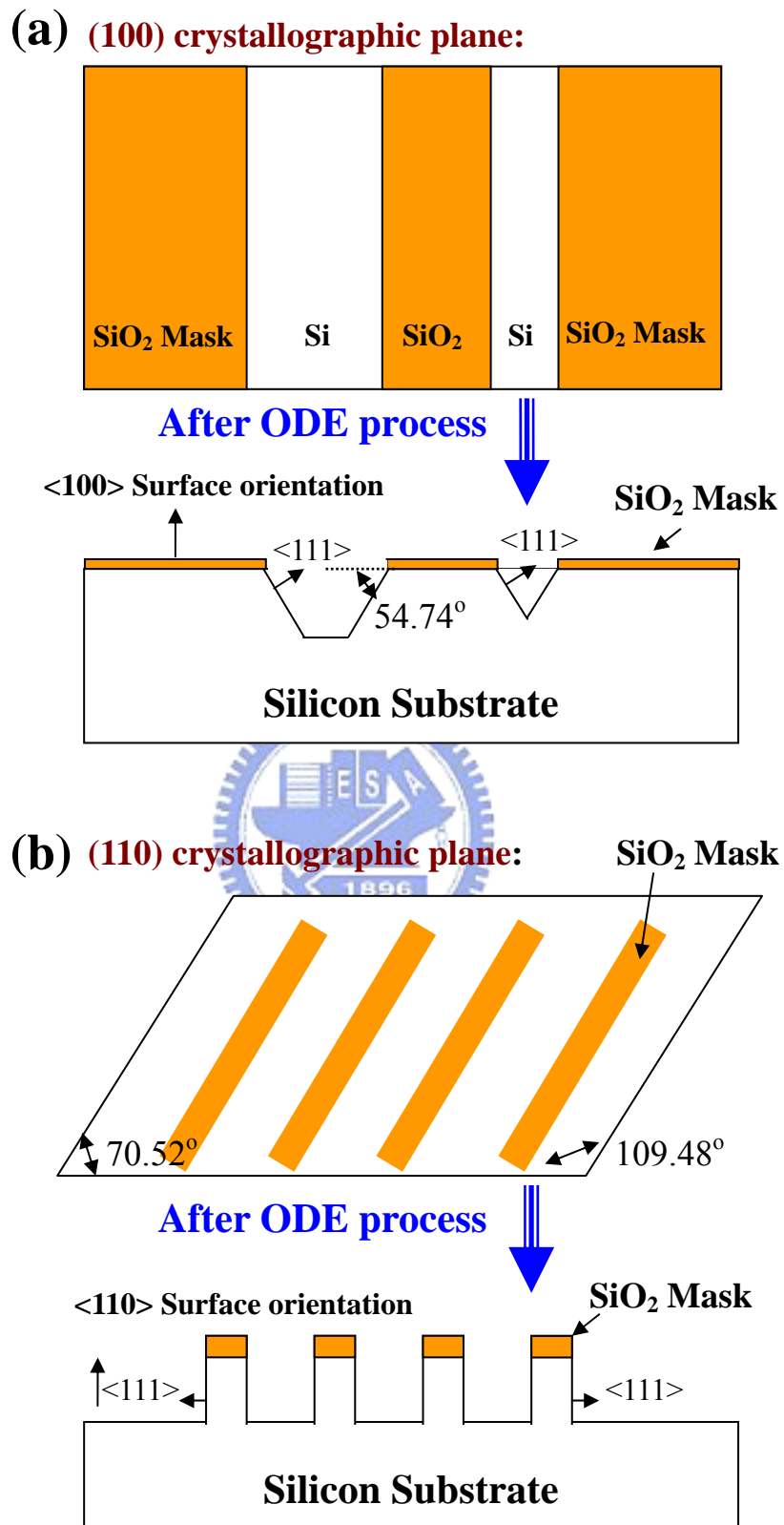


**Figure 2.6** Diagram of orientation-dependent anisotropic wet etching in various orientation silicon planes. (a) (100) crystallographic plane, (b) (110) crystallographic plane.

The etching anisotropy of certain solutions used with this technique is greater than  $[110] : [100] : [111] = 600 : 400 : 1$  etching, making it possible to fabricate virtually any value of aspect ratio trench. On the other hand, Orientation dependent etching (ODE) has the potential to produce a well-defined surface with very large aspect ratios.

The ODE etching process does not attack a particular crystallographic plane as quickly as others, producing a high anisotropic etching. For (100) crystallographic planes, because the (111) plane lays  $54.74^\circ$  to the (100), and perform a V-trench structures (or U-trench structures) as shown in Figure 2.6(a). For (110) crystallographic planes, because the (111) plane lays perpendicular to the (110), allowing for etching of vertical sidewall trench structures as shown in Figure 2.6(b).

## 2.5 Influenced Parameters of SPL Field-induced Oxidation

The strong activity devoted to SPL field-induced oxidation process has revealed some of the relevant factors affecting the oxidation process, by properly changing and control the experimental conditions, such as additional bias between the apex of tip and sample surface, SPM-tip force, SPM-tip scanning speed, and air humidity of patterning environment, etc., SPL oxide patterns with controllable line-widths and heights/depths can be routinely achieved.

### 2.5.1 Additional bias effect between tip and sample surface

Kinetic results are shown in as shown in Figure 2.7, the SPL local oxidized grid lines patterning on the silicon substrate with 10 nN contact force and 1.0  $\mu\text{m}/\text{sec}$  scanning speed at various tip biases ranging from -6 V to -10 V with respect to the sample surface. For sufficiently tip bias, growth of shallow oxides was observed even at -6 V during the  $45 \pm 1\%$  humidity of patterning environment.

Typically, after the first oxide layer forms, the native oxide continues to grow as thick as 7 Å can be attributed to the field assisted Mott-Cabrera mechanism at room temperature. It was suggested that the oxygen diffusion limited electric field corresponding to this native oxide thickness is around  $9 \times 10^7$  V/m. The molar volume expansion ration  $(1 + h / d)$  of the tip bias of ranging from -6 V to -10 V determined by the bulge height  $h$  and the

buried depth  $d$  of the oxide pattern was estimated around 2.86, 2.79, 2.31, 2.43, 2.36, respectively.

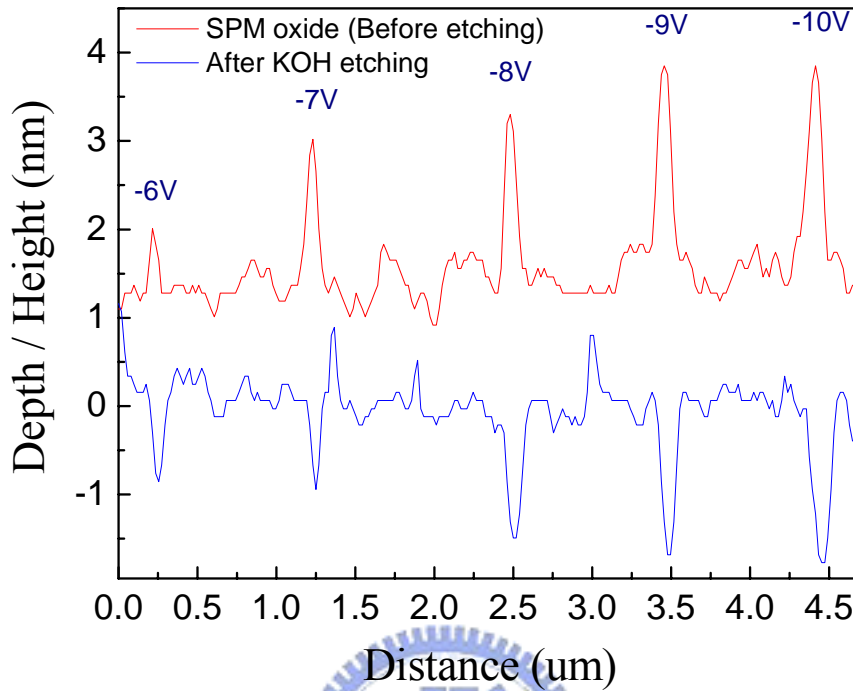


**Figure 2.7** Depth and height of SPL field-induced local oxide patterns varied with additional applied tip voltages from -6 V to -10 V.

It was appeared that the local oxidation volume expansion ration is not proportional to additional tip bias. The oxidation volume expansion ration is much higher than the thermally grown oxide volume expansion ration of 2.27 indicating the SPM-induced local oxidation is less dense than the thermal oxide film. As shown in Figure 2.8, we can find both local oxidation pattern linewidth and height increased as AFM-tip bias increased. It was suggested that the electric field is theoretically exponential proportional to additional tip bias while the tip force, tip scanning speed and humidity were maintained.

The bias dependence of the rate is a clear indication that the electric field plays an important role in the process. The high initial growth rates occur at extreme electric field strengths near the tip apex of up to  $10^8$  V/cm. Field enhanced thin film oxidation can be modeled by Cabrera and Mott. The decrease of the growth rate observed here would then be attributed to the reduction of the electric field strength as the oxide thickness increases. The relation between local oxidation and applied bias can be presented by the

Mott-Cabrera mechanism [15] as following equations:

$$\frac{dx}{dt} \approx \exp\left(-\frac{K_o}{E}\right) \dots\dots\dots (2.6)$$

$$E = \frac{V_{Bias}}{x + x_{gap}} \dots\dots\dots (2.7)$$

$$\frac{dx}{dt} \cong R \times \exp\left(-K_o \frac{(x + x_{gap})}{V_{Bias}}\right) \dots\dots\dots (2.8)$$

Where **R** and **K<sub>o</sub>** are modification fitting factors, **E** is the electric field, **x** is the local oxidation thickness, **x<sub>gap</sub>** is a small gap between tip and sample surface, and **V<sub>Bias</sub>** is applied voltage across the tip and sample surface. It is evident that the growth rate of oxidation is not only a function of electric field strength but also depends on the applied bias. Therefore, both the linewidth and oxide height depend on the voltage applied to the tip during local oxidation patterning, with larger voltages producing larger linewidths and oxide heights.

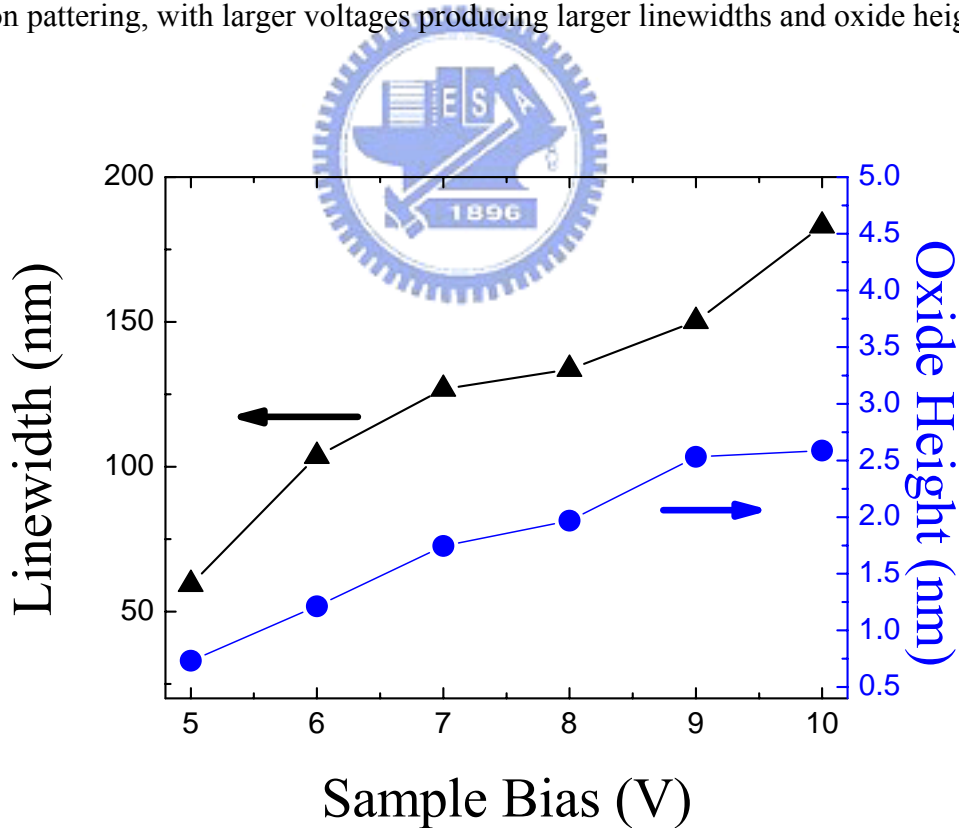


**Figure 2.8** Characteristics curve of linewidth and oxide height of SPL field-induced local oxide patterns varied with different tip voltages from -5 V to -10 V.

## 2.5.2 SPM tip force effect between tip and sample surface

The tip force characteristics curve of local oxidation grid lines as shown in Figure 2.9. The tip bias, tip scanning speed, and ambient humidity were maintained on -9 V, 1.0  $\mu\text{m}/\text{sec}$ , and  $45 \pm 1\%$ , respectively. It was shown that both the local oxidation pattern linewidth and oxide height increased as the tip force increased. It was suggested that the space between tip and silicon surface decreased and the tip vibrated violently as tip force increased. It was appeared that the electric field is theoretically inverse proportional to additional tip force by the equation (2.7). [i. e.  $E \propto V_{\text{Bias}} / X_{\text{Gap}}$ ] Electric field at the tip desorbs the hydrogen atoms and exposes the clean silicon substrate to the water molecules. The oxidation of the exposed surface is enhanced by the electric field. During local oxidation patterning, both the linewidth and oxide height increased as tip force increased.

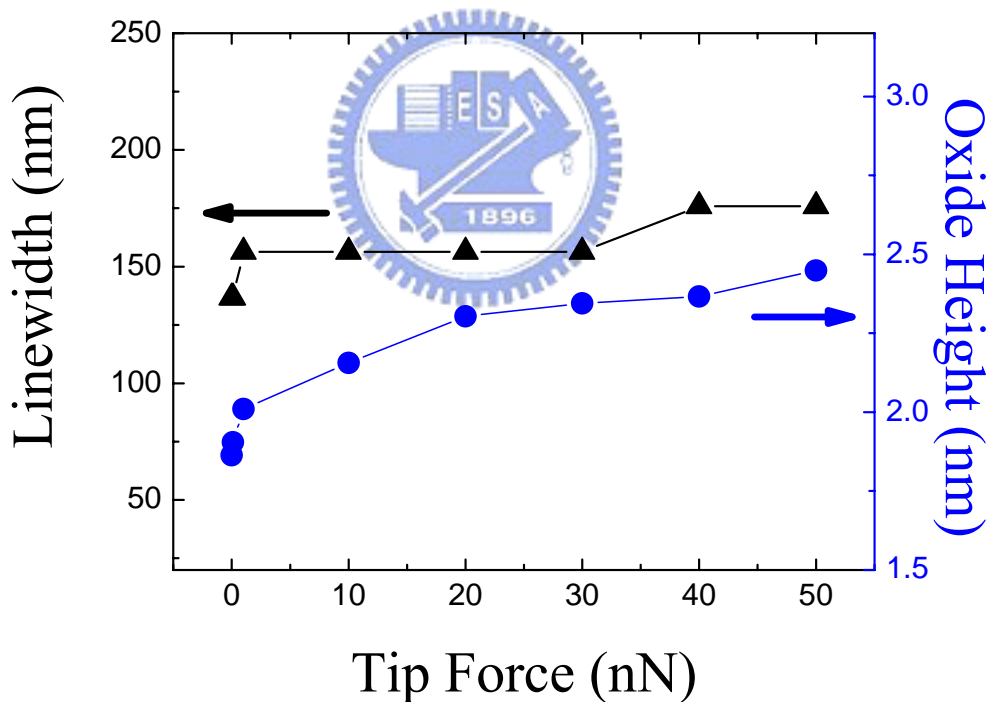


**Figure 2.9** Tip force characteristics curve of local oxidation grid lines. The tip bias, tip scanning speed, and ambient humidity were maintained on -9 V, 1.0  $\mu\text{m}/\text{sec}$ , and  $45 \pm 1\%$ , respectively.

### 2.5.3 Effect of APM-tip scanning speed

SPM-tip scanning speed characteristics curve of local oxidation grid lines as shown in Figure 2.10. The tip bias, tip force, and ambient humidity were maintained on -9 V, 15 nN, and  $45 \pm 1\%$ , respectively. From this result, we can found that both the local oxidation pattern linewidth and oxide height decreased as the tip scanning speed increased.

Typically, the oxide growth rate is theoretically proportional to the oxidation time. This phenomenon was indicated that the SPM-based electric field there's not enough time to induce ample oxygen molecules into silicon surface as operated at higher tip scanning speed. Hence, the SPM-based local oxidation is less dense as the tip scanning speed increased. To optimally use this oxidation process in nanofabrication requires that we understand the factors that control its characteristics. With this in mind, the lateral resolution is determined by the defocusing of the electric field in a condensed water film whose extent is a function of ambient humidity.

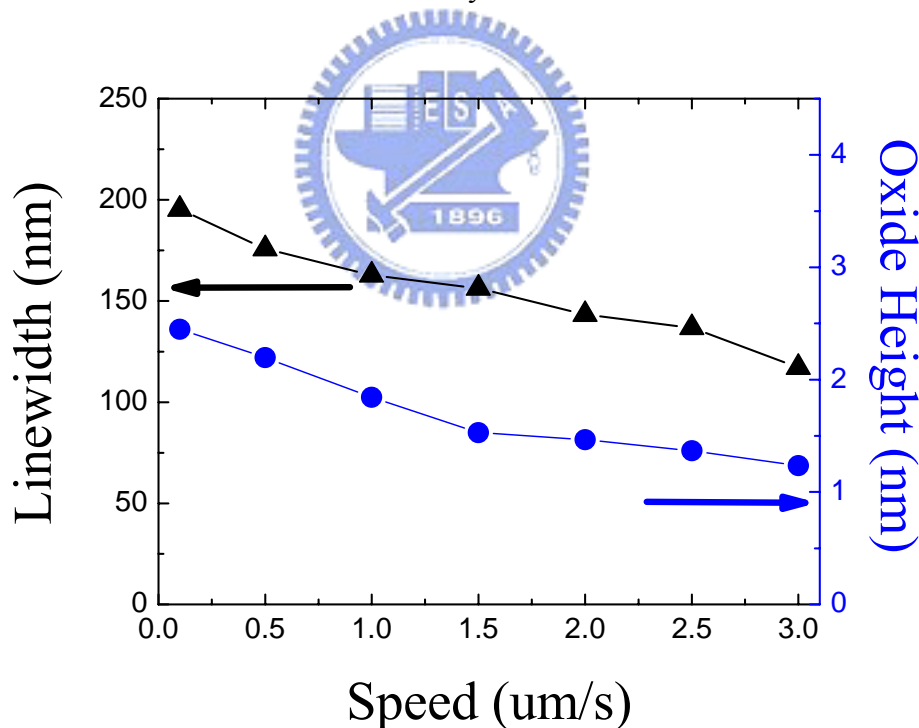


**Figure 2.10** Characteristic curves of oxidation grid lines of effect of scanning speed. The tip bias, tip force, and ambient humidity were maintained on -9 V, 15 nN, and  $45 \pm 1\%$ , respectively.

### 2.5.4 Influence of ambient humidity

Figure 2.11 shows the humidity characteristic curve of oxidation grid lines. The tip bias, tip force, and tip scanning speed were maintained on -9 V, 10 nN, and 1.0  $\mu\text{m/s}$ , respectively. The water bridge provides the pathway for the oxygen species to oxidize the silicon. Both oxide pattern linewidth and oxide height increased as ambient humidity increased. Such results demonstrated the strong influence of external factors on the characteristics of the local oxidation process. Hence, it was suggested that the water film condensed on the surface not only supplies the oxidizing species, but also its finite conductance also leads to a defocusing of the electric field, which degrades the lateral resolution of the local oxidation process.

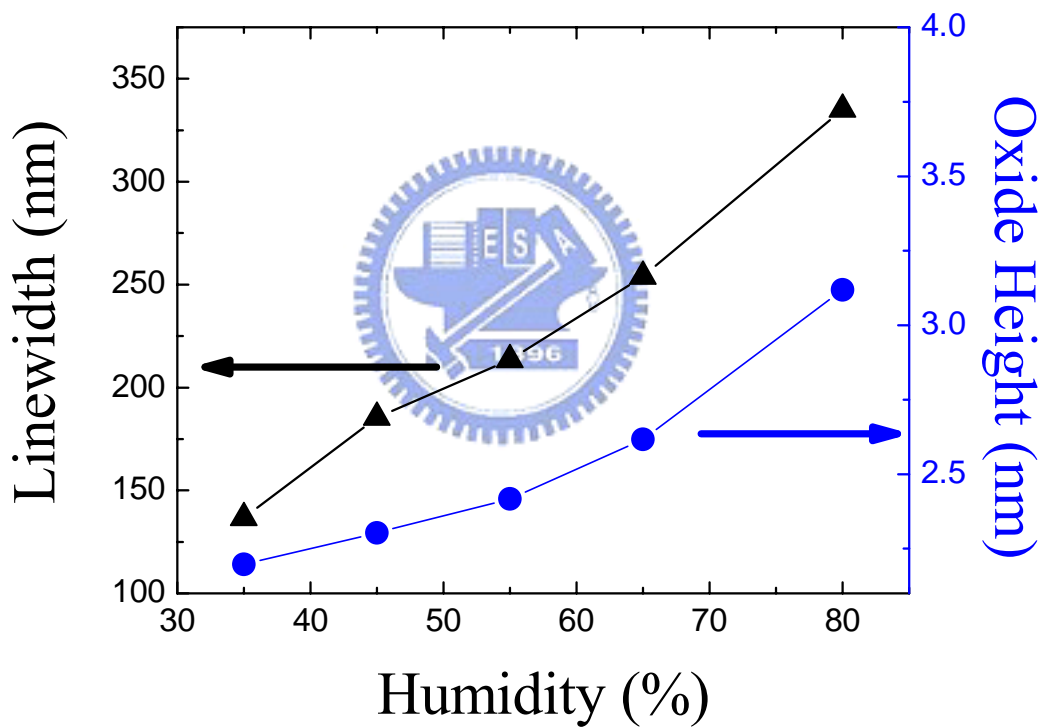


**Figure 2.11** Characteristic curves of oxidation grid lines of influence of ambient humidity. The tip bias, tip force, and tip scanning speed were maintained on -9 V, 10 nN, and 1.0  $\mu\text{m/s}$ , respectively.

### 2.5.5 Influence of etching temperature

Nano-scale local oxidation structures were etched in (110)-oriented silicon substrate by changing the temperature of the KOH solution. It was observed that the etching temperature has considerable influence on the silicon etch rate and the quality of etched surface. The etching rate is theoretically proportional to temperature, the higher the temperature the higher the etching rate as shown in Figure 2.12. Chemical anisotropic etching rate can be presented by following equation:

$$R = R_0 \times \exp\left(-\frac{E_a}{kT}\right) \dots\dots\dots (2.9)$$

where  $R_0$  is modulation parameter of etching rate,  $E_a$  is activation energy of the etching material,  $k$  is Boltzmann constant,  $T$  is etching absolute temperature.

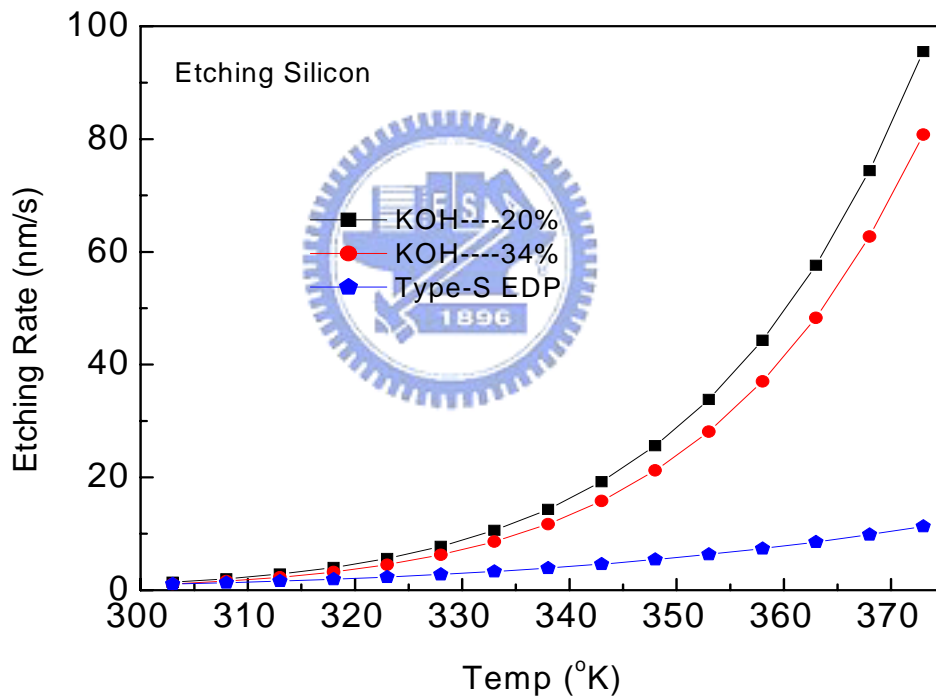


**Figure 2.12** Characteristic relationship curves of etching rate vs. etching temperature.

Owing to both the surface of (110)-oriented planes and the surface of (111)-oriented planes appeared violent attack and etching rate emerged exponential variety increased as etching temperature increased. When the ODE process operated at high etching temperature condition, we can facily make a high aspect ratio nanostructure pattern. However, the sample surface roughness and the morphology obviously deteriorated, and



selective etching ratio also decreased, as etching temperature increased as shown in Figure 2.13.

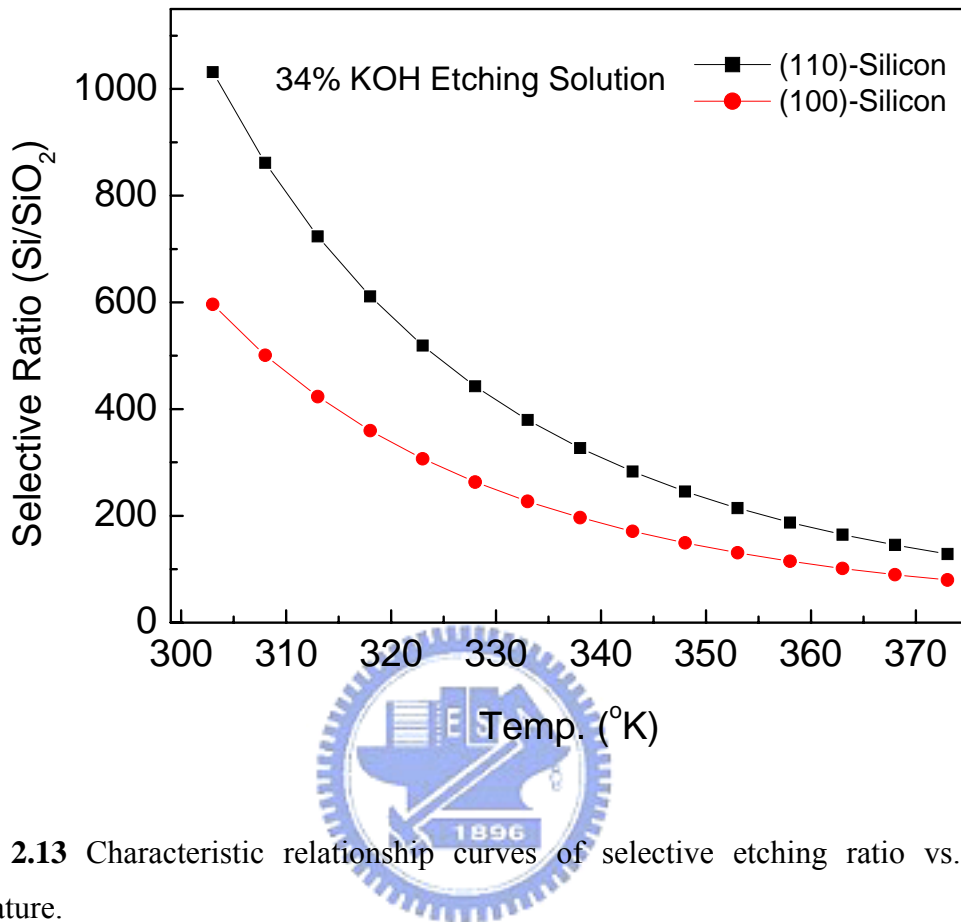


**Figure 2.13** Characteristic relationship curves of selective etching ratio vs. etching temperature.

It was suggested that the reaction mechanism of the chemical wet etching was dominated by mass transfer mechanism during the higher etching temperature condition. On the contrary, when the ODE process operated at low etching temperature condition, we can proper control the etching rate slow down to improve the sample surface roughness and the surface morphology. Nevertheless, the etching rate was too slow to efficiently shrink the linewidth during the lower etching temperature, and the aspect ratio of the nanostructure grid line pattern become worse. Furthermore, it was also found that the additional agitation with 43 KHz by ultrasonic cleaner can speed up mass transfer of chemical reactants on surface of (110)-plane such that improve the surface roughness and morphology as shown in Figure 2.14. In this research, we have successfully demonstrated that using high etching temperature ODE process with the additional agitation to obtain a high aspect ratio, vertical walls, and smooth bottom formation structure pattern.

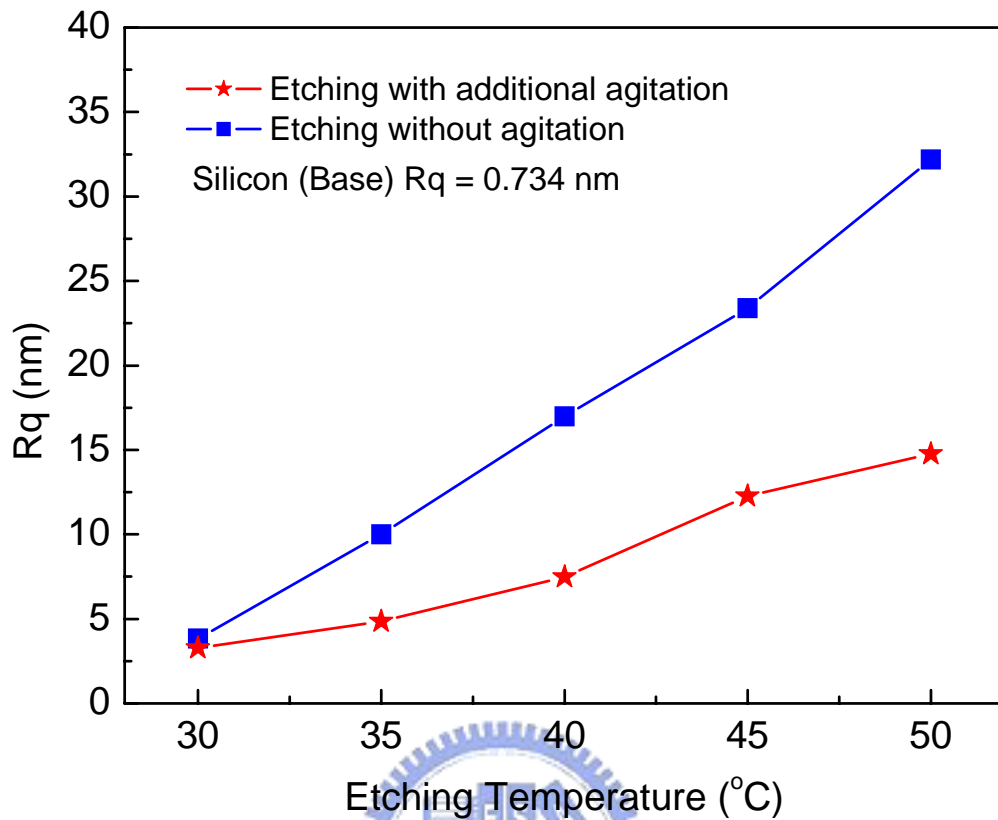


**Figure 2.14** Influence of additional agitation for the surface roughness  $R_q$  (nm) as etching temperature increasing. The silicon (base)  $R_q = 0.734$  nm.

## 2.6 Nanofilter structures fabrication on (100)-Si substrate by using SPL method

In this section, we introduced an interesting technique to fabricate a nanofilter structures on (100)-Si substrate by using the scanning probe lithography with anisotropic wet etching process. Owing to the (100) crystallographic planes which the (111) plane lays  $54.74^\circ$  to the (100) plane, so the (100)-plane ODE etching process removed around  $54.74^\circ$  from the (111)-plane, and we can perform a V-trench structures. Therefore, the combination of SPL nanolithography with anisotropic wet etching process is a highly reliable process for nano-filter structures fabrication. In the Figure 2.15, the nano-filter patterns were generated by SPL method on the (100)-oriented silicon substrate under KOH

anisotropic etching at temperature 50°C for 120 sec. The square nanofilter patterns were clearly performed and the two pairs {111} planes which have an angle 54.74° between (100)-plane and (111)-plane, and this fabrication technique can be further applied in nano-biochemical applications.

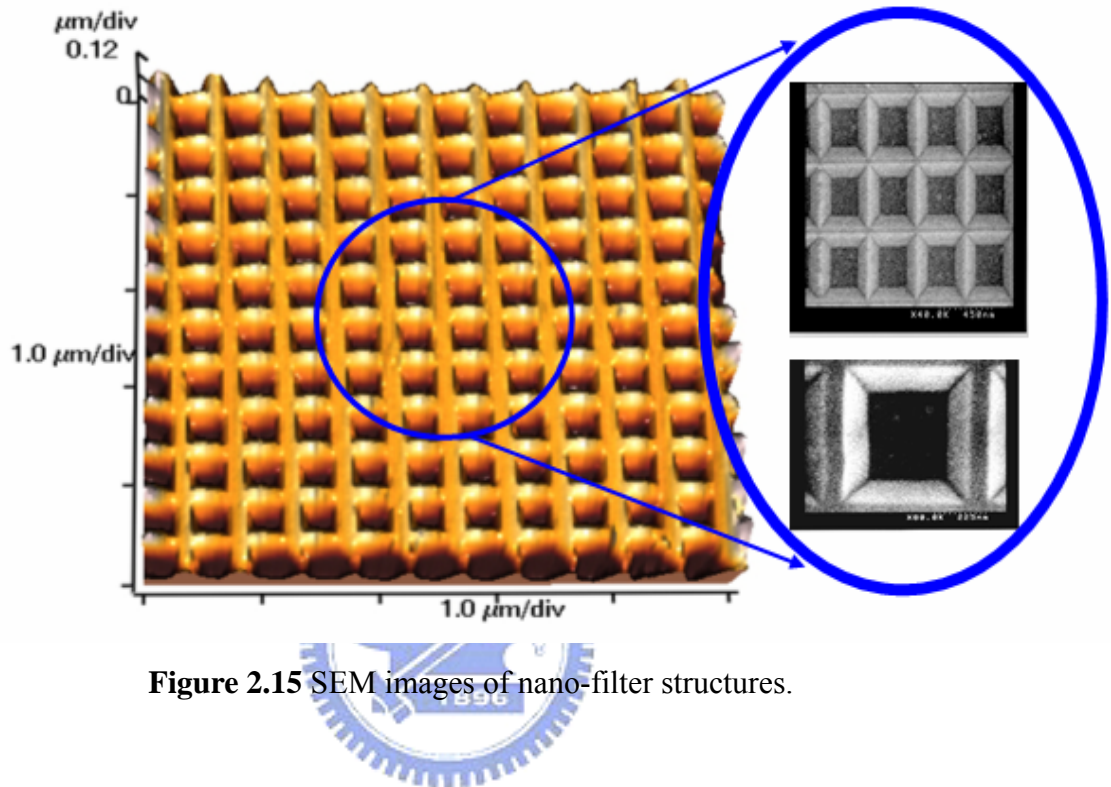


**Figure 2.15** SEM images of nano-filter structures.

## **2.7 Linearity control of Scanning Probe Lithography on (110) Silicon Substrate**

As the semiconductor industry continues to shrink its design rules, new advanced metrology and lithography tools become increasingly important. Recently, scanning probe lithography techniques [16-19] such as the scanning tunneling microscopy (STM) and the atomic force microscopy (AFM) have been used to perform nanometer-scale surface modification and dominated the field of nanometer structures fabrication. Previous reported results [17-19] of linear control of nanostructure patterns transfer into substrate by SPM-based local oxidation with selective wet etching process are not apparently. In this section, we have investigated that the nanostructures fabrication on silicon substrate and successfully demonstrated the ability of nanostructure patterns transfer of linearity

lithography and accurately defined the linewidth of nanostructure patterns and by using SPL technique with KOH solution anisotropic wet etching process. With multipixel scanning of SPL, we can control the pattern width and pattern height of local oxidation and then transferred these patterns into the silicon substrate with wet etching. We have successfully demonstrated accurate linear control of nanostructures fabrication for different linewidth from 25 to 80 nm by SPL technique. The standard deviation ( $1\sigma$ ) for 25 nm nanostructures is 3.01 nm.

### 2.7.1 Linearity control experiment

In this experiment, silicon samples were cut from n-type (110)-oriented Si wafers with a resistivity of around 1~10 ohm-cm. Samples were hydrogen-passivated by dipping in 10 % aqueous HF solution for 15 sec to remove surface native oxide and then blown dry using N<sub>2</sub> gas before performing SPM local oxidation process. The surface roughness (R<sub>q</sub>) of the H<sup>+</sup>-passivated films is around 0.733 nm measured by atomic force microscopy (AFM). Local oxidation was performed in ambient using highly doped Si cantilevers with a resistivity of 0.01~0.0025 ohm-cm and a commercial AFM / STM microscopy (M5 type, Park Scientific Instrument). The diameter of silicon SPM tip is around 10 nm. Oxidation robust masks were formed by applying a sample bias of -8 V to the H<sup>+</sup>-passivated Si (110)-oriented surfaces. Typical, tip speed and tip force are 1.0 μm/s and 0.1 nN, respectively. Owing to the humidity has a key role in controlling the resolution, and the resolution becomes worse with increasing humidity. So, the relative humidity always holds on  $45 \pm 1\%$  during the SPL local oxidation time.

Owing to the orientation-dependent etching (ODE) of (111) crystallographic planes is very slow compared with other planes. For (110) silicon substrate, the ODE process will produce four {111} planes are 90° to the (110) surface plane and perform a very narrow and high aspect ratio grid line nanostructures. The ODE process was done with a 34 wt.% aqueous KOH solution at 50°C. Under these etching conditions, the (110) pure-silicon theorizing etch rate is about 375 nm/min, and the thermally grown SiO<sub>2</sub> theorizing etch rate is about 0.52 nm/min. In this experiment, we will try to control the nano-structure pattern width and height by using the multi-pixel scanning method of the scanning probe lithography (SPL) technique. After KOH selective wet etching, the surface morphology and etch depth structures images were examined by means of a JEOL field-emission

scanning electron microscope (FESEM).

### 2.7.2 Linear control of nanostructures transfer

In the nanostructures fabrication, smooth walls and bottom surface morphology fabrication have been an uphill task during nanostructure patterns performing of (110) silicon substrate due to its orientation-dependent chemical etching process. This section are presented and discussed along with experimental results.

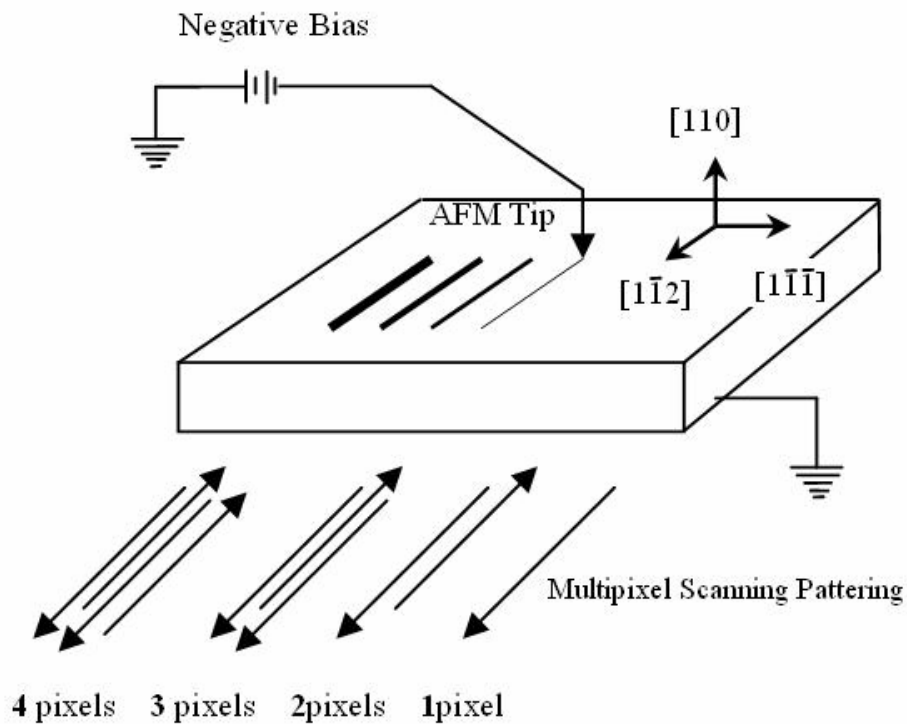


**Figure 2.16** Nanostructure grid line patterns transfer on (110)-Si procedure by using the multipixel scanning method of scanning probe lithography.

The anodic electric-field-enhanced local oxidation patterns are formed with the tip biased negatively with respect to the silicon substrate. For pattern transfer, oxidized samples are etched in a 34 wt. % aqueous KOH solution at 50 °C for 45 sec. In this research, in order to estimate linear control of line nanostructure patterns transfer into (110) silicon substrate, we proper control on tip speed, tip force, tip bias and humidity of

patterning environment. Typical four parameters were maintained 1.0  $\mu\text{m/s}$ , 0.1 nN, -8 voltages and  $45 \pm 1\%$ , respectively. The nanostructure grid line pattern transfer procedure by the multipixel scanning method as shown in Figure 2.16. The pitch of interval between each scanning pixel is 15 nm  $\sim$  40 nm. Utilizing the multipixel scanning method of the SPL to pattern oxide grid line nanostructures on (110)-Si, we can accurately control and define the nano-scale grid line oxidation pattern width and oxidation pattern height.

Shown in Figure 2.17(a) and Figure 2.17(b) are AFM topographic height profiles along the local oxidation nanostructure grid line marked patterns by utilizing the multipixel scanning times and different line / space of the pitch after KOH selective wet etching process for 35 sec. It was appeared that the linearity change increased as multipixel scanning local oxidation times increased. Moreover, it was observed that the nanopattern linewidth variety increased as the line / space of the pitch increased. However, it was also found that the top surface profile of the nanopatterns becomes jagger as the line / space of the pitch increased. It was attributed that the space between pitches is not enough closely knit to withstand the KOH selective wet etching. Consequently, it was considered that proper reduced the line / space of the pitch and harmony with the multipixel scanning times method of the SPL technique can perform the optimal nanostructures and linearity characteristics.

We proper control the multipixel scanning times from 1 to 4 to perform various linewidths of the grid line patterns. The pitch of interval between each scanning pixel is 15 nm. Shown in Figure 2.18 is the SEM micrography of the linear control of line nanopatterns with selective wet etching in a 34 % KOH solution for 45 sec. From the results, we have found that four (111)-oriented sidewalls with a characteristic  $90^\circ$  angle with respect to the (110)-oriented surface. The images of (111)-oriented vertical sidewalls appeared that fairly smooth (111)-oriented surface and excellent parallelism lateral profile could be obtained by SPL technique with selective KOH wet etching process. The average height of the nanostructure patterns is about 200 nm, and the linewidth of the nanostructure patterns are 26.25 nm, 42.19 nm, 63.75 nm, 74.06 nm, respectively by SEM measurement. The linewidth of the nanostructure pattern was shrunk to 27.78 % compared to the FWHM of the original SPM oxidation grid line patterns.

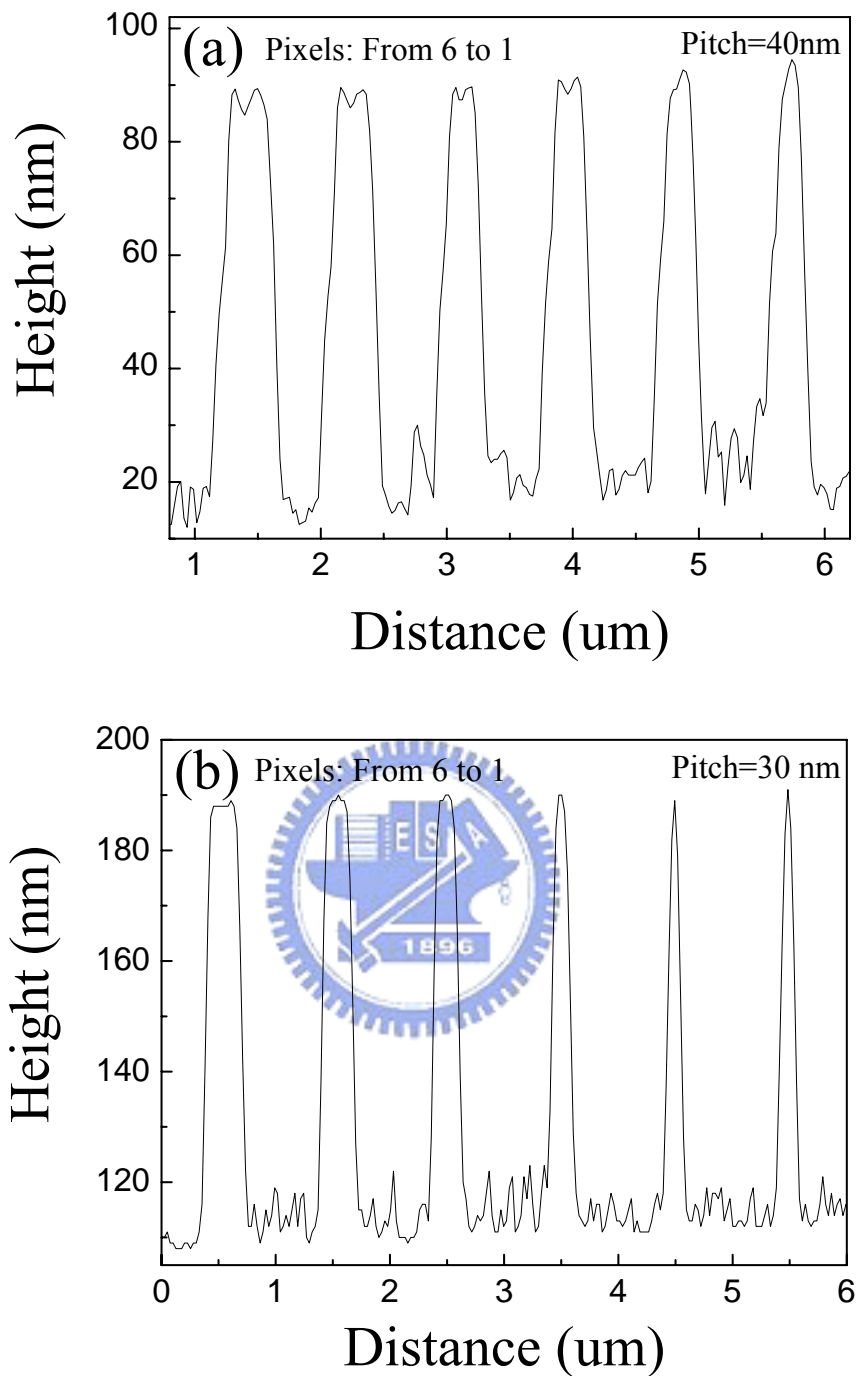


**Figure 2.17** AFM topographic height profiles along the local oxidation nanostructure grid line marked patterns by utilizing the multipixel scanning times and different line / space of the pitch. (a) Pitch = 40 nm; (b) Pitch = 30 nm.

It was considered that both the etching rate of (110)-oriented planes and the etching rate of (111)-oriented planes appeared the exponential variety increased as etching temperature increased. Furthermore, the thickness of oxidation mask edges was defective

and weaker, and it was also caused linewidth shrink during the aqueous KOH anisotropic wet etching process. The volume expansion ration ( $1+h/d$ ) of the tip bias of -8 V determined by the bulge height ( $h$ ) and the buried depth ( $d$ ) of the SPL oxide patterns. It was estimated around 2.31 which were comparable with the thermally grown oxide films is around 2.27 by measuring the AFM images of oxide patterns before and after selective liquid HF wet etching process.

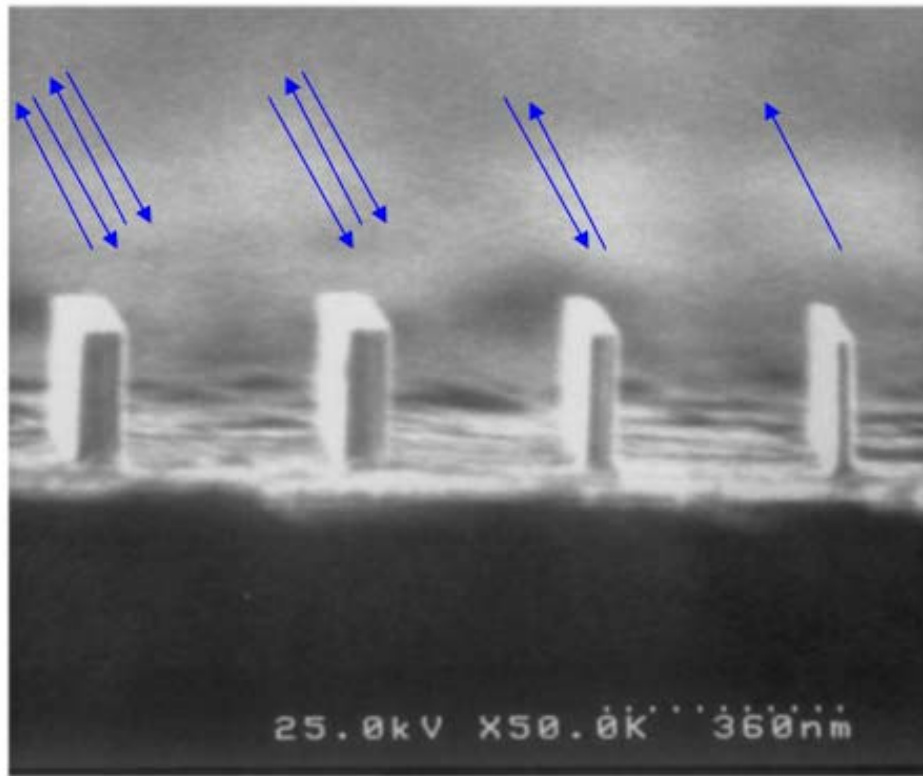


**Figure 2.18** Linear control of pattern transfer of line nanostructure into (110) silicon substrate by SPM-based multipixel scanning local oxidation and wet etching in a 34 % aqueous KOH solution for 45 sec.

Utilizing the multipixel scanning of scanning probe lithography (SPL), we can easily and precisely control the both nanostructure pattern width and nanostructure pattern height of electric-field-enhanced local oxidation and then transferred these patterns into the silicon substrate with aqueous KOH anisotropic wet etching. SPL linearity characteristic curve of the nano-scale grid line patterns after wet etching in a 34 % KOH solution for 45 sec as shown in Figure 2.19.



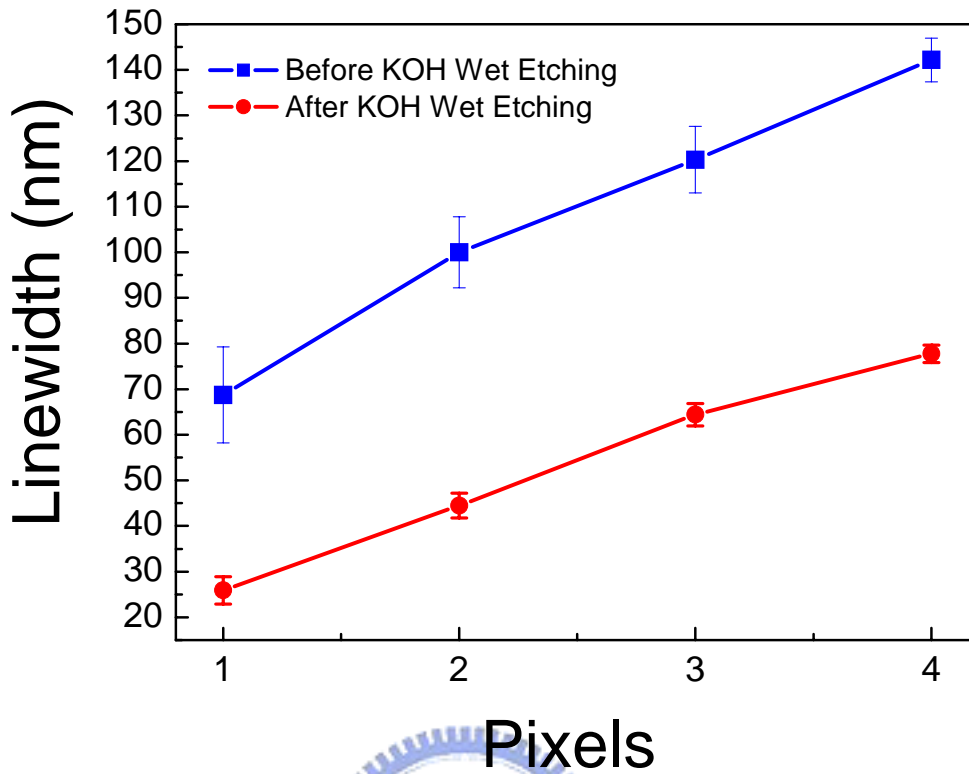


**Figure 2.19** Linearity characteristic curve of oxidation patterns transfer into (110)-silicon wafer by using the scanning probe lithography technique after aqueous KOH anisotropic wet etching process. The pitch of between each scanning pixel is 15 nm.

Nanostructure pattern Gauss distribution illustrations of transferred grid line nanostructure into (110) silicon wafer by using multipixel scanning probe patterning method and anisotropic wet etching as shown in Figure 2.20. Sampling number of nanostructure grid line patterns is thirty, and the average linewidth of one pixel scanning patterning to four pixels scanning patterning is around 25.88 nm, 44.47 nm, 64.41 nm, and 77.76 nm, respectively. The standard deviation is about 3.01 nm, 2.73 nm, 2.45 nm, and 1.93 nm, respectively.

SEM image showing a higher aspect ratio 9.71 : 1. The silicon nanostructure patterns fabricated by SPM-baesd local oxidation with wet anisotropic etching as shown in Figure 2.21. The pattern height is about 191.2 nm and pattern width is about 19.25 nm. The pattern image of the (111)-oriented sidewall was shown that the rational smooth

(111)-oriented surface and excellent vertical standing on the (110)-oriented Si surface plane after selective KOH wet etching process could be obtained by this way. Owing to the orientation-dependent etching of (111) crystallographic planes is very slow compared with other planes. In the most used KOH wet etching process, a high anisotropic etch ratio of greater than  $\{110\} : \{111\} = 600 : 1$  can be routinely obtained. These results show a new technique may be possible to perform reasonably fast, reliable nano-bulges of silicon surfaces for practical applications, such as device nanofabrication and quantum wires using an SPL technique.

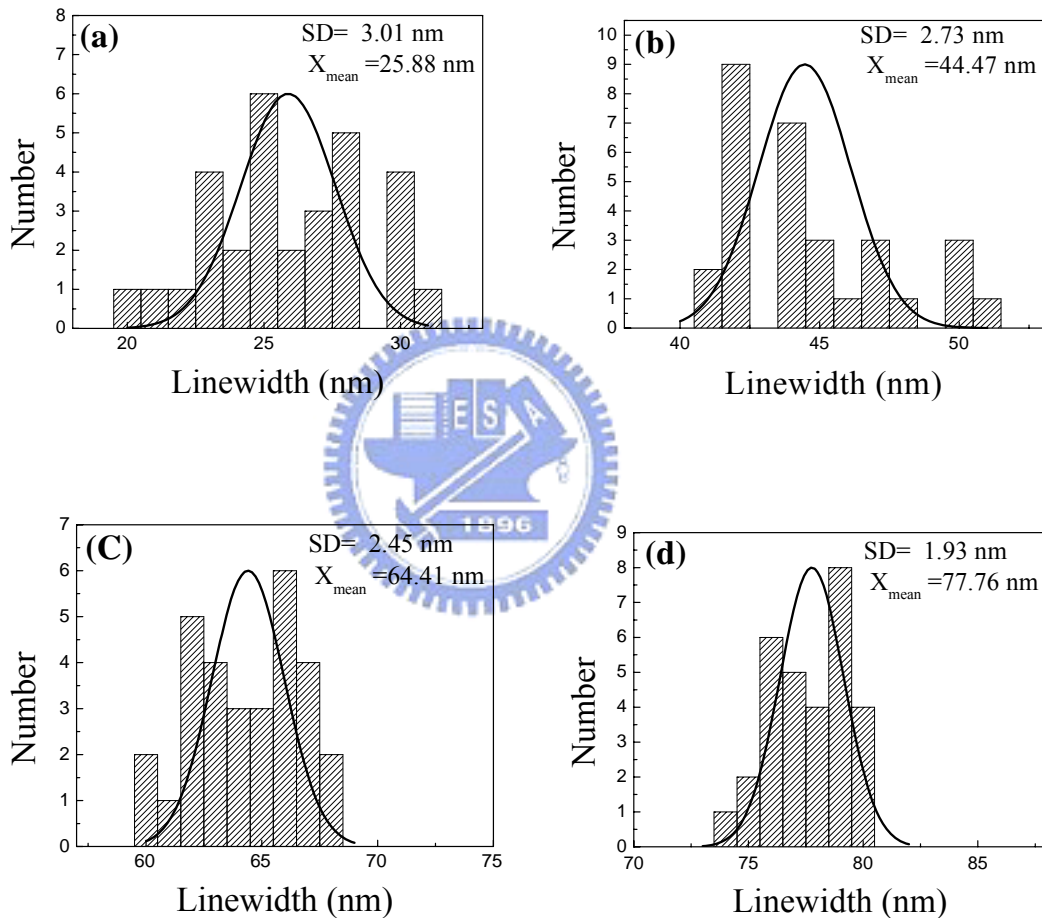


**Figure 2.20** Nanostructure pattern Gauss distribution illustration of transferred grid line nanostructure into (110) silicon wafer by the scanning probe lithography and anisotropic wet etching. (a)one pixel patterning; (b)two pixels patterning ; (c)three pixels patterning; (d)four pixels patterning. The average linewidth is around 25.88 nm, 44.47 nm, 64.41 nm, and 77.76 nm, respectively. The standard deviation is about 3.01 nm, 2.73 nm, 2.45 nm, and 1.93 nm, respectively.

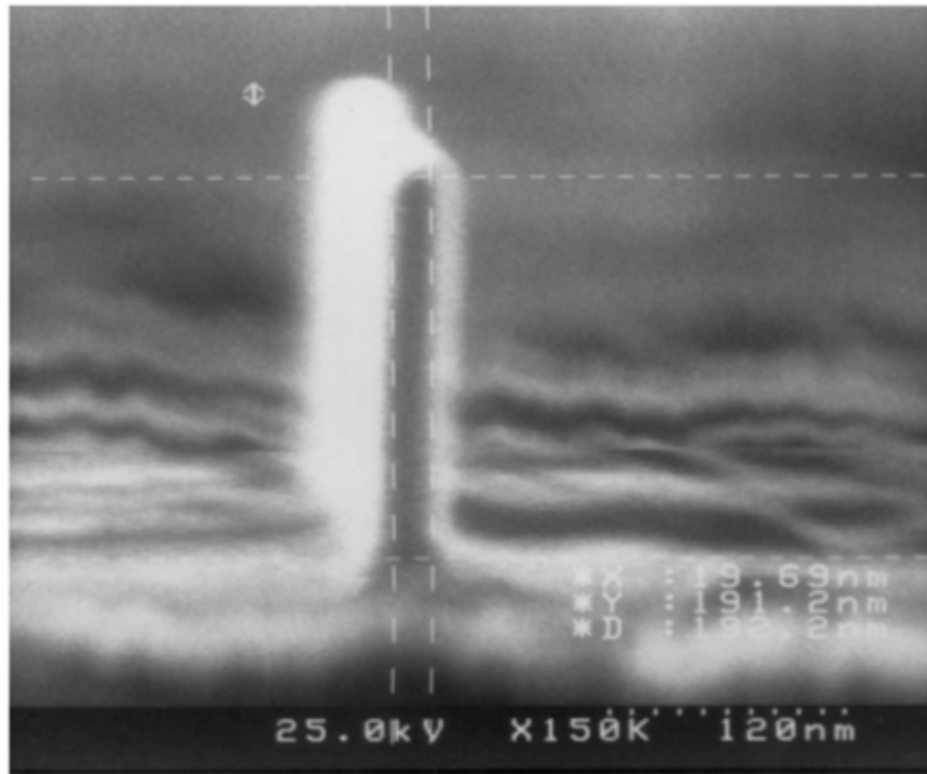


**Figure 2.21** SEM image of the high aspect ratio (9.71 : 1) Si nanostructure fabricated by SPM-based local oxidation and anisotropic wet etching. The pattern height is about 191.2 nm and the pattern width is about 19.69 nm.

From the results, when the multipixel scanning local oxidation times increased, it was obviously found that the standard deviation of the nanostructure grid line patterns transfer into (110)-oriented silicon surface decreased, and the average linewidth of the nano-scale grid line pattern appeared the linearity variety increased. Overall, our results indicated that the use of multipixel scanning method of SPM-based lithography with more potential benefits to perform novel structures for fundamental studies, and nanostructure patterns for linearity studies is comparable to conventional lithography in the nanostructure level.

## 2.8 Summary

Nanostructures and nanodevices fabrication of on single-crystal silicon have been demonstrated by electric-field-enhanced local oxidation on the semiconductor materials using the scanning probe lithography (SPL). We have successfully demonstrated accurate linear control of nanostructures fabrication for different linewidth by using the multipixel scanning method of SPL technique with ODE etching process, and feature size of desired nanopattern down to 20 nm can be easily obtained under control. We have successfully demonstrated accurate linear control of nanostructures fabrication for different linewidth from 25 nm to 80 nm by SPL technique. The standard deviation ( $1\sigma$ ) for 25 nm nanostructures is 3.01 nm. It was indicated that the use of multipixel scanning method of SPL with more potential benefits to perform novel structures for fundamental studies of nanostructure, nano-patterning for linearity studies, and there is the possibility of using these techniques for practical applications, such as device nanofabrication and nanoelectronics.



## Reference

- [1] J. A. Dagata, "Device fabrication by scanning probe oxidation", *Science* **270**, p. 1625, 1995.
- [2] E. S. Snow, P. M. Campbell and F. K. Perkins, "Nanofabrication with proximal probe", *Proc. IEEE* **85**, pp. 601-611, 1997.
- [3] G. Binnig, H. Rohrer, Ch. Gerber and E. Weibel, "Surface Studies by Scanning Tunneling Microscopy", *Phys. Rev. Lett.*, 49, pp. 57-61, 1982.
- [4] G. Binnig, H. Rohrer, C. To stack, E. Weibel, " $7 \times 7$  rebuilding one Si(111) resolved in real space", *Phys. Rev. Lett.*, **50**, pp. 120-123, 1983.
- [5] G. Binnig, C. F. Quate and Ch. Gerber, "Atomic Force Microscope", *Phys. Rev. Lett.*, **56**, pp. 930-933, 1986.
- [6] J. A. Dagata, J. Schneir, H. H. Harary, C. J. Evans, M. T. Postek, and J. Bennett, "Modification of hydrogen-passivated silicon by a scanning tunneling microscope operating in air", *Appl. Phys. Lett.*, **56**(19), pp. 2001-2003, 1990.
- [7] E. S. Snow, P. M. Campbell, and P. J. McMarr, "Fabrication of silicon nanostructures with a scanning tunneling microscope", *Appl. Phys. Lett.*, **63**(6), pp. 749-751, 1993.
- [8] E. S. Snow and P. M. Campbell, "Fabrication of Si Nanostructures with and AFM", *Appl. Phys. Lett.* **64**(15), pp. 1932-1934, 1994.
- [9] P. M. Campbell, E. S. Snow, P. J. McMarr, "Fabrication of Nanometer- Scale Si Side-Gated Transistors with and AFM", *Appl. Phys. Lett.* **66** (11), pp. 1388-1390, 1995.
- [10] Dawen Wang, Liming Tsau, K. L. Wang, and Peter Chow, "Nanofabrication of thin chromium film deposited on Si(100) surfaces by tip induced anodization in atomic force microscopy", *Appl. Phys. Lett.* **67** (9), pp. 1295-1297, 1995.
- [11] E. S. Snow, D. Park, and P. M. Campbell, "Single-Atom Point Contact Devices Fabricated with and AFM", *Appl. Phys. Lett.* **69**(2), pp. 269-271, 1996.
- [12] N. Cabrera and N. F. Mott, "Theory of the oxidation of metals", *Repts. Progr. Phys.* **12**, pp.163-184, 1949.
- [13] F. Marchi, V. Bouchiat, H. Dallaporta, V. Safarov, D. Tonneau, and P. Doppelt, "Growth of silicon oxide on hydrogenated silicon during lithography with an atomic force microscope", *J. Vac. Sci. Technol. B*, **16**(6), pp. 2952-2956, 1998.

- [14] S. F. Lyuksyuto, P. B. Paramonov, I. Dolog, R. M. Ralich, “Peculiarities, of an anomalous electronic current during atomic force microscopy assisted nanolithography on n-type silicon”, *Nanotechnology*, **14**, pp. 716-721, 2003.
- [15] E. S. Snow, G. G. Jernigan, and P. M. Campbell, “The kinetics and mechanism of scanned probe oxidation of Si”, *Appl. Phys. Lett.*, **76**(13), pp. 1782-1784, 2000.
- [16] C. F. Quate, “Scanning probes as a lithography tool for nanostructures”, *Surface Science*, **386**(1-3), pp. 259-264, 1997.
- [17] S. Gwo, C.-L. Yeh, P. -F. Chen, Y. -C. Chou, T. T. Chen, T. S. Chao, S. -F. Hu, and T. -Y. Huang, “Local electric-field-induced oxidation of titanium nitride films”, *Appl. Phys. Lett.*, **74**(8), pp. 1090-1092, 1999.
- [18] F. S. -S. Chien, C. -L. Wu, Y. -C. Chou, T. T. Chen, S. Gwo, and W. -F. Hsieh, “Nanomachining of (110)-oriented silicon by scanning probe lithography and anisotropic wet etching”, *Appl. Phys. Lett.*, **75**(16), pp. 2429-2431, 1999.
- [19] F. S. -S. Chien, J. -W. Chang, S. -W. Lin, Y. -C. Chou, T. T. Chen, S. Gwo, T. -S. Chao, and W. -F. Hsieh, “Nanometer-scale conversion of  $\text{Si}_3\text{N}_4$  to  $\text{SiO}_x$ ”, *Appl. Phys. Lett.*, **76**(3), pp. 1-3, 2000.



## Chapter 3.

### Dip-Pen Nanolithography

Dip-Pen Nanolithography (DPN) is a scanning probe nanopatterning technique in which an AFM-tip is used to deliver molecules to a surface via a solvent meniscus, which naturally forms in the ambient atmosphere. DPN is a direct-write soft lithography technique that is used to create nanostructures on a substrate of interest by delivering collections of molecules via capillary transport from an Atomic Force Microscope (AFM) tip to a surface as shown in Figure 3.1. This direct-write technique offers high-resolution patterning capabilities for a number of molecular and biomolecular ‘inks’ on a variety of substrates, such as metals, semiconductors, and monolayer functionalized surfaces. It is becoming a work-horse tool for the scientist interested in fabricating and studying soft-and hard-matter on the sub-100 nm length scale.

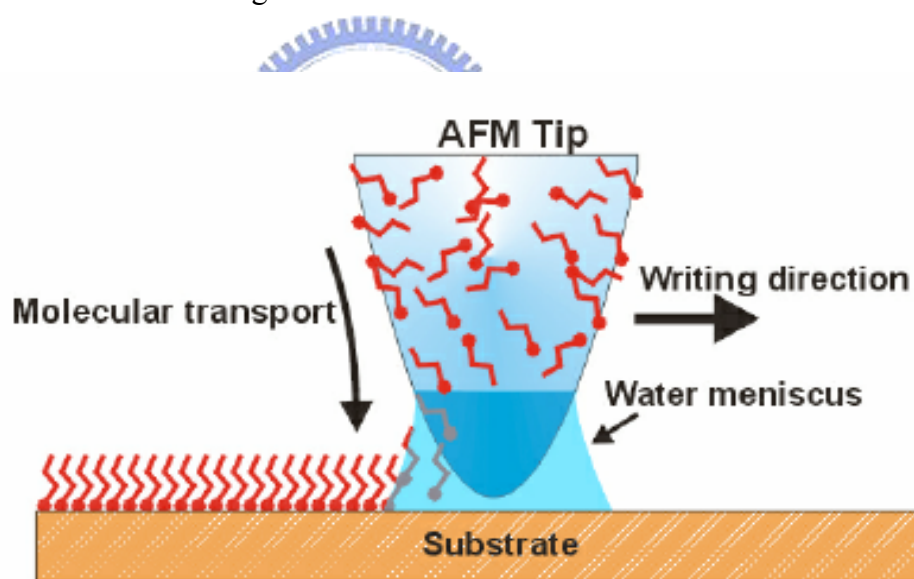


**Figure 3.1** Schematic representation of Dip-Pen Nanolithography (DPN). Transport mechanism of molecules to the surface via the water meniscus forms between the AFM-tip and the sample surface in air. [1]

Using the conventional atomic force microscope it is possible to achieve ultra-high-resolution features as small as 15 nm line widths and ~ 5 nm spatial resolutions. For nanotechnology applications, it is not only important to pattern molecules in high

resolution, but also to functionalize surfaces with patterns of two or more components. One of the most important attributes of DPN is that because the same device is used to image and write a pattern, patterns of multiple molecular inks can be formed on the same substrate in very high alignment.

### **3.1 Introduction of dip-pen lithography applications**

In recent years, several lithography methods such as electron-beam lithography, photo-lithography, ion beam lithography [2], scanning probe lithography [3], micro-contact printing [4], and nano-imprint lithography [5] offer one the ability to build nano-structures on this scale of length, but none of these allow one to deposit molecule-based nanostructures directly on a surface especially on the oxide surface [6-8]. Dip-pen nanolithography (DPN) is a nano-writing procedure that utilizes the tip of an atomic force microscope as a “nano-pen” to transport an “ink” containing organic molecules onto a substrate surface via a water meniscus. Using the same AFM-tip to write and subsequently read patterns, it is possible to create nanoscale patterns with remarkable resolution (<100 nm) and simultaneously control the chemical functionality of the written regions [9]. Dip-pen nanolithography technique has emerged as a useful tool that allows one to make multi-component nanostructures on a surface with near-perfect registration capabilities. This makes DPN a unique tool that can be used to fabricate both hard and soft structures with nano-scale precision on the semiconductor substrate [8, 10]. On the other hand, dip-pen nanolithography (DPN) allows one to fabricate one molecule thick nanostructures with feature size from micron to sub-100 nm dimensions on solid substrates [11]. Preparation of metal nano-clusters on the various substrates is a key issue in all fields of modern science and technology covering microelectronics, photonics, biochemical sensors, nano-technologic devices, and so forth.

In the field of nanoscience and technology, functionalized inorganic metallic nano-structures have been widely studied because of their potential applications in electronic devices [12, 13], photonics [14-16], and biodiagnostics [17-20]. Recently, one of the major themes of nanotechnology has been the search for techniques for self-assembling nano-particles to construct architectures on a solid-state surface for different applications. Techniques to make low-dimensional assemblies of colloidal nanoparticles to fabricate



nanostructures are essential for developing and capitalizing upon the emerging field of nanoscience [7, 10]. In 2004, Dr. Y. Cui [13] et al. reported the effective assembly of very small nanostructures using the capillary force method; nano-particles were selectively forced into lithographically defined nano-fillisters but no particles were deposited on the surrounding areas. Dr. J. Zheng [21] et al. reported that an octadecyltrichlorosilane (OTS) self-assembled monolayer (SAM) was formed on silicon by immersing the silicon substrate in OTS solution. Localized oxidation of the OTS-covered silicon substrate was carried out with a commercial AFM-tip. An amino-terminated propyltriethoxysilane (APTES) monolayer was selectively formed on lithographically created silicon oxide regions by soaking the substrate in APTES solution. Dr. Hun Zhang [8] et al. developed a method for fabricating arrays of gold nanostructures on a solid surface based on dip-pen nanolithography (DPN) and wet chemical etching. A 16-mercapto-hexadecanoic acid (MHA)-coated tip was prepared by immersing a commercial  $\text{Si}_3\text{N}_4$  tip into the MHA solution. Each pattern was generated via DPN with a MHA-coated tip in contact with gold surface. Thiol-functionalized molecules, like 2-aminoethanethiol ( $\text{HS}-\text{C}_2\text{H}_4-\text{NH}_2$ ) (AET), were used to modify these nanopatterns. After the AET-modified nanostructures were immersed into a solution of citrate-stabilized gold nanoparticles, a monolayer of gold nano-particles localized on each of the AET-modified nanopatterns on the gold substrate surface. Except for micro-contact printing [22], many lithography methods, such as electron-beam lithography, photo-lithography, ion beam lithography [2], scanning probe lithography [5], and nano-imprint lithography[3], offer one the ability to build nano-structures on this scale of length, but none of these methods allow one to deposit molecule-based nanostructures directly on a surface, especially on an oxide surface.

DPN utilizes the tip of an atomic force microscope as a “nano-pen” to transport an “ink” containing organic molecules onto a substrate surface via a water meniscus. DPN allows one to fabricate one-molecule-thick nanostructures with feature sizes from micron to sub-100 nm dimensions on solid substrates. This makes DPN a unique technique that can be used to fabricate both hard and soft structures with nano-scale precision [9] and it has also emerged as a useful tool that allows one to make multi-component nanostructures on the sample surface [11].

### 3.2 Impact of UV-induced production of gold nanoclusters on the SiO<sub>2</sub> surface of SiNWs by using DPN technique

Dip-pen nanolithography (DPN) was adopted to provide HAuCl<sub>4</sub> ink (7.5 mM) on the surface of SiO<sub>2</sub>/Si samples and followed by UV light-induced reduction of gold ions on the area of interest such that gold nanoclusters formed selectively. X-ray photoelectron spectroscopy (XPS) was then used to evaluate the surface chemical composition before and after 365 nm UV light irradiation of gold salt on the surface of oxide/silicon. UV-induced reduction of the gold ions (Au<sup>3+</sup>) and aggregation of gold nanoclusters (Au<sup>0</sup>) on the SiO<sub>2</sub>/Si surface were observed.

UV irradiation resulted in decrease in the binding energy and the changes in the width of the Au4f peak corresponding to Au<sup>0</sup>. The silicon nanowires (SiNWs) with 100 nm wide and 2 μm long on the n-type (100) SOI substrate were fabricated by the scanning probe microscope (SPM)-based local oxidation technique and followed by wet etching with tetramethylammonium hydroxide (TMAH) solution. HAuCl<sub>4</sub> ink was then selectively provided by DPN on the native oxide surface of SiNWs and followed by electrical property measurements. The thickness of the gold nanoclusters, estimated less than 1nm, was observed by lateral force microscopy (LFM). I<sub>d</sub>-V<sub>ds</sub> characteristics demonstrated that the conductance of SiNWs increased two times at 0.5 volts of V<sub>ds</sub> after DPN of gold nanoclusters. DPN of gold nanoclusters on the oxide surface of SiNWs enhanced carriers transport in the channel of n-type silicon nanowires. It is believed that the proposed nanofabrication technique can be further applied in both nanoelectronics and nanobio applications. In this 3.2 section, we report a successful technique for using DPN technique to write molecule ink (HAuCl<sub>4</sub>) structures directly onto oxidized surfaces of silicon nanowires (SiNWs). The silicon nanowires were performed based on scanning probe lithography (SPL) technique and anisotropic tetramethylammonium hydroxide (TMAH) wet etching were expressed. Utilizing the HAuCl<sub>4</sub> solution as an ink in a conventional DPN procedure, we can directly generate monolayer nano-patterns onto oxidized silicon surface.

Furthermore, it was demonstrated that UV light-induced reduction of gold ions on the region of interest such that gold nanoclusters formed selectively. It is believed that the

proposed nanofabrication technique combined DPN method with the self assembled monolayer (SAMs) process can be further applied in both nano-electronics and nano-biochemical sensors applications.

### **3.2.1 Experiment details of the UV-induced production of gold nano-clusters with DPN lithography**

The main key of this research was a detailed investigation of the UV light-induced reduction of gold ions deposited from an aqueous  $\text{HAuCl}_4$  ink solution onto a silicon nanowire by using dip-pen lithography method. In our experiment, first, the silicon wafer was cleaned by using standard RCA cleaning process to remove surface organic contamination. After wafer cleaning, a thermal oxidized  $\text{SiO}_2$  layer of 30 nm thick was formed. Then, the sample was immersed into the  $\text{HAuCl}_4$  solution for 10 min, and baked at 120 °C for 30 min in a hot-plate. XPS analysis was then used to evaluate the surface chemical composition before and after 365 nm UV light irradiation of gold salt on the surface of oxide/silicon. Afterward, we have performed the silicon nanowire with 100 nm width and 2  $\mu\text{m}$  length on an n-type (100) SIMOX SOI wafer with 50-nm-thick silicon and 150-nm-thick buried silicon dioxide by using the scanning probe microscope (SPM)-based local oxidation technique in ambient using PtIr tip (tip diameter =10 nm) for SiNW oxide patterns. SiNWs were generated by tetramethylammonium hydroxide (TMAH) anisotropic wet etching procedure. Then,  $\text{HAuCl}_4$  ink-coated tips was prepared by immersing a commercial PtIr tip (tip diameter =10 nm) into a 7.5 mM solution for 60 sec for following DPN procedure. DPN experiments were carried out under ambient conditions (set point = 1.0 V,  $25 \pm 1$  °C, 85 % relative humidity) by using an commercial atomic force microscopy, and a commercial lithography software (NSCRIPTOR, DPN Writer<sup>TM</sup>, NanoInk Inc.) with a  $\text{HAuCl}_4$  ink-coated tip. We are utilizing an inked 7.5 mM  $\text{HAuCl}_4$  AFM-tip to deposit gold nano-clusters on the surface of the silicon nanowire, it is in fact possible to write nano

-scopic patterns of reactive  $\text{HAuCl}_4$  production on the silicon nanowires (SiNWs) with proper control of tip scan speed, tip force, and relative humidity environment. After DPN writing procedure, the sample was baked at  $120\text{ }^\circ\text{C}$  for 30 min in a hot-plate. Influence of UV-induced production of gold nanoclusters on the oxide surface of SiNWs was demonstrated by both of the XPS analysis and electrical properties.

### 3.2.2 Relationship of DPN transport mechanisms

In the dip-pen nanolithography (DPN) procedure, water meniscus controls the effective tip-substrate contact regions, aqueous  $\text{HAuCl}_4$  molecules can be deposited on silicon oxide surfaces of SiNWs with precise control over pattern shape and feature size. Figure 3.2 shows the relationship of AFM-tip writing speed and relative humidity of environment for dip-pen nanolithography of aqueous  $\text{HAuCl}_4$  ink on the surface of silicon dioxide.

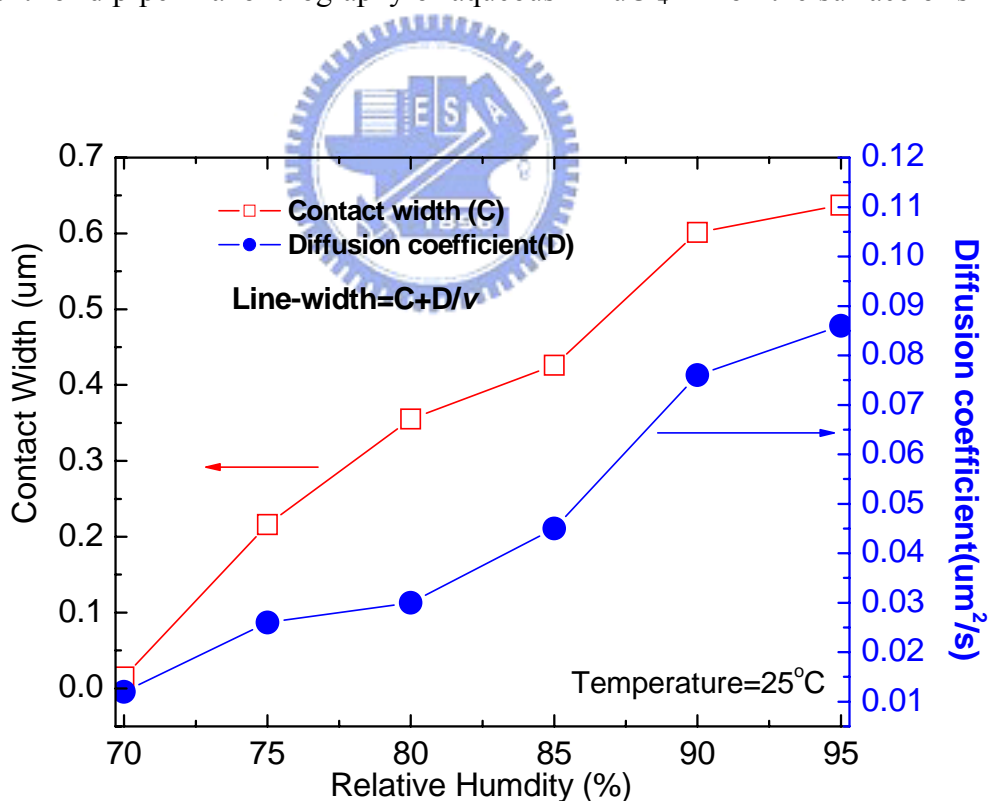


**Figure 3.2** Characteristic curves between speed of the dip-pen lithography and relative humidity of environment at room temperature ( $25\text{ }^\circ\text{C}$ ).

It was observed that line widths increased with longer tip-substrate contact times, and the resolution of the patterning is dependent upon writing speed ( $v$ ) and relative humidity. It was found that line widths depend on two coefficients, including: contact width  $I$  and diffusion coefficient ( $D$ ). Contact width term further is assumed that the finite size of the tip apex results in a minimum contact width and dependent upon relative humidity. Diffusion is the process by which ink molecules spread radially onto the substrate from the tip. Diffusion coefficient is assumed proportional to the dwell time and inversely to DPN tip drawing speed.

It means that we can place nano-scale patterns directly on oxidized silicon surface via proper control of parameters in DPN technique.  $\text{HAuCl}_4$  monolayer nano-patterns on the surface of silicon dioxide were imaged by lateral force microscopy (LFM) immediately after writing. For aqueous  $\text{HAuCl}_4$  inks, line-widths are essentially dependent of the DPN pen-tip writing speed and dwell time. Under various relative humidity conditions, the diffusion coefficient and contact width were estimated, which are very important for line-width control in the advanced applications.

### 3.2.3 X-ray photoelectron spectra of UV-induced reduction of gold nanoclusters



In order to determine the influence of the UV-light irradiation for aqueous  $\text{HAuCl}_4$  solution, a silicon substrate that was used to immersion the 7.5 mM  $\text{HAuCl}_4$  solution for 10 mins and dry with  $\text{N}_2$  gas. Finally, the sample substrate was then irradiated in the 365 nm UV light for 20mins. The x-ray photoelectron spectroscopy (XPS) analysis results as show in the Figure 3.3. After 365 nm UV light irradiation process, it was clearly observed that the  $\text{Au}4f_{7/2}$  and  $\text{Au}4f_{5/2}$  spin-orbit components peak signal implicated that the UV-induced reduction of the gold ions ( $\text{Au}^{3+}$ ) and aggregation of gold nanoclusters ( $\text{Au}^0$ ) and gold salt on the  $\text{SiO}_2$  surface of silicon.

In this 3.2.3 section, we report a successful strategy for using DPN to write molecule monolayer structures directly onto the surface of silicon dioxide of SiNWs, as shown in Figure 3.4 (a). Utilizing the 7.5 mM aqueous  $\text{HAuCl}_4$  solution as the “molecule ink” in a conventional DPN procedure, we can directly write nano-scaled molecule patterns onto oxidized silicon surface of SiNWs.

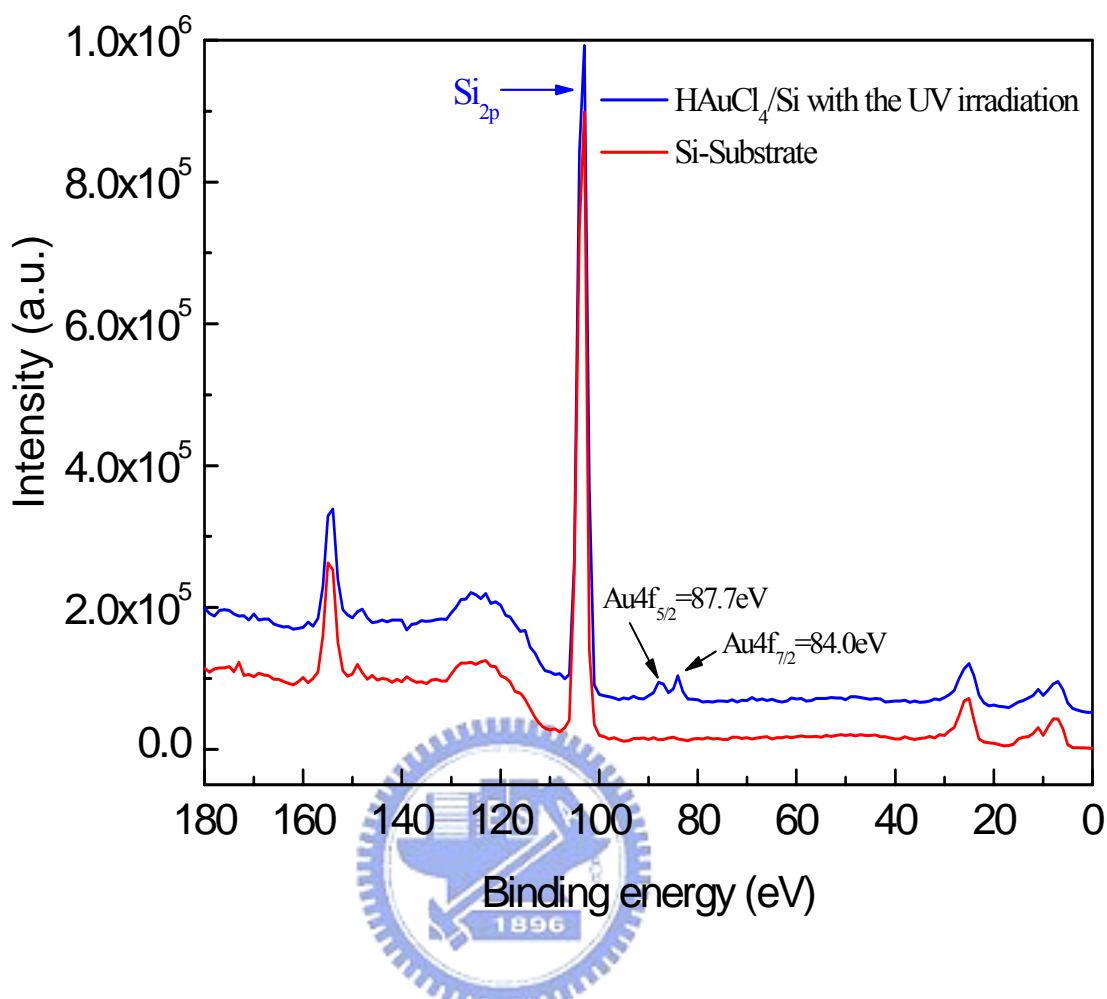


**Figure 3.3** X-ray photoelectron spectroscopy (XPS) analysis spectra of the 365 nm UV-light irradiation process on the SiO<sub>2</sub> surface of the silicon substrate.

The silicon nanowires (SiNWs) with 100 nm wide and 2 μm long on the n-type (100) SOI substrate were fabricated by the scanning probe microscope (SPM)-based anodic oxidation technique and TMAH anisotropic wet etching as shown in Figure 3.4 (b). Inset AFM images of Figure 3.4 (b) shows the details of silicon nanowire (SiNW) structure with a line-width about 100 nm.

The x-ray photoelectron spectroscopy (XPS) analysis, which was then used to evaluate the surface chemical composition before and after 365 nm UV light irradiation of gold salt on the surface of oxide / silicon as shown in the Figure 3.5.

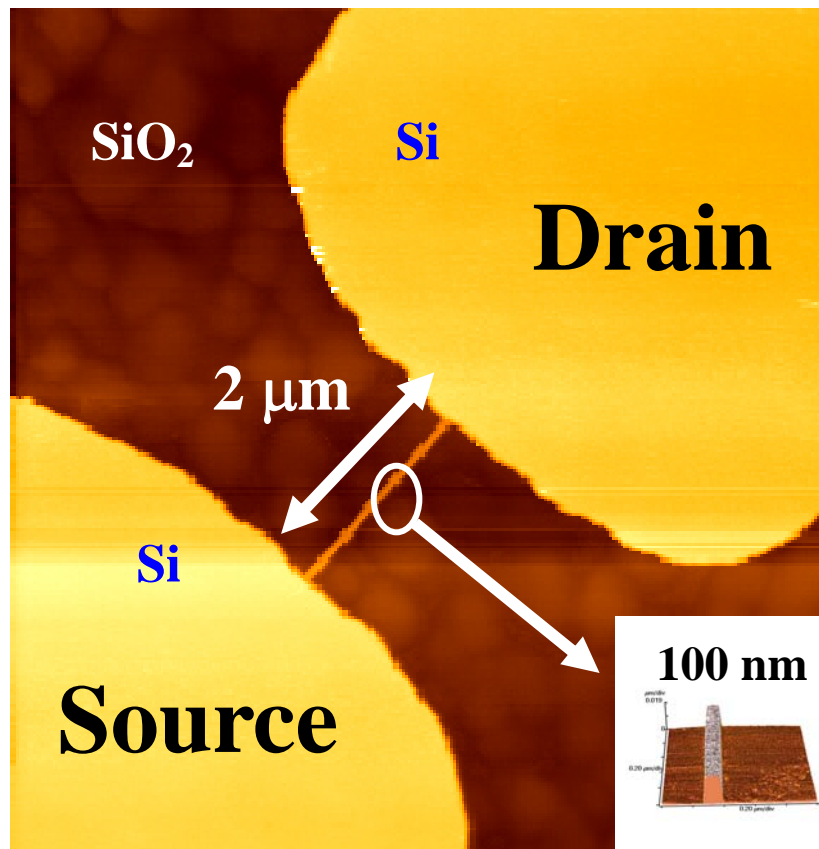
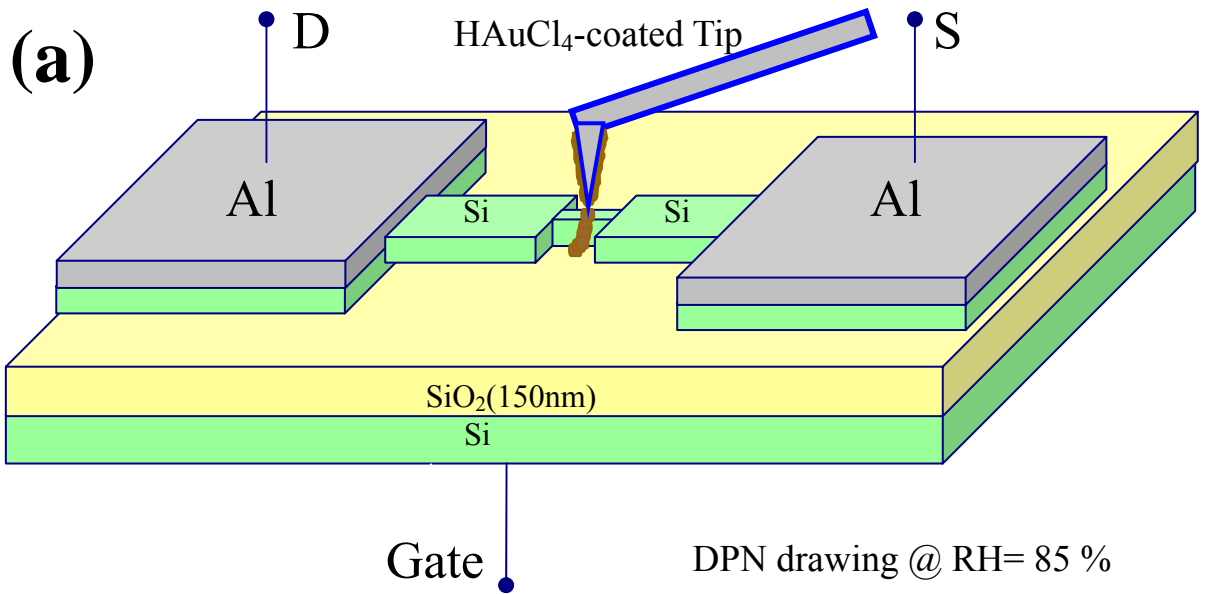


**Figure 3.4** (a) Schematic diagram of the Dip-Pen Nanolithography directly patterning. (b) AFM images of a silicon nanowire device on (100) SOI substrate fabricated by using scanning probe microscope (SPM) local oxidation method and TMAH wet etching. Nanowire is about 100 nm wide and 2 μm long.

UV-induced reduction of the gold ions ( $\text{Au}^{3+}$ ) and aggregation of gold nanoclusters ( $\text{Au}^0$ ) on the  $\text{SiO}_2/\text{Si}$  surface were found. It was observed that UV irradiation resulted in decrease in the binding energy and the changes in the width of the  $\text{Au}4f$  peak corresponding to  $\text{Au}^0$  and the growth of gold nano-clusters can be evidenced. The similar result was reported by Dr. Ferdi Karadas et al. [23].

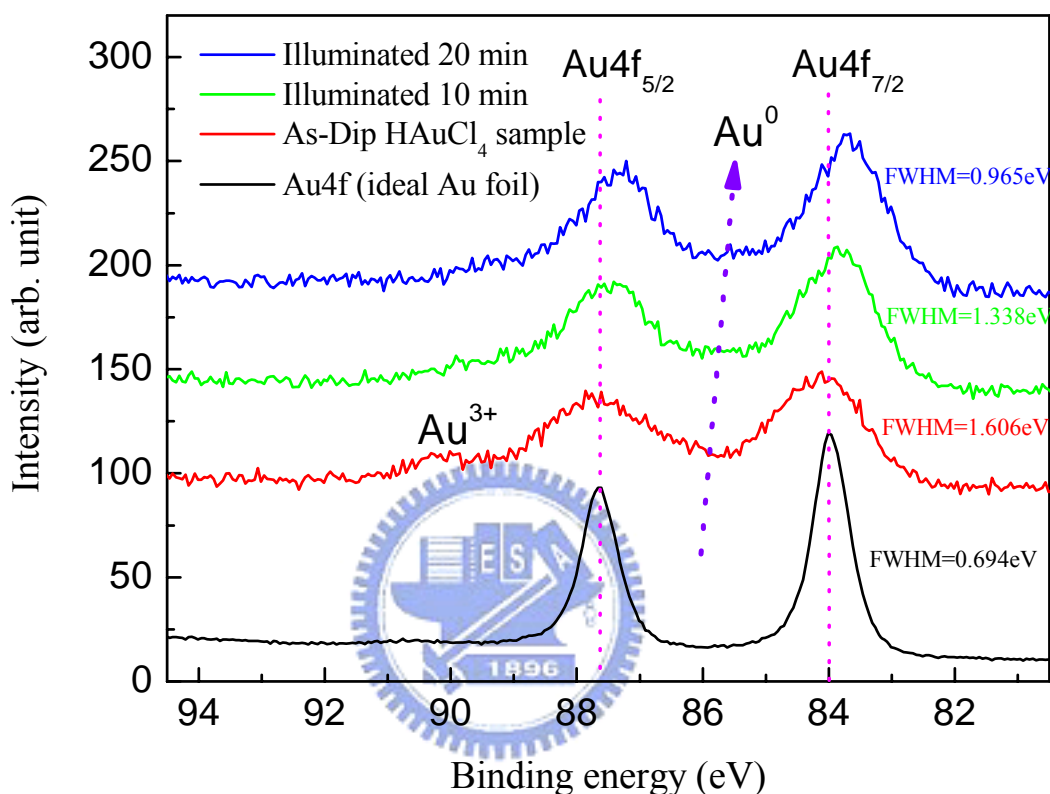


**Figure 3.5** XPS spectra of the  $\text{AuCl}_4^- / \text{native oxide} / \text{Si}$  system as function of UV exposure time. It was found that UV irradiation induced production of gold nanoclusters on the surface of a silicon dioxide sample.

AFM images were recorded at a scan rate of 1 Hz.  $\text{HAuCl}_4$  molecule ink was then selectively provided by DPN on the native oxide surface of silicon nanowires (SiNWs) as shown in Figure 3.6 (a) and Figure 3.6 (b). Owing to the thickness of the  $\text{HAuCl}_4$  molecule monolayer patterns is too thin to identify by AFM analysis. Therefore, we utilized the lateral force microscopy (LFM) to identify and analysis the molecule monolayer patterns on the silicon dioxide of SiNWs. LFM images of the silicon nanowire after DPN of  $\text{HAuCl}_4$  inking in area of  $0.5 \mu\text{m}$  by  $2.0 \mu\text{m}$  across the SiNWs at speed of 50 nm/s and RH of 85 % as shown in Figure 3.6 (b).



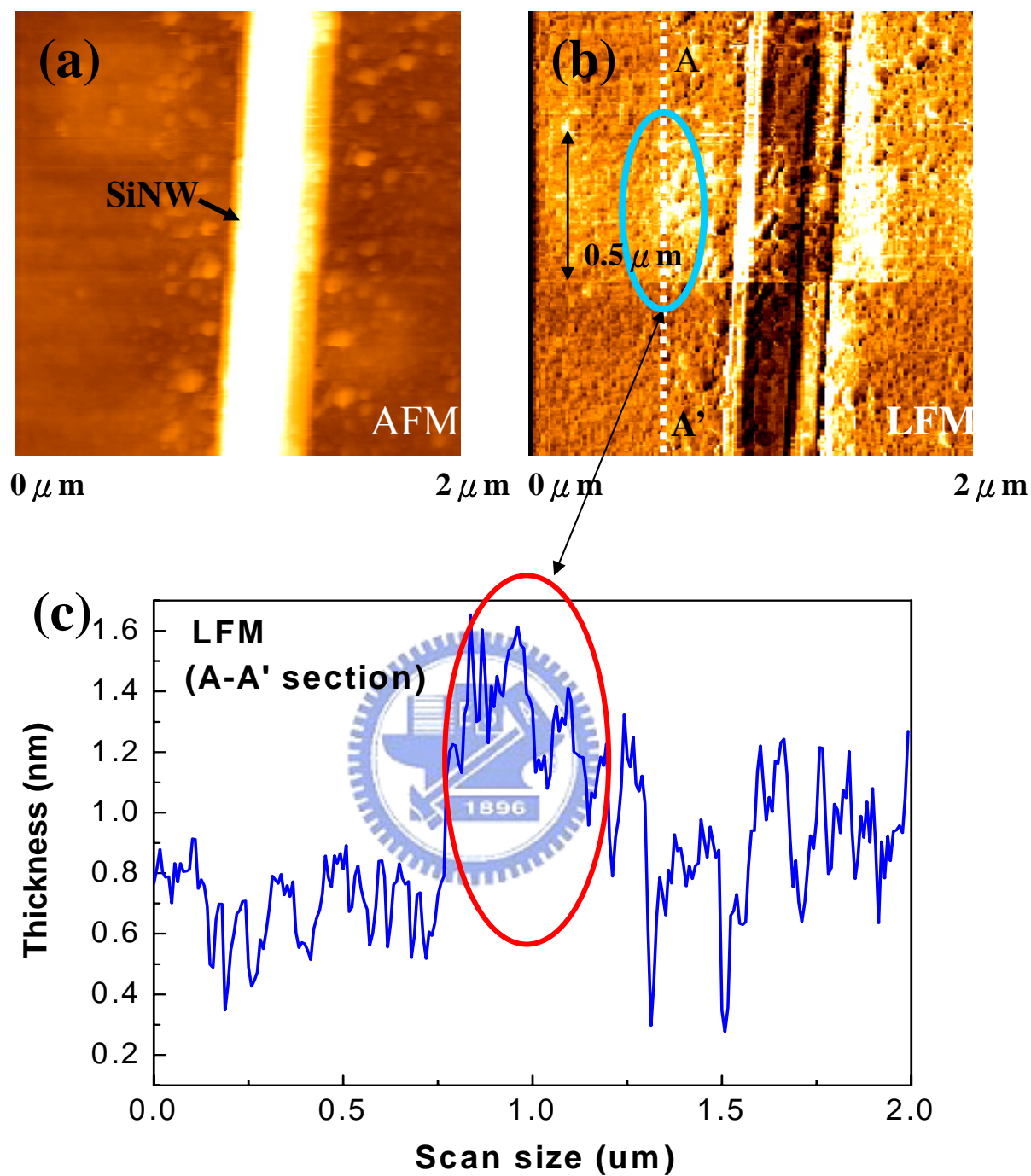


**Figure 3.6** (a) AFM images of a silicon nanowire. (b) LFM image of a silicon nanowire after DPN of HAuCl<sub>4</sub> ink in area of 0.5 by 2 μm across the SiNW at speed of 50 nm/sec and RH of 85 %. (c) Depth profile of A-A' section of a LFM image. A 2-μm LFM profile parallel to the SiNW and the thickness of gold nanoclusters is the less than 1 nm in thickness.

LFM images were recorded at a scan rate of 3 Hz. From Figure 3.6 (c) results, it was observed that the thickness of the gold nanoclusters, estimated less than 1nm, was by lateral force microscopy (LFM) measurement. The corresponding major oxidation product is determined as chlorine gas, which is initially adsorbed onto the surface, but eventually diffuses out into the vacuum on electrical property measurement system.

### 3.2.4 Electrical Characteristics of Influence of UV-induced Reduction of Gold Nanoclusters

Figure 3.7 (a) shows the  $I_{ds}-V_{ds}$  characteristics of SiNWs when  $V_{ds}$  was swept from -1.0 V to +1.0 V and the bias of the control bottom gate is +5 V. It was demonstrated that the conductance of SiNW increased two times at 0.5 volts of  $V_{ds}$  after DPN of gold nanoclusters. I suggested that the UV-induced production of gold nanoclusters on the oxide surface of SiNWs could be induced electrons into n-type silicon nanowires (SiNWs), the top-side surface of SiNWs will be in electrons accumulation such that the conductivity of the SiNWs increased. From the Figure 3.7 (b), electrical characteristic curve ( $I_d$ - $V_g$ ) shown that the change in threshold voltage ( $\Delta V_T$ ) is about 0.3 V. It was shown that the gold ions ( $Au^{3+}$ ) and gold nanoclusters ( $Au^0$ ) on the silicon nanowire surface can enhance carriers transfer in the n-type silicon nanowire channel. DPN of gold nanoclusters on the oxide surface of silicon nanowires enhanced carriers transport in the channel of n-type silicon nanowires (SiNWs).

We have successfully demonstrated that using dip-pen lithography to deposit 1nm gold salt from an aqueous  $HAuCl_4$  ink solution onto a  $SiO_2$  / silicon nanowires (SiNWs) induces reduction of the gold ions ( $Au^{3+}$ ) aggregated to gold nanoclusters by using the 365 nm UV light irradiation in air evidenced and subsequent nucleation to gold nano-clusters by XPS analysis. It was observed that the decrease in the binding energy. And, the changes in the width of the Au4f peak corresponding to  $Au^0$  and the growth of gold nanoclusters can be evidenced. Electrical characteristics demonstrated that the conductance of SiNWs increased two times at 0.5 volts of  $V_{ds}$  after DPN of gold nanoclusters. DPN of gold nanoclusters on the oxide surface of silicon nanowires enhanced carriers transport in the channel of n-type silicon nanowires. Because of the gold nano-clusters could be used for variety bio-medical applications, it is believed that the proposed nanofabrication technique can be further applied in both nano-electronics and nano-biochemical sensors applications.

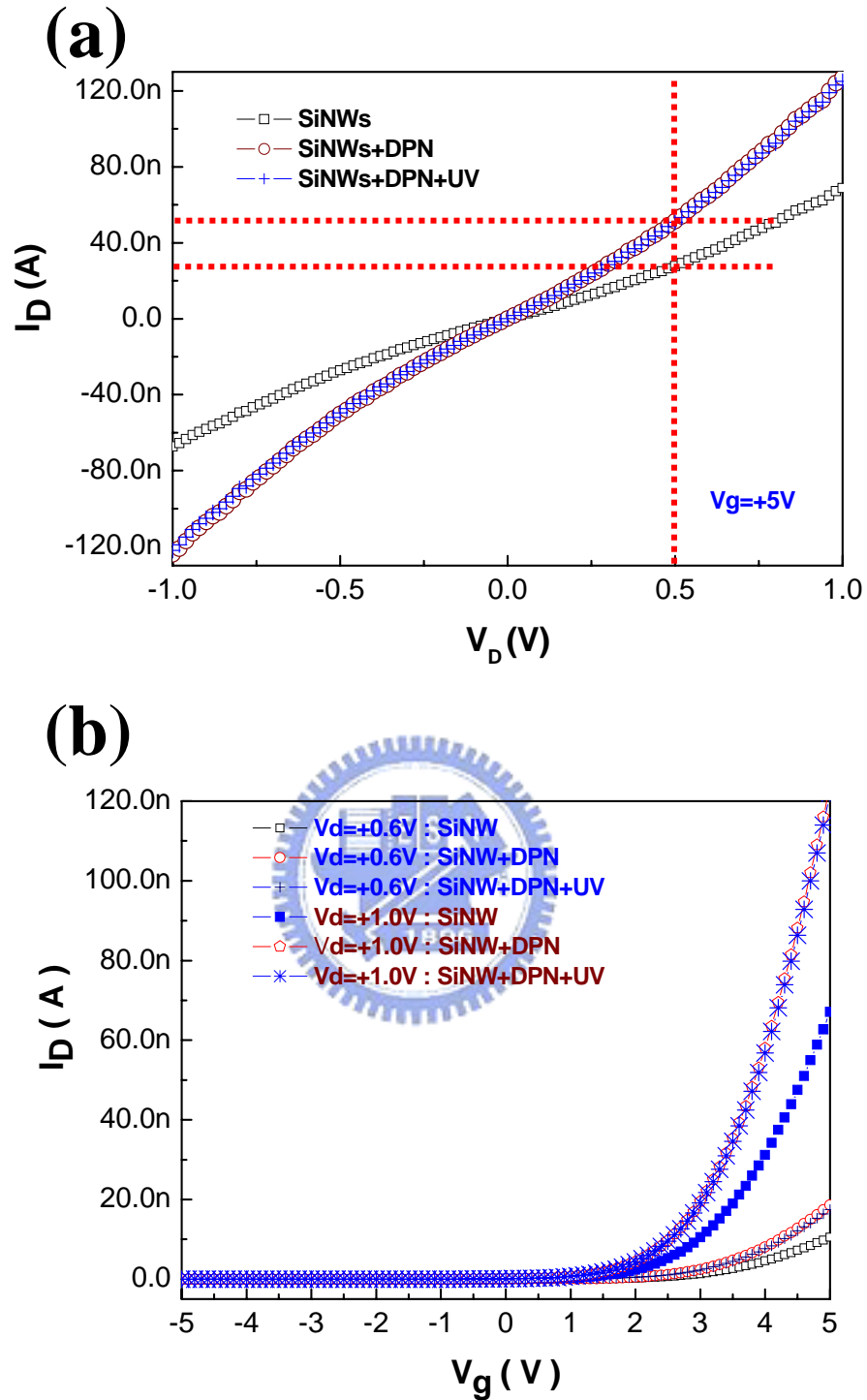


**Figure 3.7** (a) Electrical properties ( $I$ - $V_{ds}$ ) of three different samples (Si-NWs, Si-NWs + DPN  $\text{HAuCl}_4$ , Si-NWs + DPN  $\text{HAuCl}_4$  + UV irradiation) at 300 K with sweep of source-drain bias  $V_{ds}$  (-1.0 V and 1.0 V) at  $V_g = 5$  V. (b)  $I_d$ - $V_g$  characteristics of SiNWs measured at 300 K with different source drain bias  $V_{ds}$  (0.6 V and 1.0 V).

### 3.3 Selective deposition of gold particles on dip-pen nanolithography patterns on silicon dioxide surfaces

In this 3.3 section, we report a novel platform to perform selective deposition of gold nanoparticles on dip-pen nanolithographic patterns on SiO<sub>2</sub> surfaces. An “inked” atomic force microscope (AFM) tip was adopted to deposit 2.2 mM organic *N*-(2-aminoethyl)-3-aminopropyltrimethoxysilane (AEAPTMS) molecules in nanopatterns through a water meniscus onto a SiO<sub>2</sub> substrate under ambient conditions; the molecules act as linkers for the selective deposition of gold nanoparticles on the SiO<sub>2</sub> surface. Conditions for dip-pen nanolithography of organic nanopatterns of AEAPTMS were investigated. In addition, gold nano-particles with negatively-charged citrate surfaces were deposited selectively on top of the organic patterns. X-ray photoelectron spectroscopy was then used to evaluate the presence of gold nanoparticles on the SiO<sub>2</sub> surface. Lateral force microscopy was utilized to differentiate the surface between oxidized semiconductors and patterned areas with monolayer of AEAPTMS.

In this study, we successfully demonstrated the combination of DPN and self-assembly techniques to realize selective deposition of gold nanoparticles on silicon oxide surfaces. We report a successful strategy for using DPN to write molecular nano-structures directly onto silicon oxide surfaces. Figure 3.8 (a) shows the DPN writing mechanism for an AEAPTMS monolayer on the oxidized surface of a silicon substrate. Nanopatterns with feature sizes down to 60 nm on the oxidized silicon surface can be easily generated. Furthermore, citrate-coated gold nanoparticles were deposited selectively onto the AEAPTMS-patterned area via Coulombic force between AEAPTMS and the gold nanoparticles, as shown in Figure 3.8 (b). It is believed that the proposed nanofabrication technique, combining DPN with the self assembled monolayer (SAMs) process, can be further applied in both nano-electronics and nano-biochemical sensors.

#### 3.3.1 Generate the molecular monolayer by DPN technique

In the experiments, (100)-silicon wafers were cleaned by standard RCA cleaning processes to remove surface organic contamination. The hydroxyl-terminal surface of the oxidized silicon substrate was prepared by immersing the silicon sample into a piranha solution [1:3 (v/v) mixture of H<sub>2</sub>O<sub>2</sub> and H<sub>2</sub>SO<sub>4</sub>] for 10 min at 120 °C, rinsed copiously with de-ionized (DI) water (>18.5 MΩ/cm), and blown dry with nitrogen (N<sub>2</sub>) gas. The

surface roughness ( $R_q$ ) of the  $\text{OH}^-$ -passivated films was around 0.874 nm measured by AFM. Then, AEAPTMS ink-coated tips were prepared by immersing a commercial PtIr tip (tip diameter = 10 nm) into a 2.2 mM AEAPTMS solution for 30 sec. Experiments were carried out under ambient conditions (DPN-tip drawing speed = 0.1 ~ 0.6  $\mu\text{m}/\text{sec}$ , set point (tip / sample force) = 1.0 V,  $25 \pm 0.5$   $^\circ\text{C}$ ,  $65 \pm 1$  % relative humidity) using an atomic force microscope.

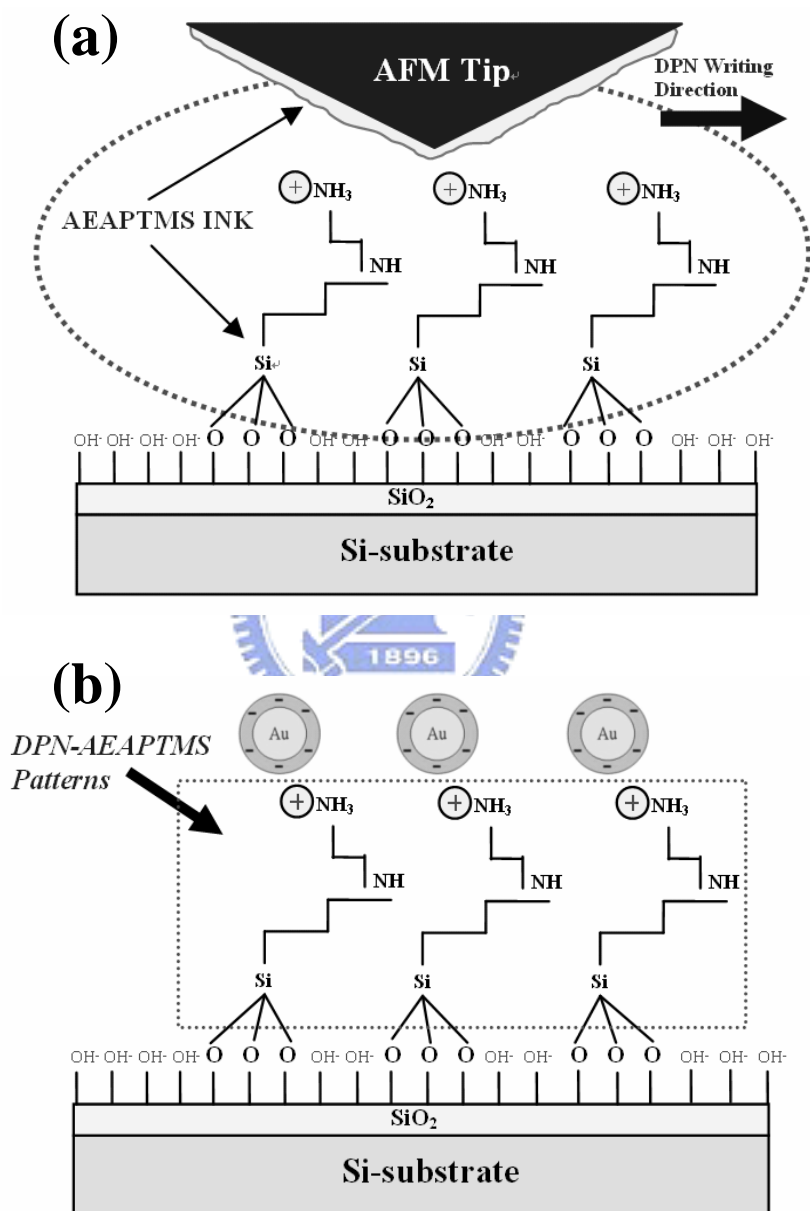


**Figure 3.8** (a) The mechanism of deposition of a monolayer of AEAPTMS molecules on the hydroxyl-terminal surface of an oxidized silicon substrate. (b) Citrate-coated gold nanoparticles were deposited selectively onto the AEAPTMS nanopattern via Coulombic force.

Several key experimental parameters affect feature resolution, including humidity, temperature, tip / sample force, and the DPN-tip drawing speed. During contact-mode DPN operation under ambient conditions, a water meniscus forms naturally between the AEAPTMS ink-coated tip and the sample surface. The DPN AFM-tip delivered AEAPTMS molecules directly onto the substrate by capillary transport through the water meniscus. Because humidity plays a key role in controlling the diameter of the water meniscus between the DPN AFM-tip and the sample surface, the linewidth of the pattern drawn by DPN increases as humidity increases. The “set point” is the parameter that sets the force acting between the specimen and the tip of the cantilever and controls the distance between the tip and the sample surface. DPN in the contact mode generally functioned in the domain of a small repulsive force to minimize specimen damage. The feature size of the DPN pattern increased as the set point (i.e. tip / sample force) increased. Moreover, for AEAPTMS ink, line widths of DPN patterns were also essentially dependent on the DPN AFM-tip drawing speed.

### **3.3.2 Colloidal gold nanoparticles synthesis and anchored onto the amino-terminal surface with the self-assembly method (SAMs)**

SAM formation provides one easy route towards surface functionalization by organic molecules containing suitable functional groups like, -SH, -COOH, -NH<sub>2</sub> and silanes, on selected metallic as well as semiconducting surfaces. We employed the SAMs technique to perform selective deposition of gold nanoparticles. The synthesis of the gold nanoparticles method was based on Frens’s synthesis method [24]. The diameter from 5 nm to 15 nm of gold nanoparticles is controllable with this method. A solution of 100 ml of 2.2 mM tri-sodium citrate (C<sub>6</sub>H<sub>8</sub>O<sub>7</sub>Na<sub>3</sub>·2H<sub>2</sub>O) as a reductant was heated to boiling, and afterwards 40 ml of 0.815 mM hydrogen-tetrachlorauric acid (HAuCl<sub>4</sub>·4H<sub>2</sub>O) was added with rapidly mixing. The solution was then heated to boiling for 15 min. The solution initially developed a pale yellow color and then a gray color, which changed to lavender and then transformed into red in 1 ~ 3 min. Gold nano particles with a diameter of 15 nm were obtained as shown in the Figure 3.9 (a), shows a wide view TEM image of a sample of approximately 15 nm gold nanoparticles [25]. After the aqueous amino silane modification of the silicon dioxide surface substrate, the amino-terminal silicon substrate was then immersed in the colloidal gold nanoparticles solution for 1.5 h.

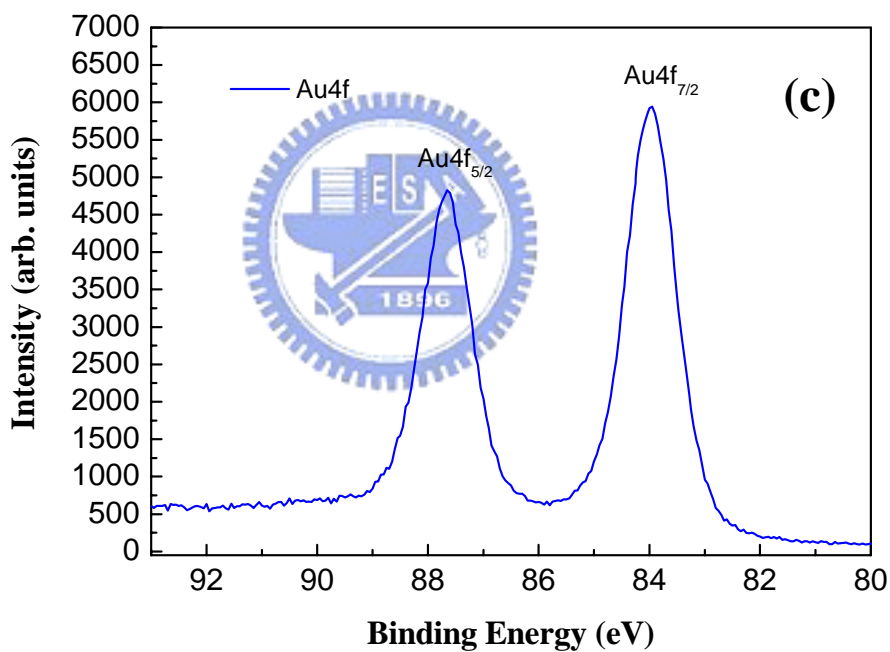
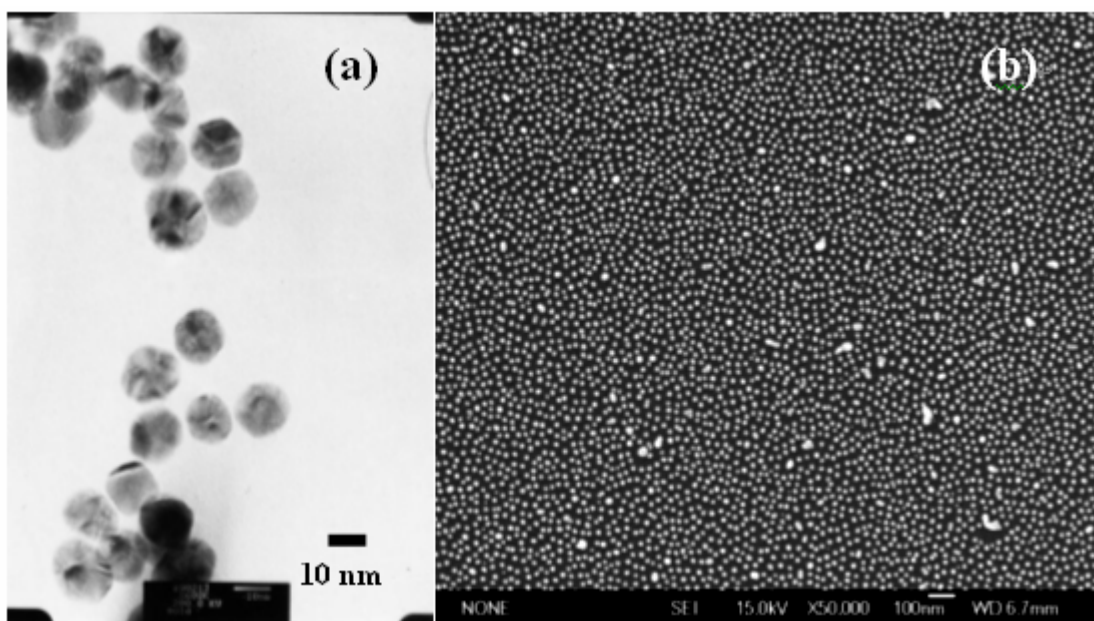


**Figure 3.9** (a) High resolution TEM images of 15 nm gold nanoparticles. (b) SEM images of AuNPs self-assembled on the AEAPTMS-functionalized SiO<sub>2</sub> surface. (c) X-ray photoelectron spectra of AuNPs anchored on the AEAPTMS-functionalized SiO<sub>2</sub> surface.

The silicon dioxide substrate was rinsed with distilled water plentifully and dried with N<sub>2</sub> gas afterwards. Owing to the coulomb interaction between amino groups and the repulsive of the negatively charged surfaces of gold nanoparticles resulted in the gold

nanoparticles being distributed homogeneously on the surface of silicon dioxide as shown in Figure 3.9 (b). Figure 3.9 (c) shows that the Au 4f core-level spectra, which has been resolved into the Au4f<sub>7/2</sub> and Au4f<sub>5/2</sub> spin-orbit components and the binding energy of the Au4f<sub>7/2</sub> component was measured to be 84 eV and is characteristic of metallic gold.

After DPN writing procedure, amino-functional silane nanopatterns formed on the hydroxyl-terminal surface, which provided a surface bearing free amine (-NH<sub>3</sub>) group, was dried with nitrogen and baked at 120 °C for 30 min on a hot-plate. Then, the silane-modification sample was immersed in a solution of 15 nm citrate-coated gold nano-particles for 1 h. Then the sample was rinsed with DI water and dried with N<sub>2</sub> gas. This procedure led to the selective deposition of gold nanoparticles on the AEAPTMS-patterned region via interaction of the static charge between AEAPTMS-patterned regions and gold nanoparticles. X-ray photoelectron spectroscopy (XPS) was used to evaluate the surface chemical composition of patterns with and without gold nanoparticles selectively deposited onto the SiO<sub>2</sub> surface. Lateral force microscopy (LFM) was used to differentiate areas on the surface as oxidized semiconductor regions and DPN nanopatterns. Gold nanoparticles repelled each other due to the presence of negative citrate ions on the hydroxyl-terminated surface; the particles were imaged by AC-mode atomic force microscopy.

### 3.3.3 Linear control patterning of the DPN lithography

In DPN for AEAPTMS nanopatterning, the size of the water meniscus controls the effective tip-substrate contact regions. AEAPTMS molecules were deposited on hydroxyl-terminated surfaces with precise control of pattern shape and feature size.

It was found that the linewidth of DPN patterns increased with longer tip-substrate contact times, and the resolution of the patterning is depended upon writing speed ( $v$ ) and relative humidity. Three key experimental factors affect diffusion coefficient ( $D$ ), including humidity, the DPN-tip drawing speed, and the chemical affinity between the AEAPTMS ink and the substrate surface. In the linear diffusion model of liquid solutions, line widths of DPN-patterns are assumed proportional to the inverse of the writing speed (i.e., dwell time). That is, line width =  $D / v$ , and the plot of the line width as a function of the inverse of tip scanning speed is linear and goes through the origin. Furthermore, the diffusion



coefficient in this model is the slope of the curve. However, in the curve for the DPN of AEAPTMS, the plot of the line width as a function of the inverse writing speed is linear but intercepts the y-axis at positive offset, the value of which depends upon environment humidity. Consequently, the linear diffusion model for DPN was modified to a linear diffusion with offset. This offset value is assumed as the finite size of the area of the tip peak interaction with the sample surface and represents the minimum contact width of the

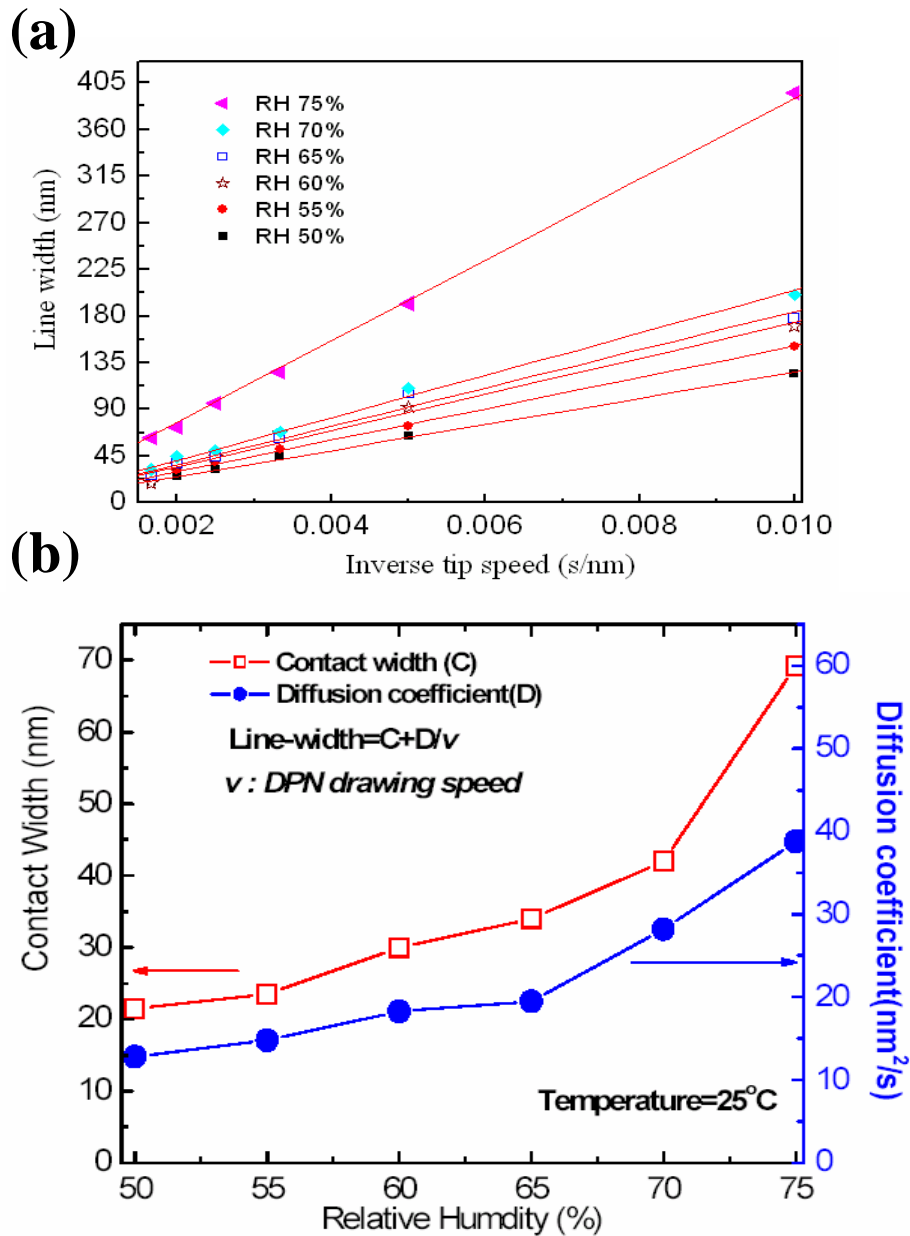


**Figure 3.10** Characteristic curves from dip-pen lithography for the AEAPTMS ink. (a) Relationship of DPN linewidth with respect to tip writing speed under different relative humidities. (b) Relationship of the contact width and diffusion coefficient estimated from Figure 3.10 (a) under different relative humidities.

tip when the drawing speed of DPN is extremely large. This also means that the smallest linewidth that can be achieved is the contact width once the relative humidity is determined. Figure 3.10 (a) shows the relationship of DPN linewidth of AEAPTMS with respect to the inverse of writing speed for different relative humidities. For different humidities, the contact widths are all different because the diameter of the water meniscus formed between the tip and the sample is related to the relative humidity. The contact widths and diffusion coefficients under different relative humidity are obtained from the intercepts of the slopes of the lines in the y-axis in Figure 3.10 (a). Figure 3.10 (b) shows the relationship of contact width and diffusion coefficient with respect to relative humidity of DPN of aqueous AEAPTMS molecular ink onto the hydroxyl-terminal surface of an oxidized silicon substrate. AEAPTMS nanopatterns on hydroxyl-terminal surfaces were imaged by lateral force microscopy (LFM) immediately after DPN.

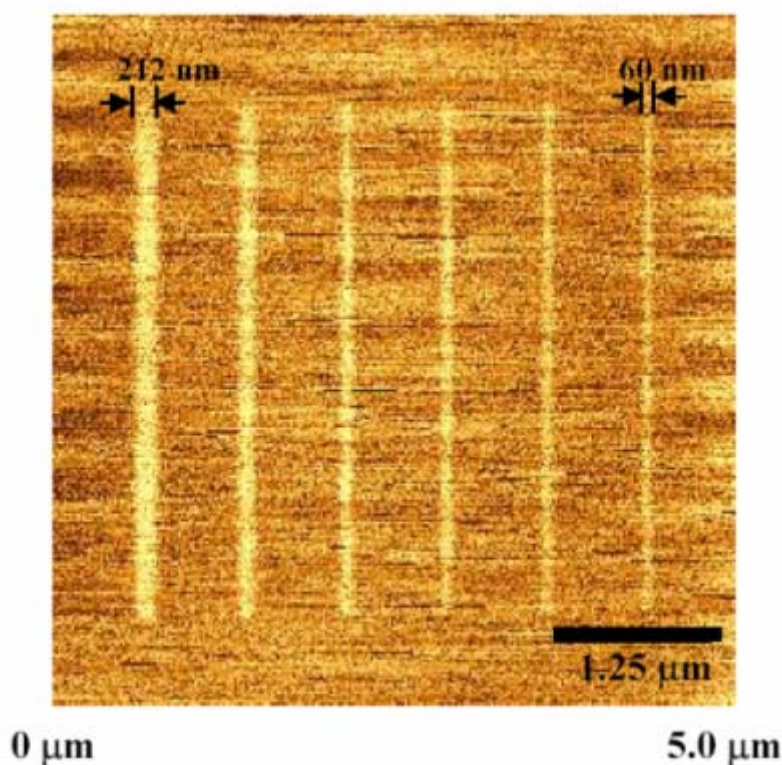


**Figure 3.11** LFM images of DPN-generated AEAPTMS monolayer patterns on silicon oxide surfaces. LFM images were recorded at a scan rate of 6 Hz. Parallel line AEAPTMS patterns on an oxidized silicon surface were generated at writing speeds of 0.1, 0.2, 0.3, 0.4, 0.5 and 0.6  $\mu\text{m}/\text{sec}$ . The linewidth of 60 nm has been successfully drawn via DPN technique at a speed of 0.6  $\mu\text{m}/\text{sec}$ .

Figure 3.11 shows the lateral force microscope images of DPN-generated AEAPTMS monolayer grid line patterns (bright contrast) on SiO<sub>2</sub> surfaces. LFM images were recorded at a scan rate of 6 Hz. Grid line patterns on the SiO<sub>2</sub> surface were obtained by DPN at a writing speed from 0.1 to 0.6 μm/sec. The linewidths corresponding to the writing speeds are 212, 140, 96, 78, 72, and 60 nm, respectively. The nanopattern of AEAPTMS modified by silanation 4 μm long and 60 nm wide has been successfully deposited as a monolayer line on SiO<sub>2</sub> surfaces via DPN at 65 % relative humidity. Smaller linewidths of AEAPTMS can be expected when a higher writing speed for DPN or a lower humidity is used.

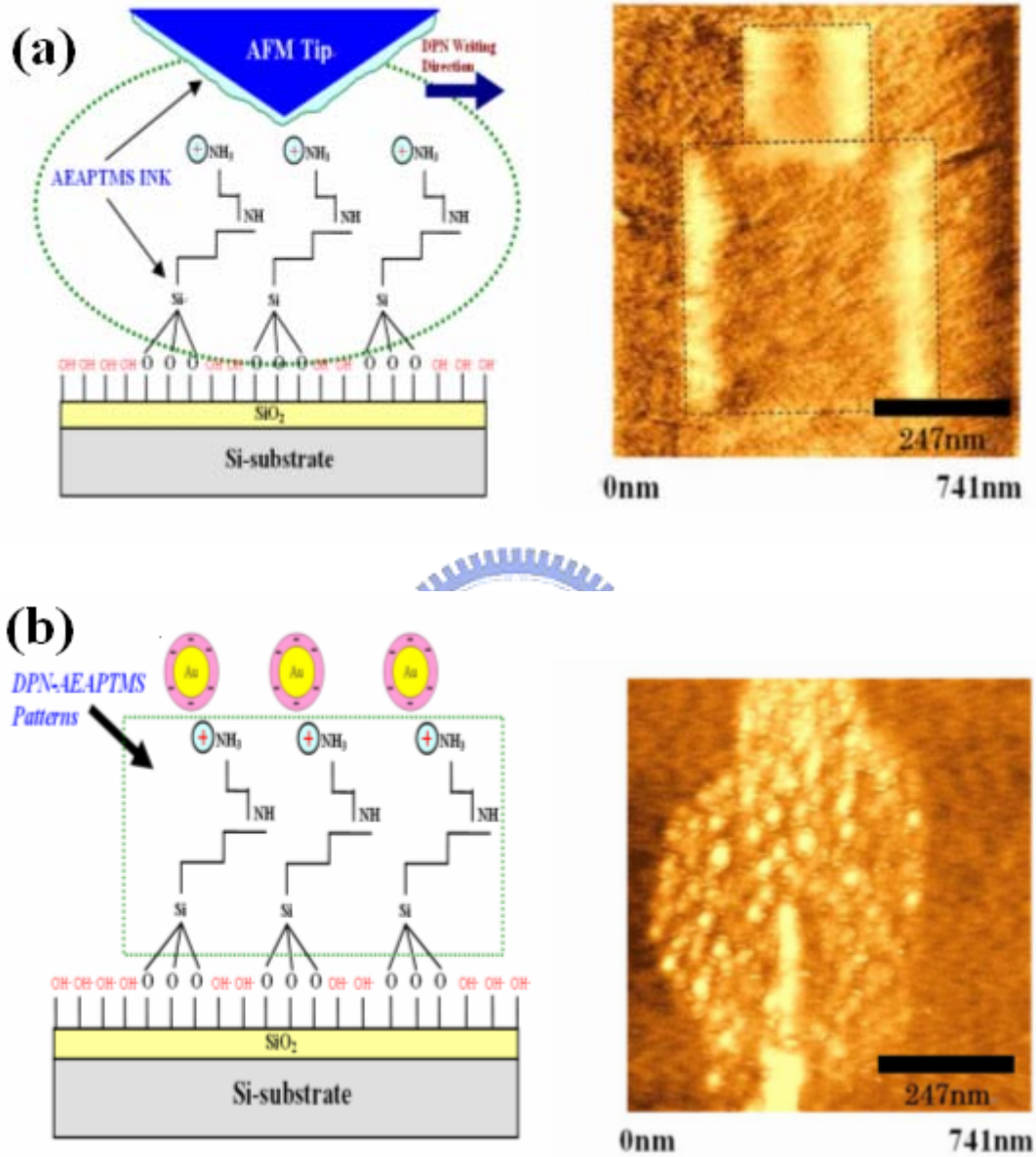
### 3.4 Gold nanoparticles selective anchored on DPN AEAPTMS regions

Figure 3.12 (a) shows an LFM image of DPN-generated AEAPTMS monolayer double square patterns (741 × 741 nm<sup>2</sup>) on SiO<sub>2</sub> surface with a writing speed of 741 nm/sec (1Hz scan). The regions of brighter contrast regions correspond to the deposited AEAPTMS patterns modified by silanation and darker regions are due to the hydrophilic (-OH group-rich) SiO<sub>2</sub> surface. As the sample after silanation by AEAPTMS solution, was immersed in the colloidal gold solution, the NH<sub>2</sub> groups become protonated, forming NH<sup>3+</sup>, and bind to the negatively charged citrate-passivated gold nanoparticles.

The amino groups on the AEAPTMS molecules immobilized the gold nanoparticles on the SiO<sub>2</sub> substrate because of the specific affinity of the amino group to the negative citrate ions on the surface of the gold nanoparticles as shown in Figure 3.12 (b) by AC-mode AFM. The patterns of gold nanoparticles, however, were not in accordance with the original AEAPTMS patterns. We believe this resulted from the lateral diffusion of AEAPTMS patterns during the selective deposition process of the 15 nm gold particles. We have successfully demonstrated the combination of DPN writing of AEAPTMS nanopatterns onto SiO<sub>2</sub> surfaces and self-assembly techniques for realizing localized deposition of gold nanoparticles onto amino-silanate-modified patterns on the SiO<sub>2</sub> surface.

To exam the selectivity of gold nanoparticles for the DPN AEAPTMS patterns on the SiO<sub>2</sub> surface, XPS analysis was applied to characterize square patterns modified by silanation (1 × 1 μm<sup>2</sup>) on the SiO<sub>2</sub> surface after the self-assembly of the gold nanoparticles.

The modification sample was immersed in a solution of 15 nm citrate-coated gold nanoparticles for 1 h. Then the sample was rinsed with DI water and dried with N<sub>2</sub> gas.



**Figure 3.12** (a) LFM images of DPN AEAPTMS monolayer patterns on SiO<sub>2</sub> surfaces. Dotted lines show the designed patterned area. (b) AC-mode AFM topographic image of gold nano-particles after selective deposition on the square patterns modified by silanation by DPN after immersion in the gold nano-particle solution for 1 h.

Figure 3.13 shows the XPS analysis of the area with the DPN AEAPTMS patterns on the SiO<sub>2</sub> surface and of the area outside the DPN AEAPTMS patterns. The Au 4f peaks corresponding to the gold nanoparticles (Au<sup>0</sup>) on the AEAPTMS silanation patterns on the SiO<sub>2</sub> surface are clearly seen. Outside the DPN-AEAPTMS patterns, no Au 4f signal is observed, showing that gold nanoparticles deposited only on the AEAPTMS patterns.

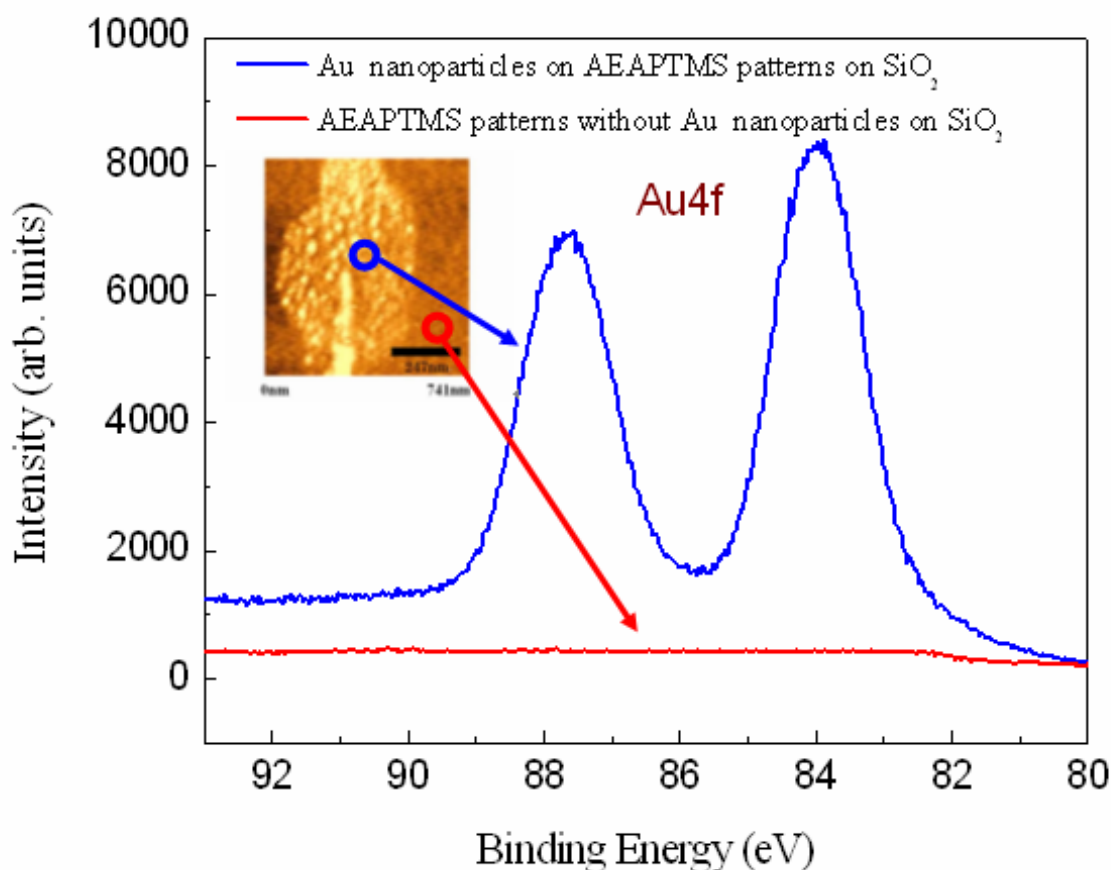


**Figure 3.13** Spectra from x-ray photoelectron spectroscopy of the areas of DPN AEAPTMS patterns and outside the DPN AEAPTMS patterns to evaluate the selectivity of gold nanoparticles for the AEAPTMS patterns and for the SiO<sub>2</sub> surface. No Au4f signal was observed outside the DPN AEAPTMS patterned area.

### 3.5 Conclusions

DPN of AEAPTMS nanopatterns has been demonstrated on the SiO<sub>2</sub> surface. Linewidths down to 60 nm have been successfully produced, and smaller patterns are expected when writing is done at lower humidity or higher speed. We also have successfully deposited gold nanoparticles onto AEAPTMS nanopatterns modified by silanation on a hydroxyl-terminal SiO<sub>2</sub> surface. The reducing the time of self-assembly in gold selective deposition may be necessary to reduce the distortion of AEAPTMS patterns and gold nanoparticles patterns. Because of their nature, gold nano-particles have been widely used for a variety of bio-medical applications. The proposed nanofabrication technique may be further applied in both nanoelectronics and nanobiochemical applications.



## Reference

- [1] R. D. Piner, J. Zhu, F. Xu, S. Hong, C. A. Mirkin, ““Dip-Pen” Nanolithography”, *Science*, **283**, pp. 661-663, 1999.
- [2] M. Albrecht, C. T. Rettner, A. Moser, M. E. Best and B. D. Terris, “Recording performance of high-density patterned perpendicular magnetic media” *Appl. Phys. Lett.* **81**(27), pp. 2875-2877, 2002.
- [3] J. T. Sheu, K. S. You, C. H. Wu, and K. M. Chang, “Single-electron transistor structures based on silicon-on-insulator silicon nanowire fabrication by scanning probe lithography and wet etching” *J. Vac. Sci. Technol. B* **20**(6), pp. 2824-2828, 2002.
- [4] Y. Xia, J. A. Rogers, K. E. Paul, and G. M. Whitesides, “Unconventional methods for fabricating and patterning nanostructures,” *Chem. Rev.* **99**, pp. 1823-1848, 1999.
- [5] M. T. Li, L. Chen, S. Y. Chou, “Direct three-dimensional patterning using nanoimprint lithography”, *Appl. Phys. Lett.* **78**(21), pp. 3322- 3324, 2001.
- [6] Benjamin M. Maynor, Yan Li, and Jie Liu, “Au “Ink” for AFM “Dip- Pen” Nanolithography”, *Langmuir* **17**, pp. 2575-2578, 2001.
- [7] Albena Ivanisevic and Chad A. Mirkin, ““Dip-Pen”Nanolithography on Semiconductor Surfaces”, *J. Am. Chem. Soc.* **123**, pp. 7887-7889, 2001.
- [8] Hun Zhang, Ki-Bum Lee, Zhi Li and Chad A Mirkin, “Biofunctionalized nanoarrays of inorganic structures prepared by dip-pen nanolithography”, *Nanotechnology* **14**, pp. 1113-1117, 2003.
- [9] Hyungil Jung, Rajan Kulkarni, and C. Patrick Collier, “Dip-Pen Nanolithography of Reactive Alkoxysilanes on Glass”, *J. Am. Chem. Soc.* **125**, pp. 12096-12097, 2003.
- [10] Ki-Bum Lee, Jung-Hyurk Lim, and Chad A. Mirkin, “Protein Nanostructures Formed via Direct-Write Dip-Pen Nanolithography”, *J. Am. Chem. Soc.* **125**, pp. 5588-5589, 2003.
- [11] P. John Thomas, G. U. Kulkarni and C. N. R. Rao, “Dip-pen lithography using aqueous metal nanocrystal dispersions”, *J. Mater. Chem.* **14**, pp. 625-628, 2004.
- [12] S. -J. Park, T. A. Taton, C. A. Mirkin, “Array-Based Electrical Detection of DNA with Nanoparticle Probes”, *Science*, **295**(5559), pp. 1503-1506, 2002.

- [13] Y. Cui, M. T. Björk, J. A. Liddle, C. Sönnichsen, B. Boussert, and A. P. Alivisatos, "Integration of Colloidal Nanocrystals into Lithographically Patterned Devices", *Nano Lett.* **4**(6), pp. 1093-1098, 2004.
- [14] Y. Lu, Y. Yin, Z. -Y. Li, and Y. Xia, "Synthesis and Self-Assembly of Au @ SiO<sub>2</sub> Core-Shell Colloids", *Nano Lett.* **2**(7), pp. 785-788, 2002.
- [15] R. Jin, Y. Cao, C. A. Mirkin, K. L. Kelly, G. C. Schatz and J. G. Zheng, "Photoinduced Conversion of Silver Nanospheres to Nanoprisms", *Science* **294**, pp. 1901-1903, 2001.
- [16] W. Lee, A. Chan, M. A. Bevan, J. A. Lewis, and P. V. Braun, "Nanoparticle-Mediated Epitaxial Assembly of Colloidal Crystals on Patterned Substrates", *Langmuir* **20**, pp. 5262-5270, 2004.
- [17] R. Elghanian, J. J. Storhoff, R. C. Mucic, R. L. Letsinger and C. A. Mirkin, "Selective Colorimetric Detection of Polynucleotides Based on the Distance-Dependent Optical Properties of Gold Nanoparticles", *Science* **277**, pp. 1078-1081, 1997.
- [18] T. A. Taton, C. A. Mirkin and R. L. Letsinger, "Scanometric DNA Array Detection with Nanoparticle Probes", *Science* **289**, pp. 1757- 1760, 2000.
- [19] Y. Xiao, F. Patolsky, E. Katz, J. F. Hainfeld, I. Willner, "Plugging into Enzymes": Nanowiring of Redox Enzymes by a Gold Nanoparticle", *Science* **299**, pp. 1877-1881, 2003.
- [20] K. Bogunia-Kubik and M. Sugisaka, "From molecular biology to nanotechnology and nanomedicine", *Biosystems* **65**, pp. 123-138, 2002.
- [21] J. Zheng, Z. Zhu, H. Chen, and Z. Liu, "Nanopatterned Assembling of Colloidal Gold Nanoparticles on Silicon", *Langmuir* **16**, pp. 4409-4412, 2000.
- [22] Y. Xia, J. A. Rogers, K. E. Paul and G. M. Whitesides, "Unconventional Methods for Fabricating and Patterning Nanostructures", *Chem. Rev.* **99**, pp. 1823-1848, 1999.
- [23] Ferdi Karadas, Gulay Ertas, Eda Ozkaraoglu, and Sefik Suzer, "X-ray Induced Production of Gold Nanoparticles on a SiO<sub>2</sub> / Si System and in a Poly(methyl methacrylate) Matrix", *Langmuir* **21**, pp. 437-442, 2005.



- [24] G. Frens, "Controlled nucleation for the regulation of the particle size in monodisperse gold solutions", *Nature*, **241**, pp.20-22, 1973.
- [25] J. T. Sheu , C. C. Chen, P. C. Huang, Y. K. Lee and M. L. Hsu, "Selective Deposition of Gold Nanoparticles on SiO<sub>2</sub> / Si Nanowires for Molecular Detection", *J. Jpn. Appl. Phys.*, **44** (4B), pp. 2864-2867, 2005.



## Chapter 4.

# Low Electron Energies of Scanning Probe Electric-filed-induced Bond Breaking Lithography

A new approach is introduced for selective deposition of colloidal gold nanoparticles (AuNPs) onto the surface of an unpatterned self-assembled monolayer (SAMs). Patterning of *N*-(2-aminoethyl)-3-aminopropyltrimeth-oxysilane (AEAPTMS) SAMs is realized by local filed-induced bond breaking using scanning probe lithography (SPL) on the thin SiO<sub>2</sub> surface. Different tip / sample biases were investigated for the bond breaking efficiency of AEAPTMS SAMs. It is found that the bond breaking efficiency is limited by the tunneling current through the thin SiO<sub>2</sub> film so that both the tip bias and tip scanning speed play the important roles. AuNPs with negative-charged citrate surfaces were selectively anchored on the SPL-unpatterned regions via electrostatic force between AEAPTMS SAMs and AuNPs. Single digit numbers of AuNPs anchored onto unpatterned AEAPTMS SAMs were demonstrated.

### 4.1 The invention review of low-dimensional novel patterning

Recently, many advanced techniques to make low-dimensional assemblies of colloidal nanoparticles in fabrication of nanostructures are essential for developing and capitalizing upon the emerging field of nano-science [1-4]. One of the major themes of nanotechnology has been the search for techniques for self-assembling nanoparticles to construct architectures on a solid-state surface for different applications. Novel patterning approaches of AuNPs have been made on the sub-100 nm scale resolution by using electron-beam lithography [5,6] and dip-pen nanolithography (DPN) [7], microcontact printing ( $\mu$ CP)[8] and scanning probe lithography (SPL)[9-11]. For foregoing burgeoning lithography applications of the nanoscience, selectively positioning chemical component molecules into a desired region on a solid silicon dioxide surface is a crucial technique. Among advanced lithography methods, scanning probe lithography with a lot of potential has been demonstrated as a powerful tool in nanofabrication [11-15]. SPL is a high-resolution patterning technique that uses a conductive tip to pattern a thin layer of electron sensitive material or conductive surface. On the other hand, self-assembled

monolayers (SAMs) [16, 17] technology provides one easy route towards surface functionalization with organic molecules containing functional groups like, -SH, -COOH, -NH<sub>2</sub> and silanes, on the selected metallic as well as semiconductor surfaces. A trimethylsilyl chemical monolayer on a thin silicon dioxide surface can be locally removed by the SPL technique was well-known [18-21]. In this section, the patterning region where the monolayer had been removed was then selectively modified with a second self-assembled monolayer of organosilane molecules. In 2002, Dr. S. Hoepfner [22] et al. combined the surface self-assembly method with a nano-electrochemical patterning process by the conductive AFM tip. A second highly ordered long-tail nonadecenyltrichlorosilane (NTS) monolayer is then allowed to selectively self-assemble on the top of the AFM-patterned OTS monolayer, thus the terminal ethylenic function groups of NTS are subsequently photo-reacted with H<sub>2</sub>S. Dr. X. Ling [10] et al. and Dr. H. Sugimura [18] et al. reported similar results with a two-step surface modification, i.e., electrical-field induced local oxidation removal of an octadecyltrichloro-silane (OTS) self-assembled monolayer through SPL process, followed by the selective chemisorptions of a second monolayer of (3-aminopropyl)-triethoxyl-silane (APS) molecules, resulting in the creation of a self-assembled monolayer (SAMs) confined to the SPL-defined patterns. The selective deposition of APS on OTS assembled monolayer, which resulted in the assembly of latex gold nanoparticles outside of the oxide domains. Using SPL technique, control and selective binding of the component chemical organic molecules can be achieved on a desired functionalized-surface pattern that can be linked to two different chemical molecules. Moreover, it is already known that tunneling electrons can be used to break chemical molecular bonds on the conductive metal surface by using the scanning tunneling microscopy method [23, 24].

This chapter describes the single-step surface modification process, i.e., a straightforward SPL field-induced bonds breaking for the patternwise placement of AuNPs with nanometer resolution on the SiO<sub>2</sub> surface was successfully demonstrated. The organic amino-functional AEAPTMS molecules that possess two amino groups act as linkers for enhance the selective deposition probability of gold nanoparticles on the SiO<sub>2</sub> surface. The bonds-breaking pattern is defined using an atomic force microscope (AFM) to apply a negative bias between the conductive AFM-tip, and selected locations of a modified silicon dioxide surface with AEAPTMS SAMs. Figure 4.1(a) shows the SPL bond breaking mechanism for the amino-functional silanation modified SiO<sub>2</sub> surface of a silicon substrate.

After SPL bond breaking of AEAPTMS SAMs, the  $\text{NH}_3$  functional groups, backbone of AEAPTMS and Si-O head groups of aminosilane modified surfaces were decomposed, and SPL patterning region was also not connected with citrate-stabilized AuNPs. The sample is then directly self-assembled with 15 nm citrate-coated AuNPs, and AuNPs were selectively anchored on the unexposed area via Coulombic force between silanation modified surfaces and the gold nanoparticles, as shown in Figure 4.1(b).

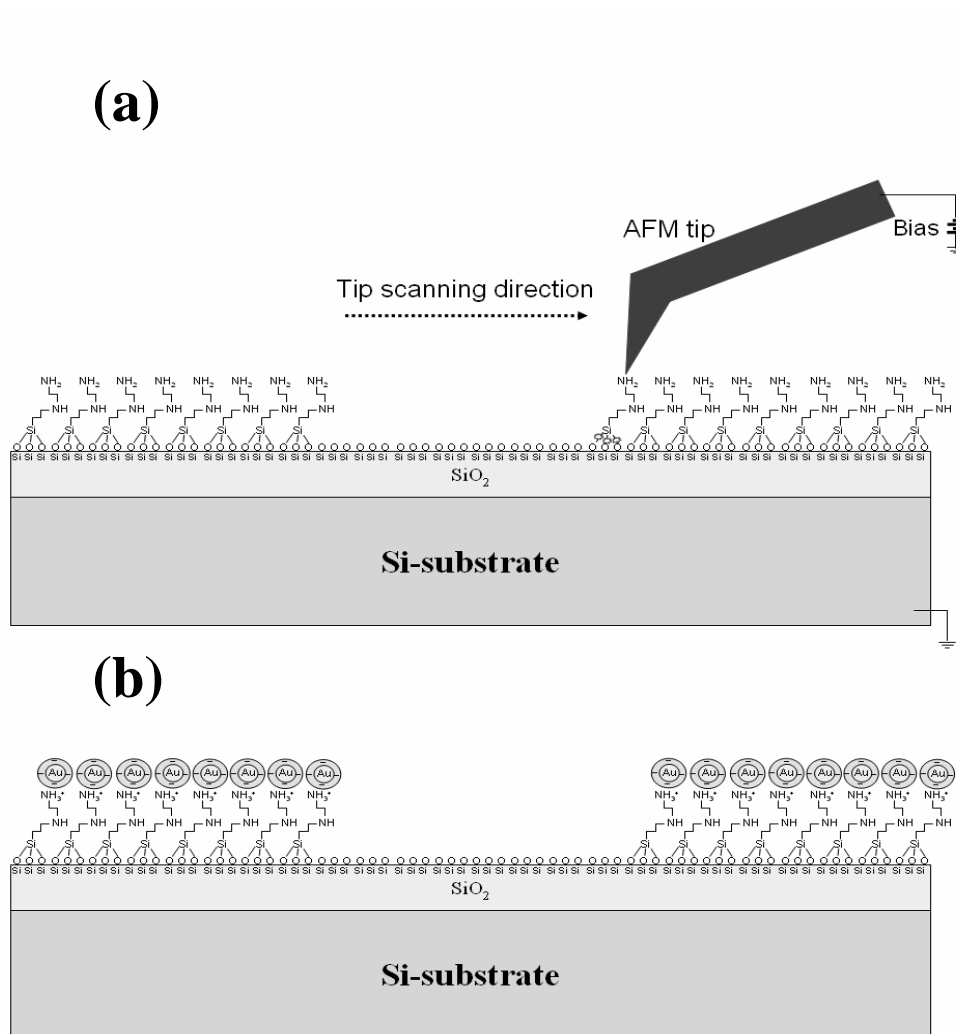


**Figure 4.1** (a) The mechanism of deposition of a monolayer of AEAPTMS molecules on the hydroxyl-terminal surface of an oxidized silicon substrate. (b) The schematic diagram of citrate-stabilized AuNPs was selectively anchored on the unexposed area.

This straightforward patterning technique is successfully demonstrated for selective

deposition of few AuNPs on the thin SiO<sub>2</sub> surface of silicon substrate, and it also can be used to fabricate any structure patterns on the SiO<sub>2</sub> surface. Citrate-stabilized gold nanoparticles were selectively anchored on the unpatterned area via electrostatic force between aminosilane modified surfaces and the gold nanoparticles as show in the Figure 4.2.

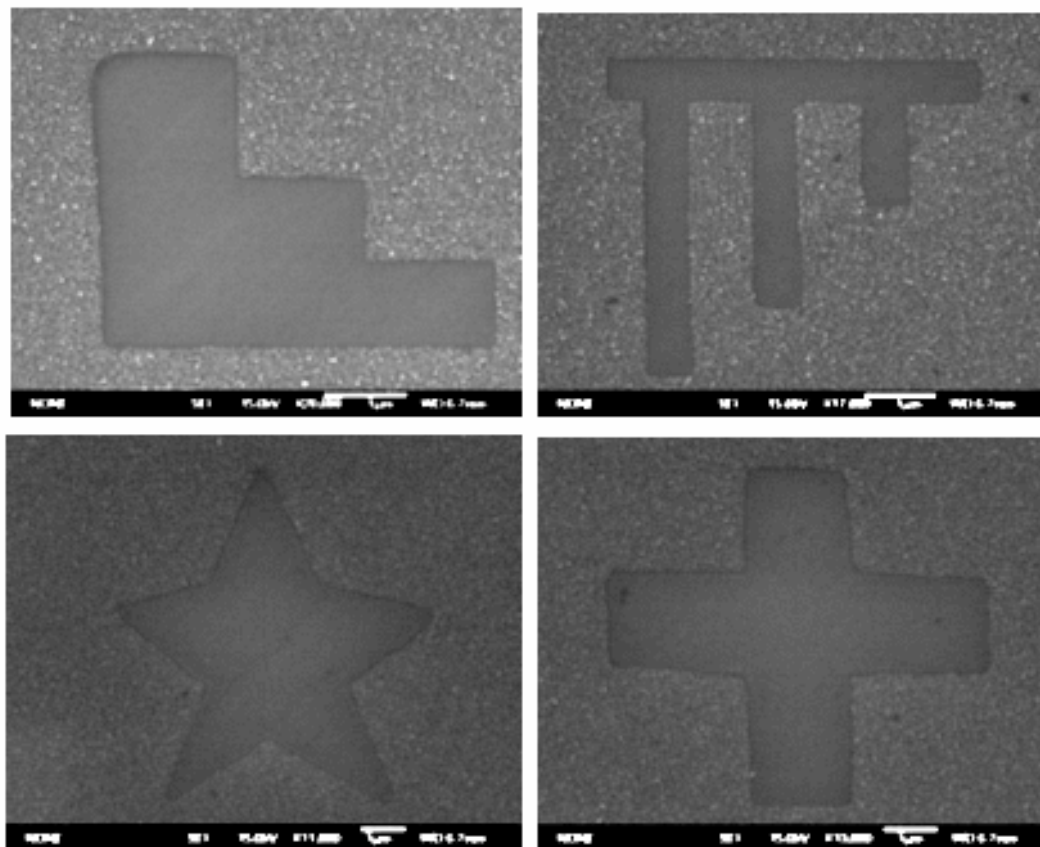


**Figure 4.2** SEM images of the citrate-stabilized AuNPs were selectively anchored on the SPL bond breaking unexposed area.

## **4.2 Experimental details of SPL bond breaking patterning of amino-silanation modified SiO<sub>2</sub> surface**

In the experiments, (100) silicon wafers were cleaned by standard RCA cleaning process to remove surface organic contamination. The hydroxyl-terminal surface of the oxidized silicon substrate was prepared by immersing the silicon sample into a piranha solution [1 : 3 (v / v) mixture of H<sub>2</sub>O<sub>2</sub> and H<sub>2</sub>SO<sub>4</sub>] for 10 min at 120 °C, rinsed copiously with de-ionized water (>18.5 MΩ/cm), and blown dry with N<sub>2</sub> gas. The thickness of the SiO<sub>2</sub> layer is about 2.5 nm and the surface roughness of the OH-passivated sample was

around 0.562 nm measured by AFM.

The aminosilane modified SiO<sub>2</sub> surfaces were prepared by immersing the OH-passivated samples into a 2.2 mM AEAPTMS solution for 15 min, rinsed copiously with de-ionized water, dried with N<sub>2</sub> gas and baked at 120 °C for 30 min on a hot-plate. After the dehydration procedure, aminosilane monolayer formed on the hydroxyl-terminal surface, which provided a surface bearing free amine (-NH<sub>2</sub>) functional groups, SAM backbone and Si-O head group. The bond energy of N-H is about 386 KJ/mol (4.0 eV), the bond energy of C-N is about 305 KJ/mol (3.16 eV), and the bond energy of Si-O is about 452 KJ/mol (4.68 eV) [25]. The contact-mode SPL bonds breaking experiments were carried out under ambient conditions (tip drawing speed = 0.5 μm/sec, set point = 0.5 V, temperature = 26 ± 0.5 °C, relative humidity = 58 ± 1%) on the aminosilane modified SiO<sub>2</sub> surface by applying dc voltages (4.0~ 6.5 V) between the PtIr-coated conductive AFM-tip and the SiO<sub>2</sub> surface. The electric field for bonds breaking is usually higher than  $1.6 \times 10^7$  V/cm which is in the Fowler-Nordheim tunneling for thin SiO<sub>2</sub> film.

The useful lateral force microscopy (LFM) image shows differences in tip-sample surface friction properties as the AFM tip scanning moves relative to the substrate. Before SPL bond breaking, the LFM scanning images show no contrast which also demonstrated that the AFM tip loading force was very small and no different frictional properties on the substrate surface. It was suggested that the AFM scanning operation without any mechanical contact damage. On the other hand, when SPL bonds breaking under ambient conditions, a water meniscus layer will be present between scanning AFM tip and sample surface was in the attractive mode, which will appear an attractive force, of the order of -1.032nN to prevent the specimen mechanical contact damage (scratching). Also, the citrate-coated AuNPs were prepared by Frens's synthesis method [26]. The SPL bonds breaking patterned sample was immersed in a solution of 15 nm citrate-coated AuNPs for 1.5 h. Then the sample was rinsed with de-ionized water and dried with N<sub>2</sub> gas. This procedure led to the selective deposition of AuNPs on the unpatterned region the electrostatic force. X-ray photoelectron spectroscopy (XPS) and lateral force microscopy (LFM) were used to evaluate the surface chemical composition of generated patterns and surface morphology before and after SPL bond breaking at different bias. Also, samples after selectively deposition of AuNPs onto the SiO<sub>2</sub> surface were characterized by XPS. Scanning electron microscopy (SEM) was used to observe the deposition of AuNPs on the patterned area.

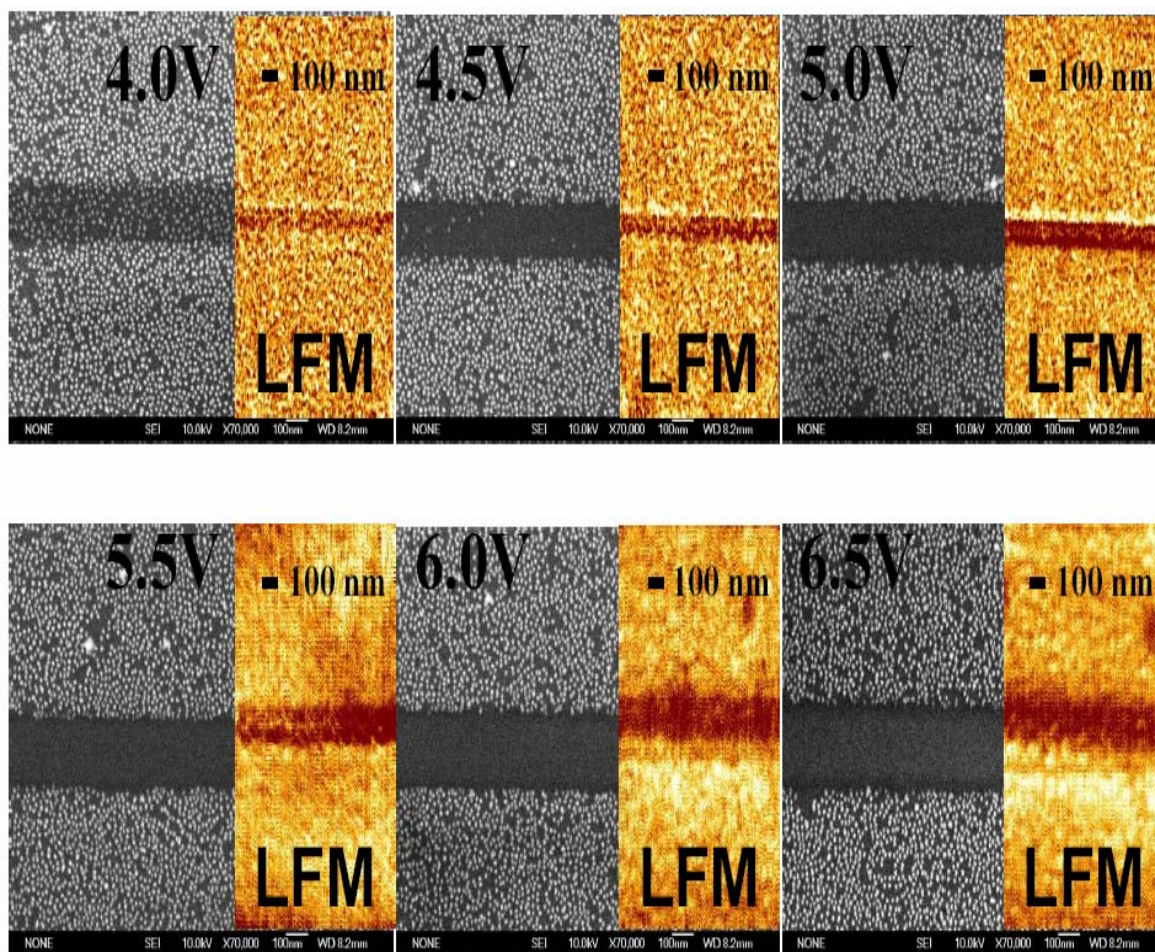


**Figure 4.3** SEM images show that efficiency of SPL bond breaking with selective deposition of AuNPs under different tip-sample bias (4.0 V to 6.5 V) and a control drawing speed  $0.5 \mu\text{m}/\text{sec}$  onto  $2.5 \text{ nm SiO}_2$  surface. Right-side inset shows lateral force microscopy (LFM) images of SPL bond breaking patterns on  $\text{SiO}_2$  surface before AuNPs selective deposition process.

### 4.3 Efficiency of SPL bond breaking with selective deposition

SPL bond breaking technique always can be applicable to any organic amino-functional trimethoxysilane chemical molecules SAMs on the silicon dioxide surface, such as 3-methacryl-oxypropyl-trimethoxysilane (MPTMS), (3-aminopropyl)-triethoxysilane (APS), 3-aminopropyl-trimethoxysilane (APTMS), *N*-(2-aminoethyl)-3-aminopropyl-trimethoxysilane (AEAPTMS). This procedure led to the selective deposition of AuNPs on the SPL unexposed region via interaction of the static charge between silanation modified regions and gold nanoparticles. This technique is always applicable to anchor any nano-metal particles SAMs (such as: platinum, gold, silver, etc.) with negative

ions on the hydroxyl-terminated surface. The bonds breaking effect of AEAPTMS SAMs was conducted by SPL field-induced bond breaking with tip bias 4.0 ~ 6.5 volts and self-assembly of AuNPs onto the thin 2.5 nm SiO<sub>2</sub> surface as shown in Figure 4.3. Right-side inset shows lateral force microscopy (LFM) images of SPL bond breaking patterns on SiO<sub>2</sub> surface before AuNPs selective deposition process, and LFM images were used to differentiate regions on the amino-modified oxide surface regions and SPL bond breaking patterns. Based on the experiments, at tip bias less than 4.5 volts, the SPL can not effectively decompose the AEAPTMS SAMs. In the low bias condition, both the charge energy and the current density are not enough to completely cleave the N-H bonds, C-N bonds on the SiO<sub>2</sub> surface. Although the decomposition of AEAPTMS SAMs was observable using LFM when bias less than 4.5 volts, AuNPs still anchored on the SPL patterned surface with lower density.

It is believed that insufficient bond breaking occurred when bias of SPL is less 4.5 volts and a small amount of AEAPTMS with NH<sub>2</sub> still binding on the SiO<sub>2</sub> surface. Although the real electrochemical reaction on the surface is complicated, the tunneling current through the thin SiO<sub>2</sub> film still has to be the dominant role. If the electric field across the oxide is strong enough, the barrier become thinner so that current increase exponentially.

Furthermore, Figure 4.4 shows that the linearity relationship curves of the linewidths of AEAPTMS bond breaking patterns with respect to SPL tip / sample bias under a control relative humidity ( $58 \pm 1$  %). Grid line bond breaking patterns on the SiO<sub>2</sub> surface were obtained by SPL at an electrical-stimulation tip bias from 4.0 V to 6.5 V. The pattern width was measured by the lateral force microscopy (LFM). It was found obviously that the linewidth of SPL bond breaking patterns increased with the SPL electrical-stimulation tip / sample bias increased. From LFM analysis, the linewidths of SPL bond breaking patterns corresponding to the tip bias are 114.2, 142.5, 172.5, 212.2, 235.6, and 254.5 nm, respectively. After AuNPs selective deposition process, the linewidths of SPL bond breaking patterns corresponding to the tip bias become 154.2, 182.6, 204.3, 226.1, 260.9, and 282.6 nm, respectively, measured by SEM images analysis. It was suggested that AuNPs were not anchored on the edge parts of SPL bond breaking grid line patterns; so that the linewidths of SPL bond breaking patterns become wider after the AuNPs deposition process. SPL bond breaking AEAPTMS patterns were performed on



hydroxyl-terminated surfaces with precise control of pattern shape and feature size. By way of SPL control and selective binding of AuNPs can be achieved on the amino-functionalized surface that can be widely used for a variety of bio-medical applications.

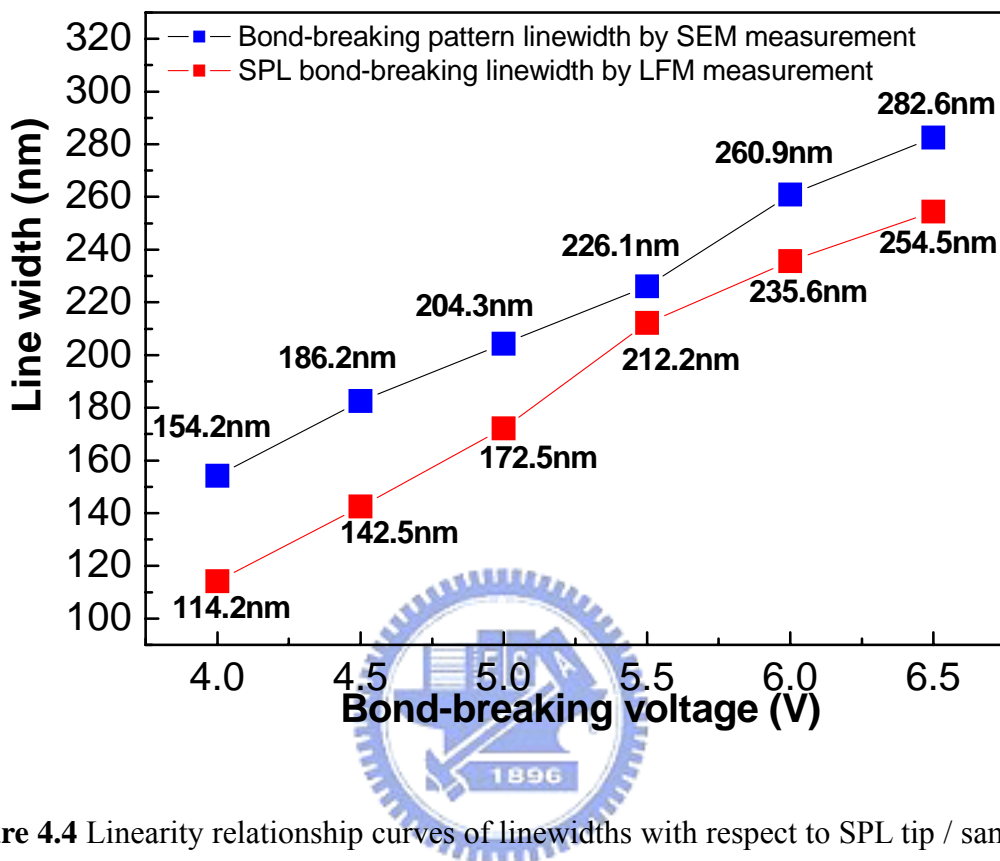


**Figure 4.4** Linearity relationship curves of linewidths with respect to SPL tip / sample bias for AEAPTMS SAMs bond breaking under a control relative humidity ( $58 \pm 1\%$ ).

#### 4.4 The mechanism of SPL field-induced bond breaking

When a silicon dioxide insulator is thin enough, it is possible for electrons and holes to tunnel through it. Figure 4.5 shows the tunneling current density for 2.5 nm silicon dioxide thicknesses as a function of the voltage across silicon dioxide ( $V_{ox}$ ). This figure shows that different tunneling effects dominate different voltage across silicon dioxide of regions. The most commonly seen tunneling effects can be classified into three categories according to their physical mechanisms: trap-assisted tunneling, direct tunneling, Fowler-Nordheim tunneling.

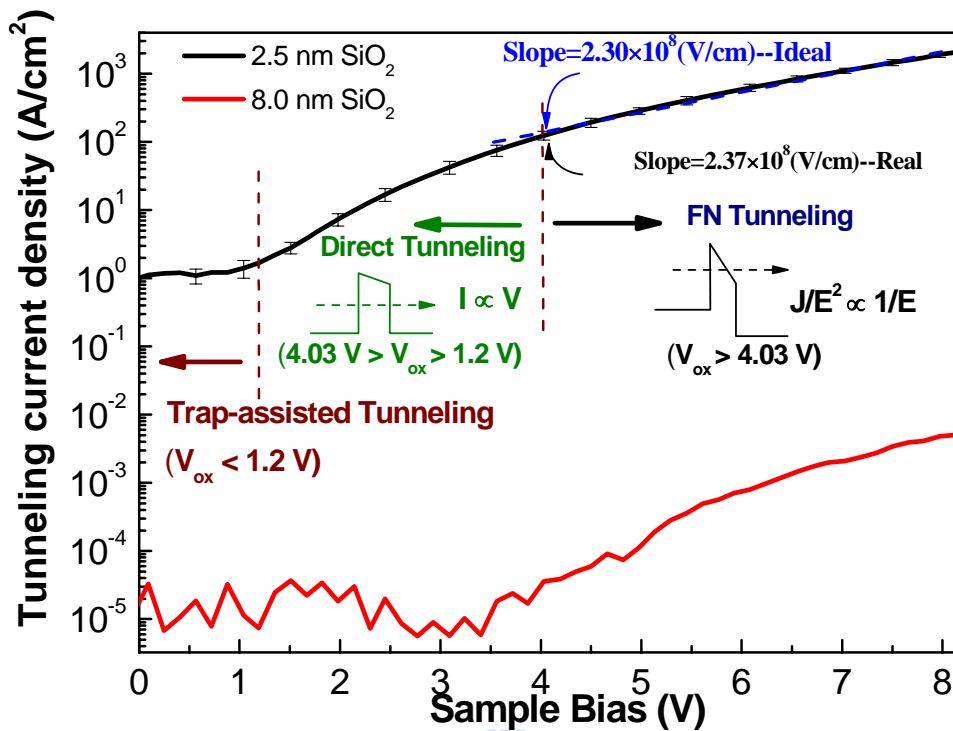


**Figure 4.5** Tunneling current densities for 2.5 nm silicon dioxide thicknesses as a function of the voltage across silicon dioxide ( $V_{ox}$ ). This figure shows that different tunneling effects dominate different voltage across silicon dioxide of regions.

If the electric field across the oxide is strong enough, it causes band bending which makes the barrier thinner. The tunneling current therefore gets higher as the silicon dioxide insulator gets stronger. This field dependent tunneling effect is called Fowler-Nordheim tunneling. Direct tunneling can occur in a very thin oxide at very low electric field. The direct tunneling current can be modeled by multiplying the Fowler-Nordheim tunneling current with a correction factor. Trap-assisted tunneling effect is assisted by the traps which are generated by the impurities in the oxide. This effect happens even at a fairly low electric field. Based on the theory calculation of the FN tunneling current model, the barrier of the 2.5 nm thin oxide layer is about 2.925 eV, and the effective mass in the oxide is about 0.538 electronic effective mass. The slope value of the plot of  $\ln(J_{FN}/E^2)$  versus  $(1/E)$  when the electrical field drop across the 2.5 nm thin oxide is about  $2.30 \times 10^8$  (V/cm). From the results, Figure 4.5 shows that if the voltage across silicon dioxide is lower than 1.2 V, it was suggested that the trap-assisted tunneling current dominates over direct

tunneling current. It was found that if  $V_{ox}$  between 4.03 V and 1.2V, direct tunneling current dominates over FN tunneling current. When the voltage across silicon dioxide is higher than 4.03 V, FN-tunneling dominates and the logarithm of the tunneling current increases with  $V_{ox}$  becomes the most significant. And, the slope value of the plot of  $\ln(J_{FN}/E^2)$  versus  $(1/E)$  when the 4.03 V drop across the thin oxide is about  $2.37 \times 10^8$  (V/cm). The value is very close to ideal value which was also confirmed the thin oxide is about 2.5 nm thickness. From the Figure 4.3 results, tip bias more than 4.5 V can effectively decompose the N-H bonds of AEAPTMS SAMs patterns. Based on this SPL experiments, it was found that the FN tunneling-current-induced bond stimulation dominated SPL bond breaking damage mechanism, and the energy is enough to completely cleave the all N-H bonds on the  $SiO_2$  surface.

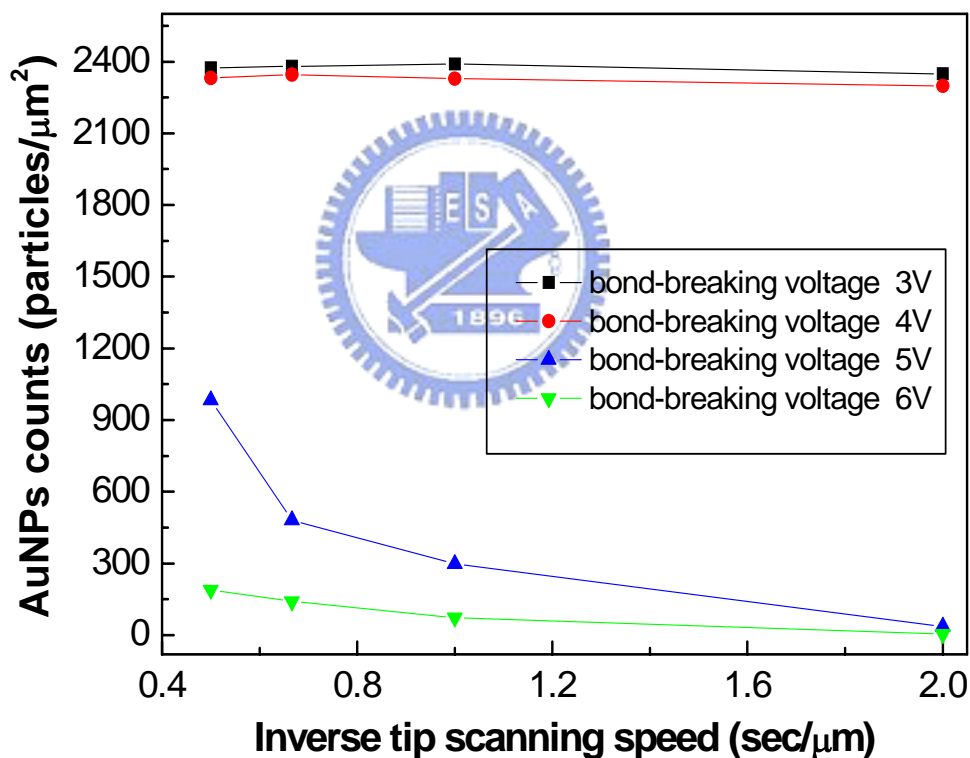


**Figure 4.6** AuNPs selective deposition on the SPL unexposed patterns for different bond breaking voltages as a function of the inverse tip scanning speed is exponential increased. For SPL tip bias is lower than 5 volts, the SPL bonds breaking energy is not enough to completely cleave N-H, C-N bonds on the  $SiO_2$  surface so that AuNPs were able to assemble onto the SPL bonds breaking patterns with lower density.

Figure 4.6 shows particle numbers of the selective deposition of AuNPs on the SPL bond breaking patterns for different tip / sample bias as a function of the inverse tip scanning speed. It was observed that AuNPs selective deposition of SPL bond breaking patterns decreased with the decrease of SPL tip scanning speed (i.e. the SPL bond breaking reaction time increased).

For SPL tip / sample bias smaller than 5 volts, the SPL bond breaking energy is not enough to decompose N-H bonds of AEAPTMS SAM completely, both the charge energy and the tunneling current density are not enough to completely cleave among N-H bonds (4 eV), C-N bonds (3.16 eV), Si-O bonds (4.68 eV) on the SiO<sub>2</sub> surface, and remained small amount of AuNPs assembled onto the SPL patterns. For SPL tip / sample bias higher than 5.0 volts, Fowler-Nordheim tunneling dominates completely because of the high electric field (> 10 MV/cm) and the logarithm of the tunneling current increases exponentially with tip / sample bias [27]. Furthermore, Figure 4.6 also depicts that the tunneling current density increases exponentially with respect to the SPL bias, according to the numbers of assembled AuNPs.

High-resolution x-ray photoelectron spectroscopy (XPS) characterization with focus beam was conducted at the U5 beamline of National Synchrotron Radiation Research Center, Taiwan (NSRRC). Figure 4.7 shows the XPS analysis of N1s peak for the AEAPTMS SAMs at the regions of SPL patterns under for bias 0, 4, 5 and 6 volts. The nitrogen N1s peak decreased obviously as the tip / sample bias of SPL bond breaking increased. For tip / sample bias of SPL bond breaking lower than 5 volts, the nitrogen N1s signals are still observable. It implies that SPL bond breaking energy is not enough to decompose N-H bonds efficiently on the SiO<sub>2</sub> surface. When tip / sample bias of SPL bond breaking is higher than 5 volts, almost no nitrogen N1s signal is observable, showing that AEAPTMS SAMs are decomposed efficiently by SPL bond breaking, and residuals of nitrogen is beyond the detection limit of XPS. Results of selective deposition of AuNPs and XPS analysis on SPL bond breaking patterns are consistent that bond breaking is efficient when tip / sample bias is larger than 5 volts.

It isn't possible to determine which bond broken under ambient conditions. Because of the electrochemical reaction between scanning AFM-tip and sample surface under ambient water meniscus is more complicated. It was suggested that all bonds (N-H (4.0 eV), C-N (3.16 eV), and Si-O (4.68 eV)) does not break concurrently which the bond breaking

energy is not enough to completely cleave all bonds on the SiO<sub>2</sub> surface. From our results, SPL tip bias between 3 V and 4 V, the SPL bond breaking energy is not enough to completely cleave N-H bonds on the SiO<sub>2</sub> surface caused the parts of AuNPs were also assembled onto the SPL patterns. For tip bias more than 5 V, the energy is enough to effectively decompose among N-H, C-N and Si-O bonds of AEAPTMS SAMs patterns at random during SPL bonds breaking under ambient water meniscus conditions.

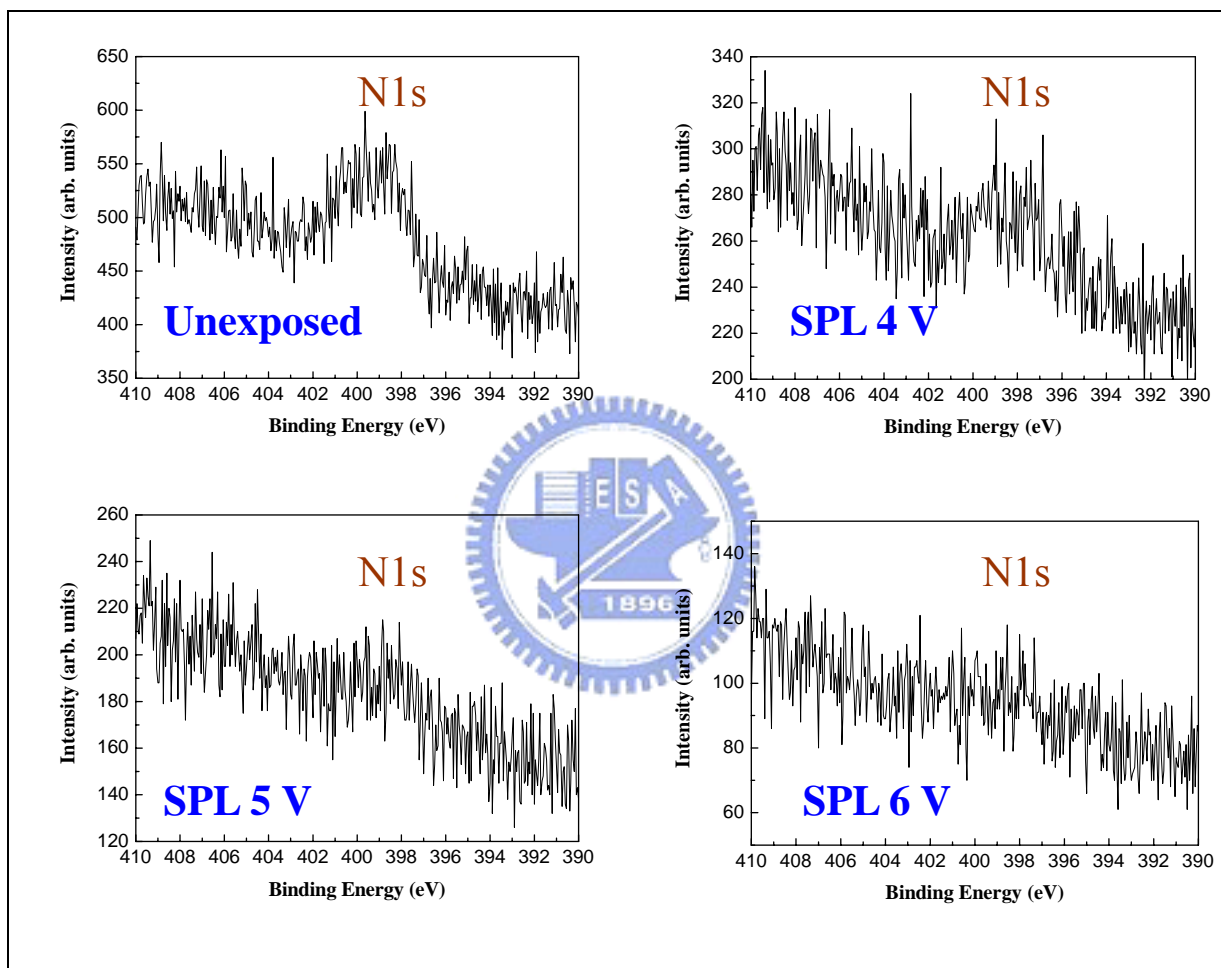


**Figure 4.7** XPS analysis exhibits the regions of the SPL of AEAPTMS SAMs bond breaking for the nitrogen N1s peak under different tip / sample bias. For tip / sample bias of SPL bond breaking lower than 5 volts, the nitrogen N1s signals are still observable. It implies that SPL bond breaking energy is not enough to decompose N-H bonds efficiently on the SiO<sub>2</sub> surface.

## 4.5 Low-dimensional patterning by using SPL bond breaking

Figure 4.8 show that SEM images of 15-nm AuNPs deposition on the arbitrarily triangles and squares patterns of unexposed silanation modification regions by applied a low energy of bias 6.5 V after immersion in the AuNPs solution for 1.5 h. As the SPL bond breaking sample was immersed in the colloidal gold solution, the  $\text{NH}_2$  groups become protonated, forming  $\text{NH}_3^+$ , and bind to the negatively charged citrate-passivated AuNPs onto the SPL unexposed regions.

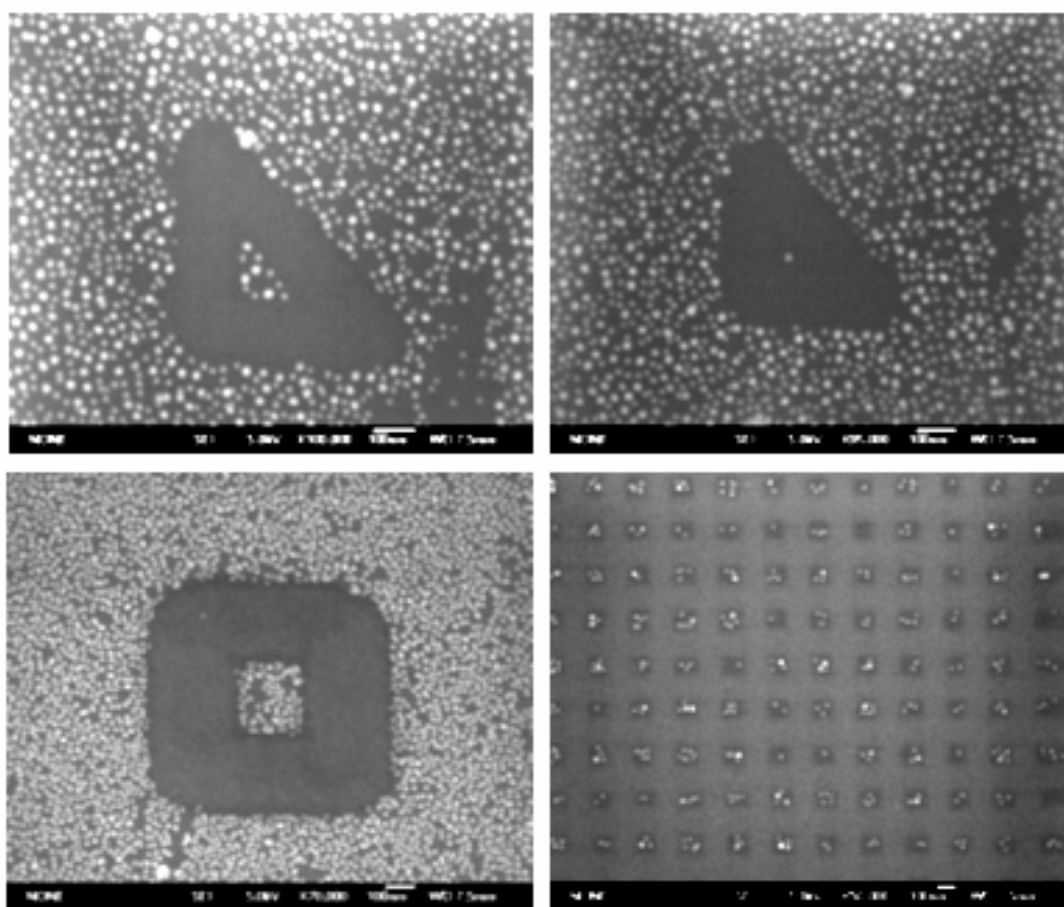


**Figure 4.8** SEM images of 15-nm AuNPs deposition on the desired triangles and squares patterns of unexposed silanation modification regions by applied the low energies of bias 6.5 V after immersion in the AuNPs solution for 1.5 h.

In this study, the amount of AuNPs (15 nm in diameter) are successfully controlled and selectively immobilized outside the SPL bond breaking grid line patterns were demonstrated on the  $\text{SiO}_2$  surface. SPL bond breaking technique combined with AuNPs SAMs process provided a super high selectivity of  $\sim 99.6\%$  AuNPs deposition. Line

pattern of gold nanoparticles were demonstrated as shown in Figure 4.9. This method allows fabrication of lines of 15 nm AuNPs in width, as well as the placement of individual AuNP on outside bond breaking region on the SiO<sub>2</sub> surface.

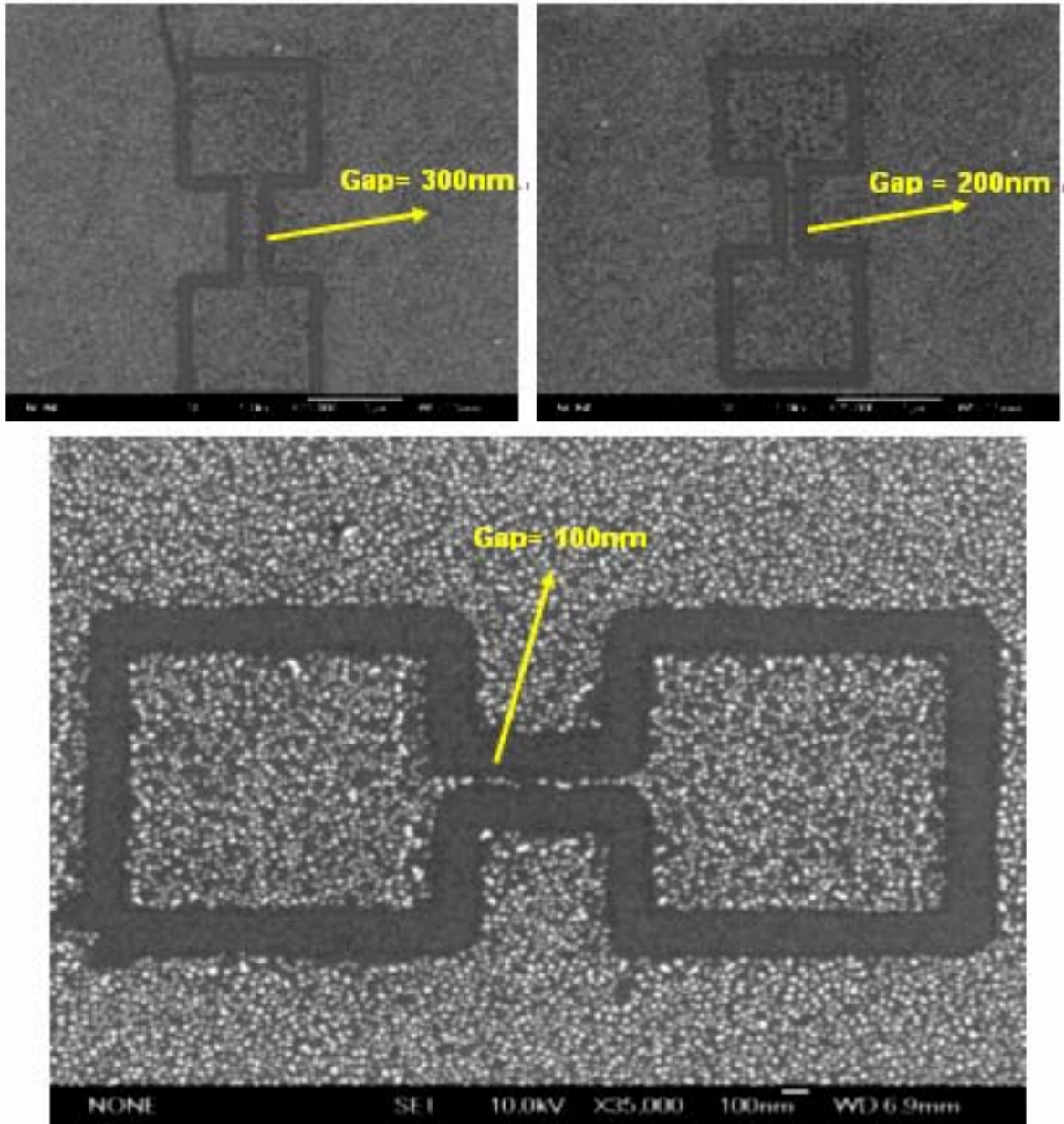


**Figure 4.9** SEM images show that the amount of 15nm AuNPs are successfully controlled and selectively immobilized outside the SPL bon breaking desired grid line patterns on the SiO<sub>2</sub> surface by applied the low energies of bias 6.5 V after immersion in the AuNPs solution for 1.5 h. The details of line patterns composed of single AuNPs on the SiO<sub>2</sub> surface. (a)Gap = 300 nm; (b)Gap = 200 nm; (c)Gap = 100 nm.

Figure 4.10 shows both the XPS survey analysis at region of SPL bond breaking patterns on the SiO<sub>2</sub> surface and at region outside the SPL bond breaking patterns after self-assembly of AuNPs. The tip / sample bias of SPL bond breaking is 6.5 volts. The Au 4f peaks corresponding to the gold nanoparticles (Au<sup>0</sup>) on the region outside the SPL bond breaking patterns on the SiO<sub>2</sub> surface are clearly observed. And, no Au 4f signal is observed at the SPL bonds breaking patterns on the SiO<sub>2</sub> surface showing that AuNPs selectively deposited only on the SPL unexposed patterns.

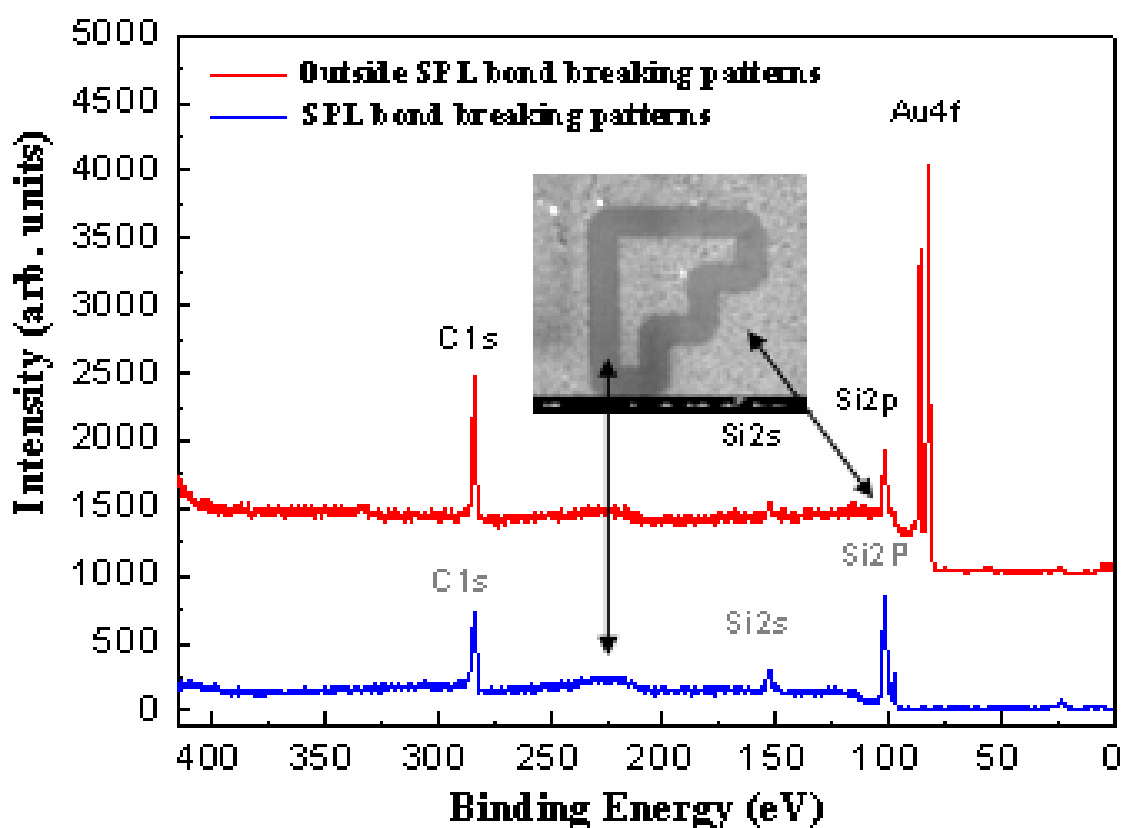
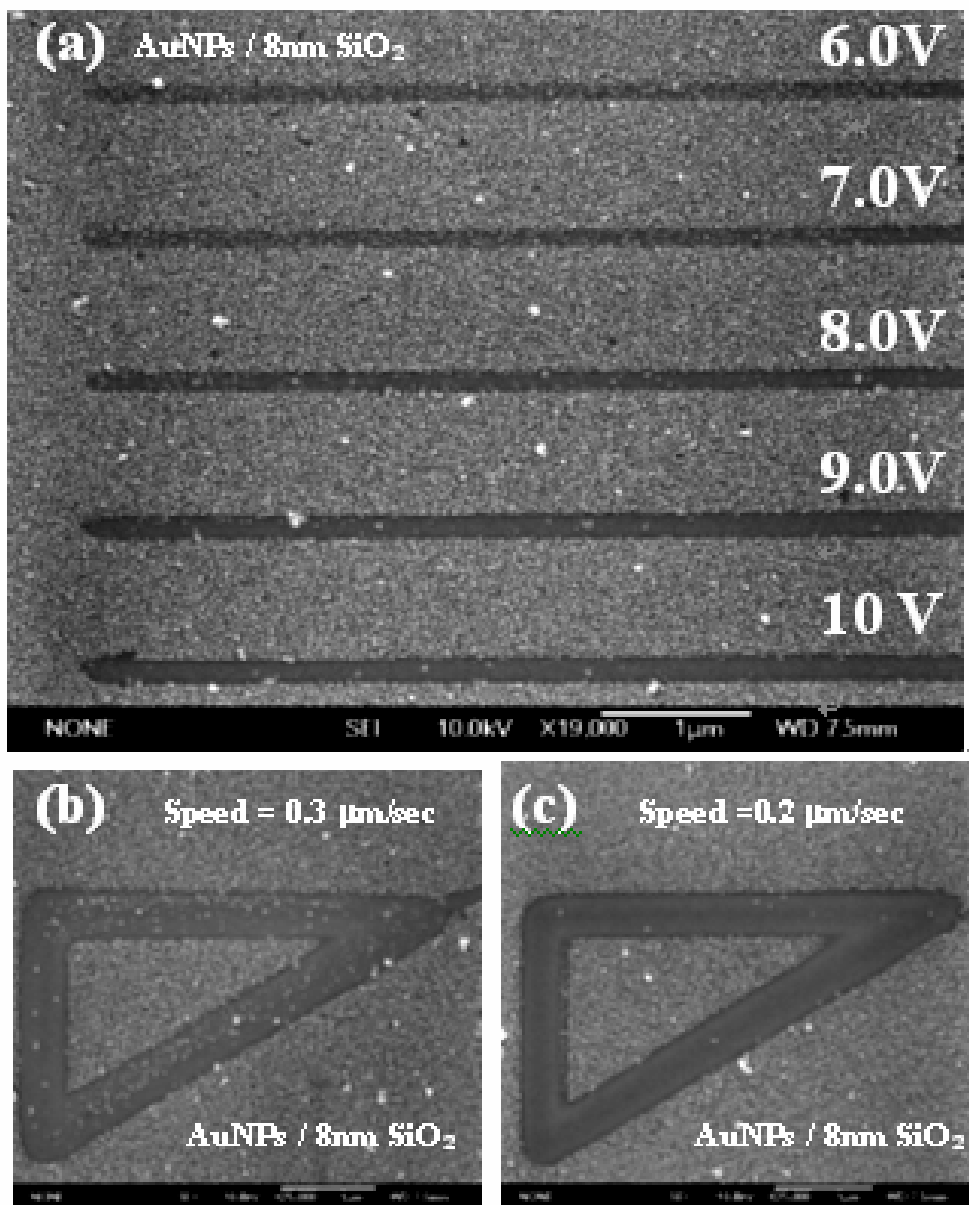


**Figure 4.10** Spectra of x-ray photoelectron microscopy at the regions of SPL bond breaking patterns and outside the SPL bond breaking patterns to evaluate the selectivity of AuNPs. The Au4f signal was observed clearly outside the SPL bond breaking area, and no Au4f signal was observed inside the SPL bond breaking area. The SPL bias and tip scanning speed is 6.5 volts and 0.5  $\mu\text{m}/\text{sec}$ , respectively.

In the past, Dr. T. Yoshinobu et al. [15] reported the oxide patterns can be drawn on the SC1-treated Si (about 0.6nm SiO<sub>2</sub>) surface by applying the anodizing voltage of 22 V between the AFM-tip and the silicon substrate. To confirm the bonds breaking effect of AEAPTMS SAMs is limited by tunneling mechanism, an 8-nm-thick thermal oxide layer

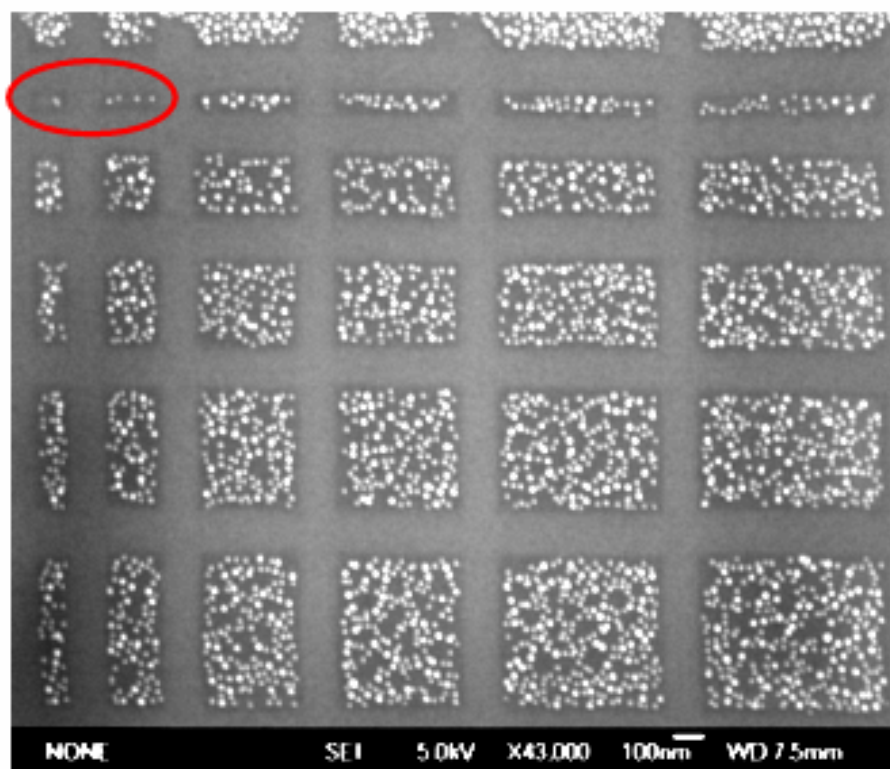


on silicon substrate was prepared by the thermo oxidation furnace at the process temperature of 950°C. The surface roughness was around 0.658 nm measured by AFM. The amino-silane modified SiO<sub>2</sub> surfaces were again prepared by immersing a 2.2 mM AEAPTMS solution for 15 min, and baked at 120 °C for 30 min.



**Figure 4.11** (a) SEM image shows that SPL bond breaking of AEAPTMS SAMs were successfully carried out by applying tip / sample bias from 6.0 to 10 volts at scanning speed of 0.2 µm/sec onto 8 nm SiO<sub>2</sub> surface. Tip scanning speed in SPL bond breaking plays an important role as shown in (b) 0.3 µm/sec, (c) 0.2 µm/sec at tip / sample bias of 10 volts.

SPL bond breaking of AEAPTMS SAMs were successfully carried out by applying tip/sample bias from 6.0 to 10 volts at a scanning speed of 0.2  $\mu\text{m}/\text{sec}$ . Figure 4.11 (a) shows that even at a bias of 10 volts, there is still small amount of AuNPs anchored on the SPL bond breaking patterns. Although tip scanning speed is slow down to accumulate more bond breaking current on AEAPTMS SAMs, the results is not as good as that demonstrated in the case of 6.5 volts for a 2.5-nm-thick  $\text{SiO}_2$  sample. Owing to the decreased electrical-field of SPL bond breaking was about  $\sim 1.25 \times 10^9$  V/m between the AFM-tip and the 8 nm  $\text{SiO}_2$  surface, tip bias less than 10 V can not effectively decompose the bonds of AEAPTMS SAMs caused the parts of AuNPs were also assembled onto the SPL patterns. Increase the tip scanning speed results in worse bond breaking as shown in Figure 4.11 (b) and Figure 4.11 (c).



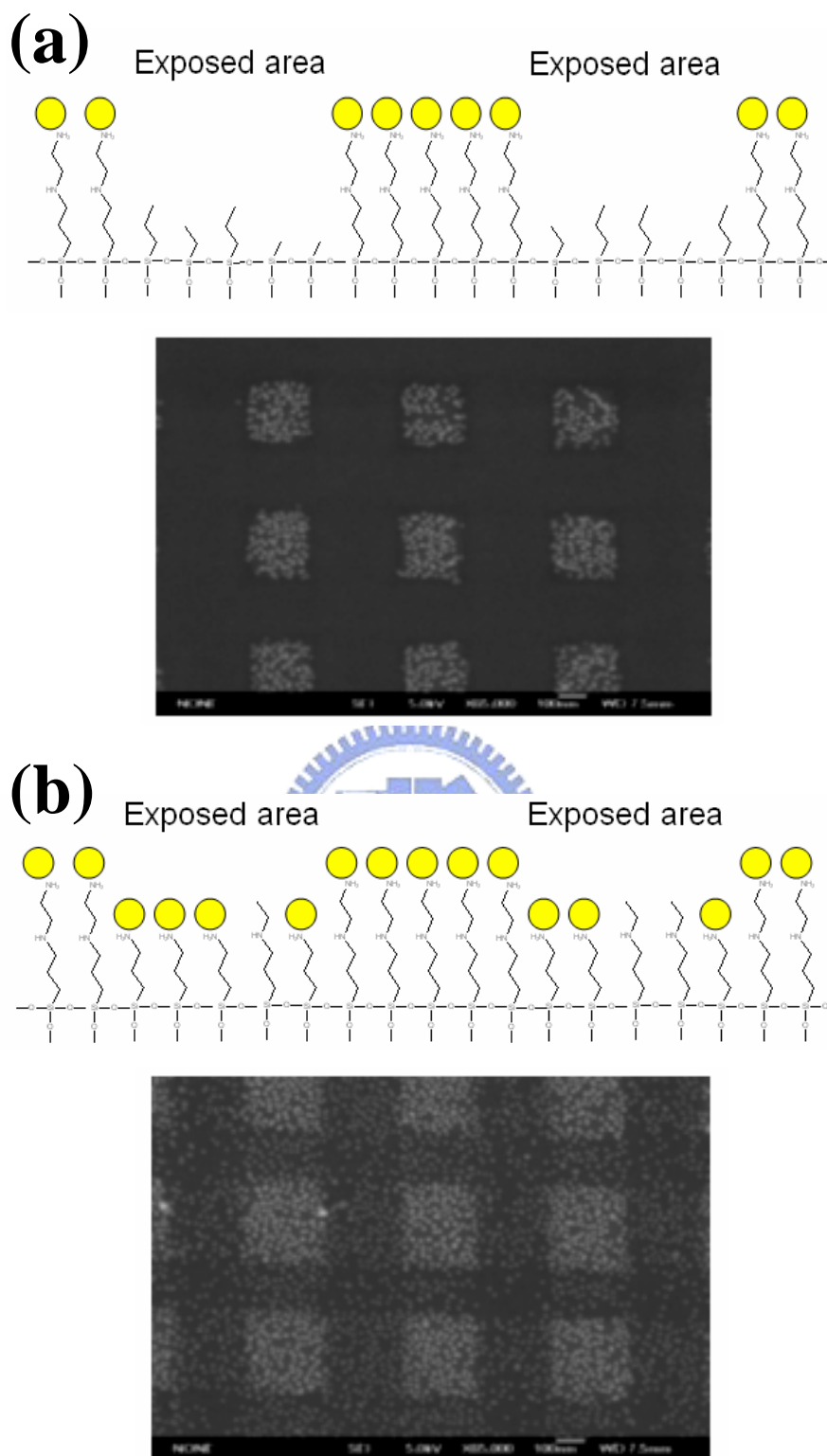
**Figure 4.12** SEM image shows deposition selectivity of 15-nm AuNPs on the regions of unexposed aminosilane modified surface. The SPL patterning pitches changed from 200 nm to 1  $\mu\text{m}$  (left to right) with tip / sample bias of 6.5 volts and immersion the sample in the AuNPs solution for 1.5 h. The numbers of AuNPs are confined spatially with electrostatic force on the area of unexposed patterns on the  $\text{SiO}_2$  surface down to single digit (circled).

Figure 4.12 shows the SEM image of 15-nm AuNPs deposition on the regions of unpatterned aminosilane modified surface. The SPL patterning pitches changed from 200 nm to 1  $\mu\text{m}$  (left to right) with tip / sample bias of 6.5 volts and immersion the sample in the AuNPs solution for 1.5 h. The numbers of 15 nm AuNPs are confined spatially on the area of unexposed patterns on the  $\text{SiO}_2$  surface. As circled in Figure 4.12, there are two AuNPs and four AuNPs anchored onto area of  $50 \times 100 \text{ nm}^2$  and  $50 \times 200 \text{ nm}^2$  unexposed AEAPTMS SAMs respectively. The proposed technique provides a simple process and a very reliable selectivity on anchoring AuNPs in nanometer scale resolution.

## 4.6 Interesting of SPL electric-filed induced gray-level selective patterning

The selective deposition of gold nanoparticles onto the silicon oxide by SPL bond breaking relates to various parameters, such as the additional bias amplitude, tip scan speed (duration of time), tip geometry, tip-substrate distance, and humidity. SPL bond breaking, as the electrochemical mechanism suggested, the water-meniscus between the tip and the substrate surface could work as an electrochemical nano-cell, and could provide hydroxyl ions, hydrogen radicals, and oxygen species for decomposing among N-H, C-N and Si-O bonds of AEAPTMS SAMs patterns at random under ambient. Since substrate surface water-bridge would be mainly supplied from the atmosphere by field-enhanced capillary condensation.

From my previous results, SPL nanolithography operated at a high electric-filed induced bond breaking condition, tip bias more than 5 V, the energy is enough to effectively decompose among N-H bonds, C-N bonds, and Si-O bonds of AEAPTMS SAMs patterns and gold nanoparticles were not able to assemble onto the SPL bonds breaking patterns as shown in Figure 4.13 (a). When the tip bias of the SPL bond breaking is lower than 4V, the SPL bond breaking energy is not enough to completely cleave N-H bonds on the  $\text{SiO}_2$  surface and caused the parts of AuNPs were also anchored onto the SPL patterns under ambient as shown in Figure 4.13 (b). Moreover, we observed an interesting phenomenon, *i. e.* the distribution densities of gold nanoparticles selective deposition become sparser when the SPL lithography operated at the lower electric-filed induced bond breaking conditions.



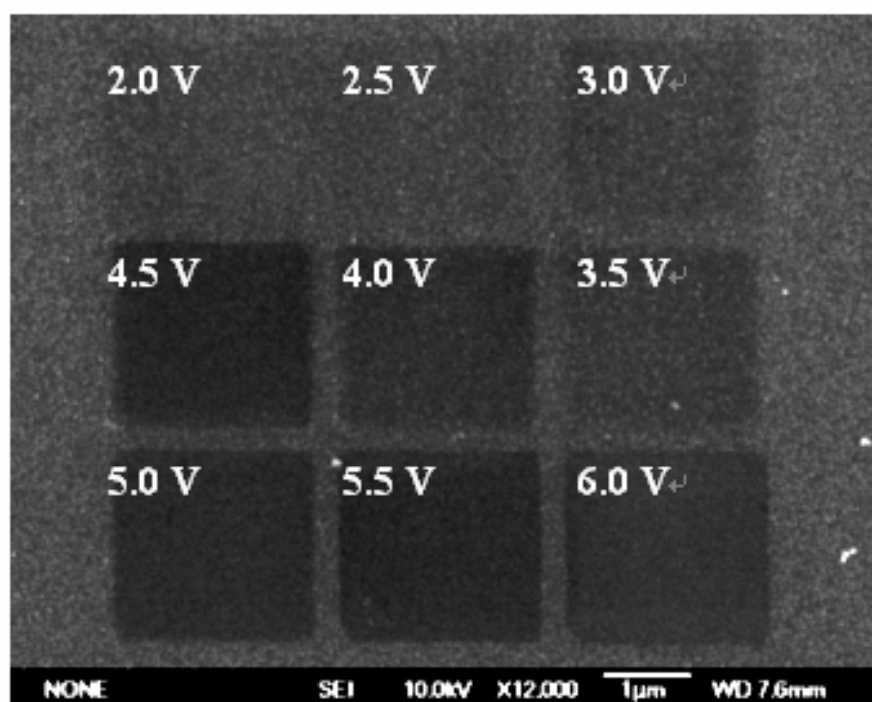
**Figure 4.13** SEM images of 15-nm AuNPs selective deposition on the desired squares patterns of unexposed silanation modification regions by applied the low energies of additional bias after immersion in the AuNPs solution for 1.5 h. (a) 5Volts and (b) 3.5Volts.

In order to confirm the ability of gray-level selective patterning by using the SPL electric-field induced bonds breaking method, a 2.5-nm-thick hydroxyl-terminal surface of the oxidized silicon substrate was prepared by immersing the silicon sample into a piranha solution for 10 min at 120 °C, rinsed copiously with de-ionized water, and blown dry with N<sub>2</sub> gas. The aminosilane modified SiO<sub>2</sub> surfaces were again prepared by immersing a 2.2 mM AEAPTMS solution for 15 min, and baked at 120 °C for 30 min. After the dehydration procedure, aminosilane monolayer formed on the hydroxyl-terminal surface, which provided a surface bearing free amine functional groups, SAM backbone and Si-O head group. SPL gray-level patterning of AEAPTMS SAMs were successfully carried out by applying tip / sample bias from 2.0 to 6.0 volts, the tip scanning speed, and ambient humidity were maintained on 0.5 μm/sec, and 60 ± 1%, respectively. Figure 4.14 shows the SEM images of the distribution densities of the 15-nm AuNPs selective deposition on the desired squares patterns of SPL-exposed silanation modification regions by applied the low energies of additional SPL bond breaking bias.

Figure 4.15 shows the characteristic relationship curve between the distribution densities of the gold nanoparticles selective deposition and SPL bond breaking voltages at room temperature. The ambient relative humidity was maintained on 60 ± 1%. It was appeared that the distribution densities of gold nanoparticles selective deposition decreased as the additional SPL tip bias increased.

It was suggested that the distribution densities of gold nanoparticles selective deposition were dominated by the additional SPL electrical-field-induced chemical bond decomposing effect. Distribution densities of the gold nanoparticles selective deposition on the SPL bond breaking exposed patterns as a function of the bond breaking voltages is decreased exponentially. It is believed that the proposed novel technique can be applicable to generate interesting gray-level selective patterning.

Figure 4.16 (a) shows that the black and white gray-level photograph of the physicist Dr. Richard P. Feynman with a 512 × 512 resolution. We choose the voltages range of the SPL gray-level patterning from 2.5 V to 5.5 V, the resolution of SPL bond breaking patterning is 11.71875 mV/grad, and the pitch of pixel is about 97.66 nm. The SPM-tip scanning speed, bond breaking reaction time of pixel, and ambient humidity were maintained on 7.5 μm/sec, 10 ms, and 60 ± 1%, respectively.



**Zoom in**

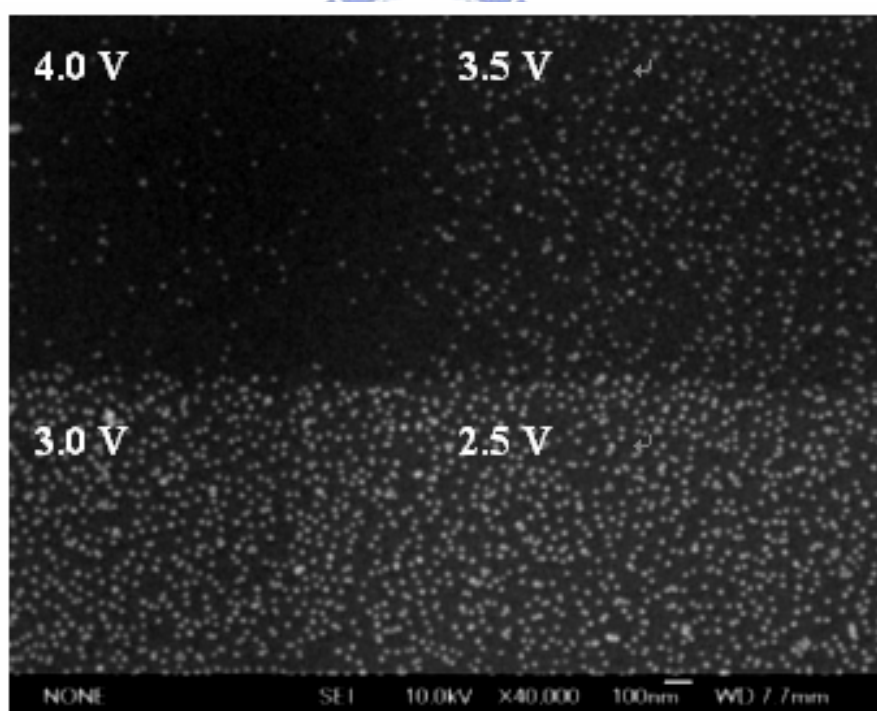


**Figure 4.14** SEM images of the distribution densities of the 15-nm AuNPs selective deposition on the desired squares patterns of SPL-exposed silanation modification regions by applied the low energies of additional bias after immersion in the AuNPs solution for 1.5 h. Additional SPL bond breaking voltages form 2.0 Volts to 6.0 Volts.

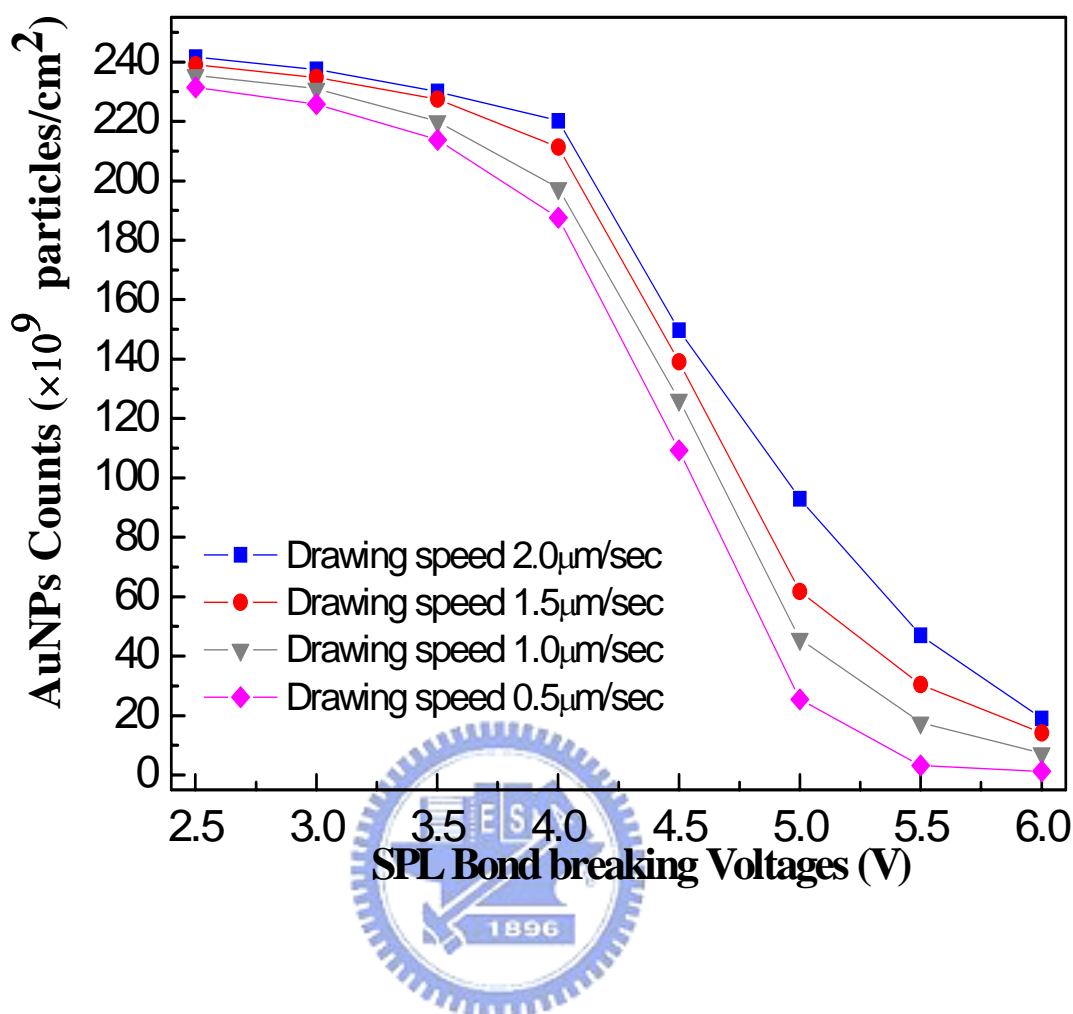


**Figure 4.15** Characteristic relationship curve between the distribution densities of the gold nanoparticles selective deposition on the SPL-exposed patterns and SPL bond breaking voltages at room temperature and the relative humidity was maintained on  $60 \pm 1\%$ .

Figure 4.16 (b) shows the SEM images of the AuNPs selective gray-level patterning on the SiO<sub>2</sub> surface by applied the low energies of additional bias after immersion in the AuNPs solution for 1 h. We have successfully demonstrated that the gray-level selective patterning on the 2.5 nm thickness silicon oxide surface by using the SPL electric-field induced bonds breaking method. Because of gold nano-particles have been widely used for variety applications, via a proper control, it is believed that the novel SPL bond breaking technique can be applicable to generate variety distribution densities of gold nanoparticles on the silicon oxide surface. The proposed nanofabrication technique may be further applied in both nanoelectronics and flash memory applications.

**(a)**



**(b)**



**Figure 4.16** (a) Black and white gray-level photograph of the physicist Richard P. Feynman (Resolution:  $512 \times 512$ ); (b) SEM images of the AuNPs selective gray-level patterning on the  $\text{SiO}_2$  surface by applied the low energies of additional bias after immersion in the AuNPs solution for 1 h. (SPL gray-level patterning voltages from 2.5 V to 5.5 V, the resolution of SPL bond breaking patterning is 11.71875 mV/grad, and the pitch of pixel is about 97.66 nm).



## 4.7 Gold nanoparticles selective anchored locally on SiNWs by using SPL bond breaking technique

Silicon nanowires can be prepared with single-crystal structures, diameters as nanometers scale and controllable hold and electron doping, and thus represent powerful integration for nanoelectronics devices such as field effect transistor. The SiNWs devices electrical characteristics are very sensitivity changed of the surface state. In this section, we had successfully fabricated the silicon nanowires devices on the bare silicon with SPL nanolithography and conventional processes. By this stable SPL nanolithography and conventional processes, we can fabricate the nano-scaled dimension of silicon nanowires stably. Herein, we used an atomic force microscopy, which usually employed in imaged the surface profiles by operating with a SPM-tip scanning around the sample surfaces. The locally additional electric-field between tip and sample surface forced the oxygen radical ions from the environment to penetrate into the sample surface and results in a thin silicon dioxide layer. The thickness and width of oxide patterns can be controlled by several factors: additional applied voltage between tip and sample surface, tip scanning speed, contact force between tip and sample surface, and humidity of the environment, which was discussed in detail in chapter 2. The silicon nanowires (SiNWs) with 120 nm wide and 10  $\mu\text{m}$  long on the p-type (100)-silicon substrate were fabricated by the scanning probe microscope (SPM)-based local oxidation technique and followed by anisotropic wet etching with tetramethylammonium hydroxide (TMAH) solution.

Then, the SiNWs sample was cleaned by standard RCA cleaning process to remove surface organic contamination. The hydroxyl-terminal surface of the SiNWs was prepared by immersing the silicon sample into a piranha solution for 10 min at 120  $^{\circ}\text{C}$ , rinsed copiously with de-ionized water, and blown dry with  $\text{N}_2$  gas. The amino-silane modified  $\text{SiO}_2$  surfaces of SiNWs were prepared by immersing the  $\text{OH}^-$ -passivated samples into a 2.2 mM AEAPTMS solution for 15 min, rinsed copiously with de-ionized water, dried with  $\text{N}_2$  gas and baked at 120  $^{\circ}\text{C}$  for 30 min on a hot-plate. We utilized the scanning probe nanolithography bond breaking technique to perform the desired patterns. The amount of 15 nm AuNPs are successfully controlled and selectively immobilized outside the SPL bond breaking desired square patterns were demonstrated on the  $\text{SiO}_2$  surface of SiNWs. Figure 4.17 shows gold nanoparticles selective anchored locally on SiNWs by using SPL

bond breaking technique. Tip / sample bias of SPL bond breaking is 6.5 volts and scanning speed is 0.5  $\mu\text{m}/\text{sec}$ , respectively.

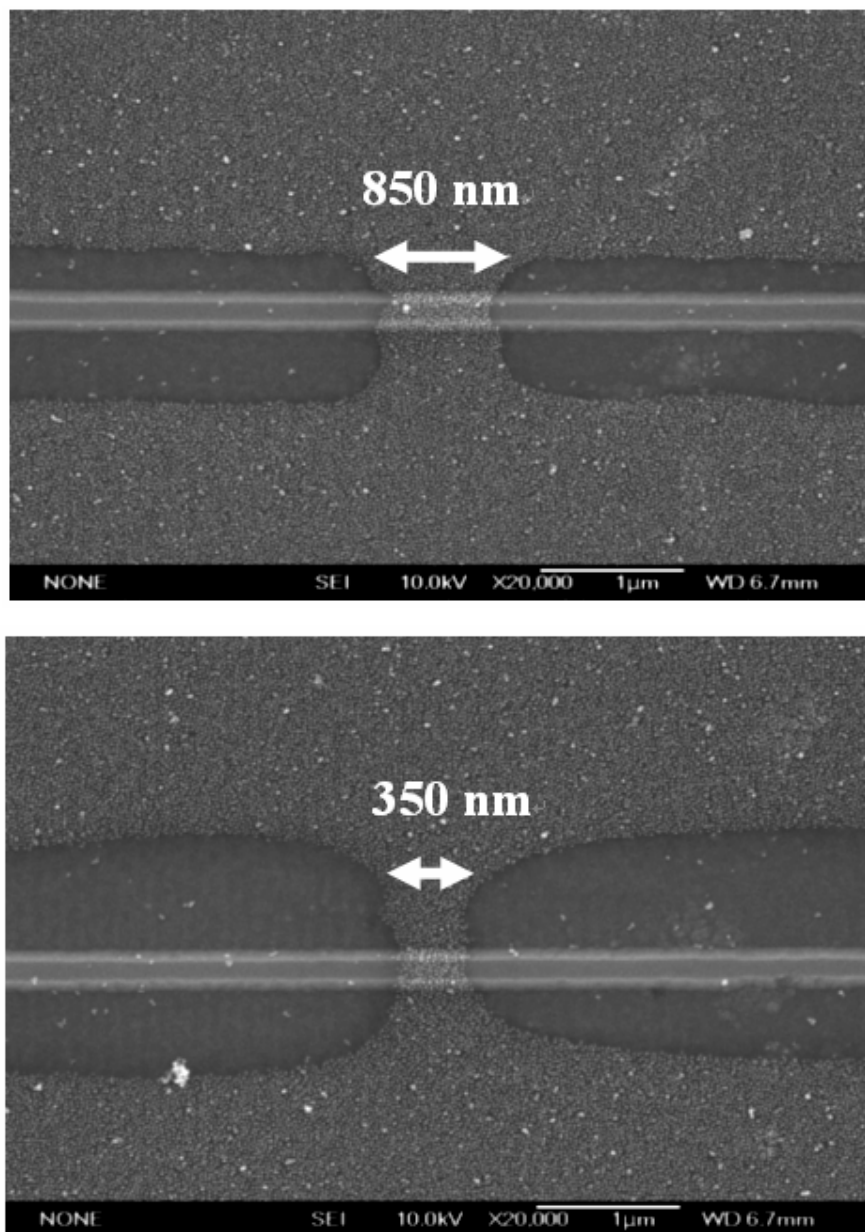


**Figure 4.17** SEM image shows selective deposition locally of 15nm AuNPs on the desired regions of unexposed aminosilane modified surface of silicon nanowires. SPL bond breaking patterning with tip / sample bias of 6.5 volts and immersion the sample in the AuNPs solution for 1.5 h. (a) desired region = 850 nm, (b) desired region = 350 nm.

It is observed that the amount of gold nanoparticles are successfully controlled and selectively immobilized outside the SPL bond breaking desired square patterns on the  $\text{SiO}_2$

surface of the SiNWs by using an additional SPL tip bias after immersion in the AuNPs self-assembly process.

#### 4.7.1 Modification of channel surface of silicon nanowires

Silicon nanowire devices represent a potential and powerful architecture to the conventional planar technology for electronic devices, because of the advanced electrostatic control of the channel via the gate voltage and the consequent suppression of short channel effects. At the nanometer-scales, due to the increasing surface to volume ratio, surface effects become predominant and can significantly modify the properties. The silicon nanowires devices are very sensitivity changed of the surface state and could affect the electrical characteristic of silicon nanowires device, we will fully study modification behaviors of channel surface of SiNWs devices in this section 4.7.1.

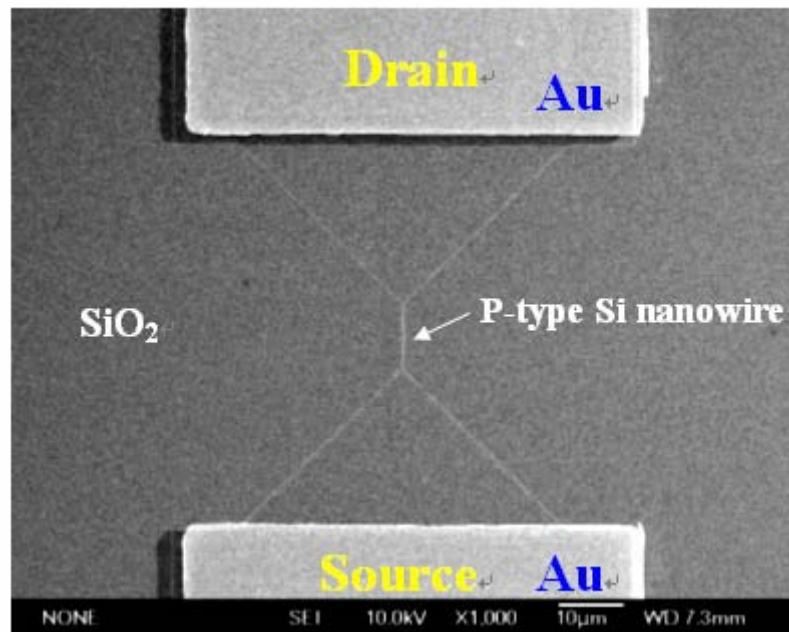


**Figure 4.18** SEM images of the p-type silicon nanowires were fabricated by E-beam nano-lithography with an anisotropic RIE dry etching process. The linewidth of nanowires was about 100 nm and 10 µm long.

In order to investigate the surface state changed by the chemical modification, the chemical-gated SiNWs devices were performed. Furthermore, our research results was found that the impact of chemical modification on the electrical characteristics of silicon nanowires devices. The silicon nanowires with 100 nm wide and 10 µm long on the p-type

(100) SOI substrate were fabricated by E-beam nano-lithography with an anisotropic RIE dry etching as shown in Figure 4.18. Schematics of different chemical molecular modifications of channel surface states of the p-type silicon nanowires devices as shown in the Figure 4.19. The p-type Si nanowires doped the high boron concentration with  $10^{19}$  (atoms/cm<sup>3</sup>). UV-Ozone (O<sub>3</sub>) treatment was applied to increase the siloxane bonds on channel surface of p-type Si nanowires for 10 mins, which led to higher density of AEAPTMS molecular bonding onto the channel surface of p-type Si nanowires. SiNWs samples then were immersed into AEAPTMS solution with concentration of 2.2 mM for 15 mins, and were rinsed copiously with de-ionized water and baked in 120 °C for 30 min. After the dehydration procedure, amino-silane monolayer formed on the hydroxyl-terminal surface. Additional contact-mode SPL electrical-field-induced chemical bond decomposing patterning were carried out desired patterns under ambient conditions on the amino-silane modified SiO<sub>2</sub> surface by applying dc voltages between the PtIr-coated conductive AFM tip and the SiO<sub>2</sub> surface. 15 nm-gold nanoparticles modification was carried out by immersing SiNWs sample modified by AEAPTMS into gold nanoparticles solution for 90 mins.

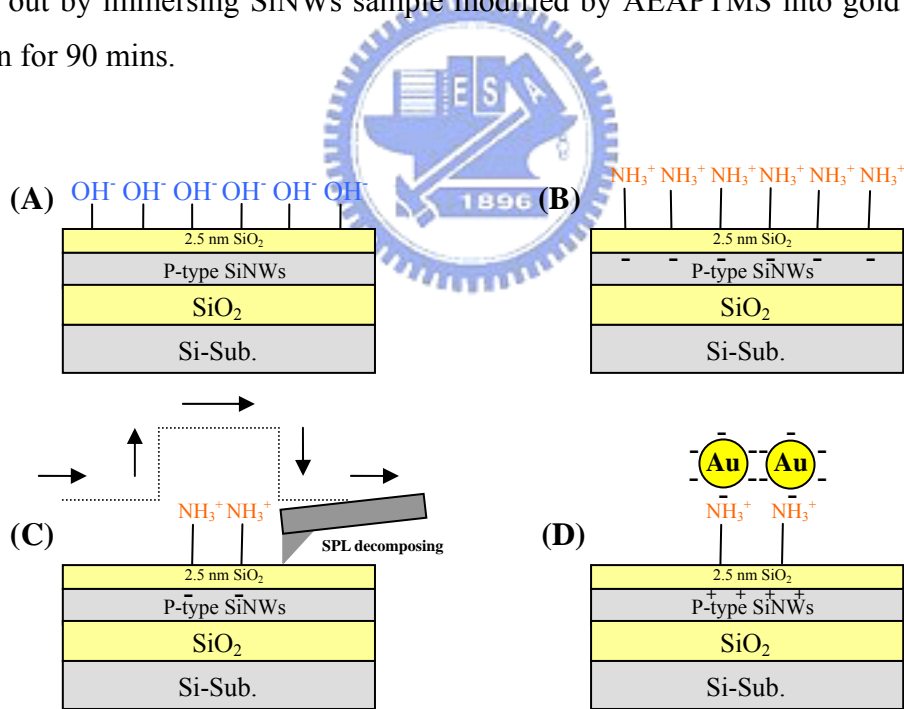


**Figure 4.19** Schematic of different chemical molecular modifications of channel surface states of the p-type silicon nanowires devices at room temperature. (A) OH<sup>-</sup>-gated modification, (B) NH<sub>3</sub><sup>+</sup>-gated modification, (C) SPL decomposed amino bonds, (D) AuNPs with citrate ions (COO<sup>-</sup>) modification.

### 4.7.2 Electrical characteristic analysis of various modified p-SiNWs

After various chemical modification processes, a clearly change in electrical conductance of the p-type Si nanowires devices can be determined by I-V measurement. The electrical property data are shown in Figure 4.20. It shows the electrical characteristic analysis of different chemical molecular modifications of channel surface states of the p-type SiNWs devices at room temperature. The significant changed in the electrical conductance of p-type SiNWs devices have clear different with varies of the chemical modifications on the channel surface of p-type SiNWs which are due to surface-state changed of the channel surface.

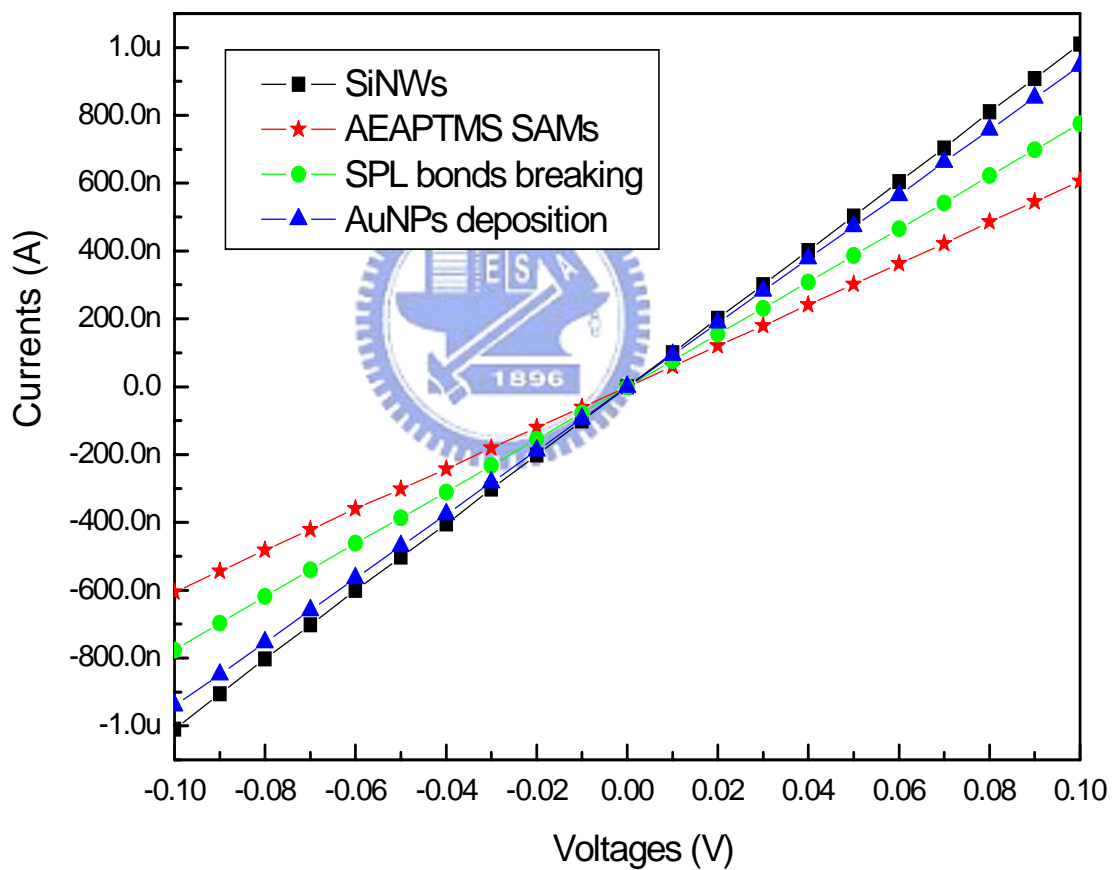


**Figure 4.20** Electrical properties ( $I_{DS}$ - $V_{DS}$ ) analysis of p-type silicon nanowires devices with different chemical molecular modifications capping at room temperature. The turn-on voltage and electrical conductance of p-type SiNWs devices have clear different with varies of the chemical modifications on the channel surface of p-type SiNWs.

For the positively gated channel by amine ( $\text{NH}_3^+$ ), it was found that AEAPTMS modifications of channel surface state of p-type SiNWs which changed the surface potential of p-type Si nanowires from negative to positive and resulted in the electrical conductance of SiNWs device moved from 10.9  $\mu\text{S}$  to 6.6  $\mu\text{S}$ , like a positive bias on the gate, as shown in Figure 4.20. (Red star “★”) Aminosilane modifications serves as a positive gate to the p-type Si channel, which depletes holes in the p-channel of SiNWs devices caused the electrical conductance decreased (decreased : 4300 nS).

SPL bond breaking effect on amino-functional silanation modified  $\text{SiO}_2$  surfaces of SiNWs was successfully demonstrated. The electronic characteristic of the p-SiNWs device after SPL field-induced decomposed chemical bonds on amino-functional silanation modified  $\text{SiO}_2$  surfaces of SiNWs is also depicted in Figure 4.20. SPL field-induced bond breaking modify the quantity of AEAPTMS on p-type Si nanowire which reduce AEAPTMS depletion effect in p-channel (increased : 1800 nS) and resulted in the electrical conductance of SiNWs device increased from 6.6  $\mu\text{S}$  to 8.4  $\mu\text{S}$ , as shown in Figure 4.20. (Green circle “●”)

After SPL bond breaking of AEAPTMS, gold nanoparticles (AuNPs) were selectively anchored on the desired unexposed region. Negatively charged gold nanoparticles interacted with amine of AEAPTMS molecules electrostatically and served as a negative chemical gate to p-channel of SiNWs. For the negatively gated channel by gold nanoparticles with citrate ions ( $\text{COO}^-$ ), it was found that gold nanoparticles modifications of channel surface state of p-type SiNWs which changed the surface potential of p-SiNWs and accumulated holes in p-channel of SiNWs. The increased significantly in conductance of the p-type SiNWs upon AuNPs attachment simply is an electrostatic gating effect by AuNPs modifications on the amino-terminal surface, and resulted in the electrical conductance of SiNWs device increased from 8.4  $\mu\text{S}$  to 9.6  $\mu\text{S}$ , as shown in Figure 4.20. (Blue triangle “▲”)

Figure 4.21 show that the schematic of band diagrams of hydroxyl-terminal of p-type Si channel gated by (a) amine ( $\text{NH}_3^+$ ) of AEAPTMS, (b) amino chemical bonds decomposed, and (c) gold nanoparticles selective deposition, respectively. It was suggested that amine ( $\text{NH}_3^+$ ) of AEAPTMS serves as a positive gate to the p-channel of SiNWs, which depleted holes in p-channel of SiNWs. Next, SPL field-induced bond breaking

modify the quantity of AEAPTMS on p-type Si nanowire which reduce AEAPTMS depletion effect in p-channel. Gold nanoparticles with citrate ions ( $\text{COO}^-$ ) serve as a negative gate to the p-channel of SiNWs, which accumulate holes in p-type Si channel.

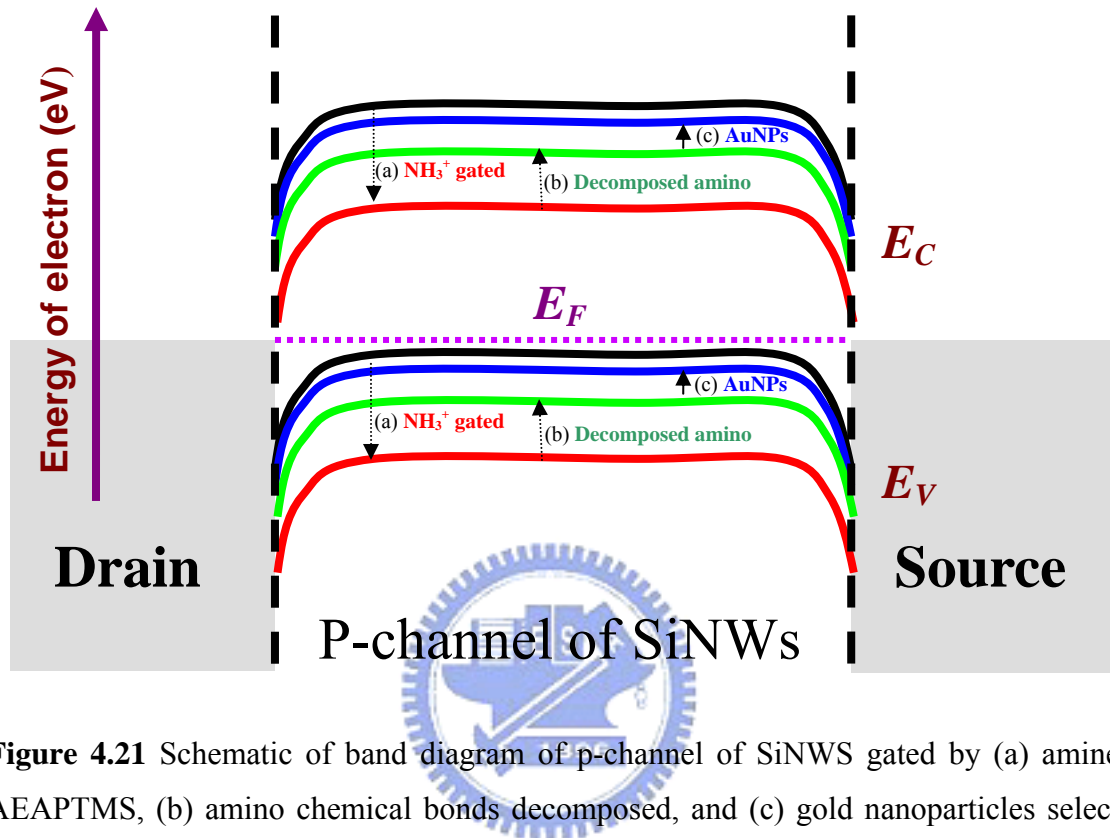


**Figure 4.21** Schematic of band diagram of p-channel of SiNWS gated by (a) amine of AEAPTMS, (b) amino chemical bonds decomposed, and (c) gold nanoparticles selective deposition, respectively. Amine of AEAPTMS serves as a positive gate to the Si channel, which depletes holes in p-channel of SiNWs. SPL field-induced bond breaking modify the quantity of AEAPTMS on p-type Si nanowire which reduce AEAPTMS depletion effect in p-channel. Gold nanoparticles with citrate ions serve as a negative gate to the p-channel of SiNWs, which accumulate holes in p-type Si channel.

Surface state potential of p-channel of SiNWs device was altered by chemicals with different types of electric charge polarity. Electrical conductance measurements also demonstrated expressly that the silicon nanowires can be detected with a very high sensitivity. Chemical modifications of channel surface gating for SiNWs devices were demonstrated successfully by modifying the p-channel surface state of SiNWs devices with AEAPTMS modified process, SPL decomposed amino bonds process, and gold nanoparticles selective deposition process, respectively. It was suggested that via scaling

down the diameter of p-channel of SiNWs, the silicon nanowire sensing with a higher sensibility on surface modification can be achieved. It was believed that the proposed novel surface modifications of channel of silicon nanowires devices can be widely applied in chemical / bio-sensors and nanoelectronics.

#### **4.8 Photoresponse of surface plasmon resonance of SiNWs with desired gold nanoparticles**

Surface plasmon resonance (SPR) effect is acknowledged arises from collective oscillations of free electrons at metallic surfaces. The binding of specific molecules onto the surfaces of metallic films or nanoparticles can cause a change in the surface plasmon resonance. The surface plasmon resonance (SPR) excited in metallic nanoparticles exhibits selective photoabsorption, scattering, and local electromagnetic field enhancement. In recent years, the surface plasmon resonance effect has demonstrated to be an excellent and a very powerful technique for real-time study of an optical properties sensing, bio-chemical sensing, and geometry of nanoparticles and intensively applied into practice, and more generally, for understanding molecular interactions and kinetics [28-32]. Interesting in the novel SPR techniques have been driven by the large number of potential applications and used widely in sensing biomolecular interactions with the surfaces of metallic substrates, ultrafast optical switches, surface enhanced spectroscopies, bio-chemical sensors, etc.

In this section 4.8, we will study and discuss forward taht a novel approach for nano-fabricating the desired and controllable gold nanoparticles selective deposition anchored onto the p-channel surface of silicon nanowire with the surface plasmon resonance-enhanced photosensitive conductivity behaviour therein. The tuning wavelength of the peak absorption attributed to SPR is highly desirable in the applications of the gold nanoparticles. Since the wavelength of the peak absorption of gold nanoparticles attributed to SPR depends on their particle size, particle shape, particle-to-particle distance, and surrounding dielectric medium. The gold nanoparticles reveal a pronounced SPR broad absorption band around 520 nm is well-known. In this research, the tuning wavelength of the observed surface plasmon resonance absorption band from the visible regions (blue: 420 nm) to near-infrared regions (infrared: 820 nm) has been achieved by using the



monochromator, indicating the change of electrical conductance of gold nanoparticles in the p-channel SiO<sub>2</sub> surface. It is believed that further improvements of the availability of SPR devices could come from the development of more compact systems with stable, inexpensive and disposable bio-sensors.

#### 4.8.1 Physical principles of surface plasmon resonance

In optics and physics, **Snell's law** which also known as the **law of refraction**, is a formula used to describe the relationship between the angles of incidence and refraction, when referring to light or other waves, passing through a boundary between two different isotropic media. The law says that the ratio of the sines of the angles of incidence and of refraction is a constant that depends on the media. When a beam of monochromatic polarized light passes from material with a high refractive index (e.g. glass prism SiO<sub>2</sub>) into material with a low refractive index (e.g. water), some light is reflected from the material interface. When the angle of incidence at which the light strikes the interface is greater than the critical angle ( $\theta_c$ ), the polarized light is completely reflected (total internal reflection). Metal is a plasmon system which is composed of free electron and immobile positive ion lattices. However, if the surface of the glass is coated with a thin film of a noble metal (e.g. gold), this reflection is not total; some of the light is lost into the metal surface as shown in Figure 4.22. There then exists a second angle greater than the critical angle ( $\theta_c$ ) at which this loss is greatest and at which the intensity of reflected light reaches a minimum. This angle is called the surface plasmon resonance angle ( $\theta_{SPR}$ ). During the surface plasmon resonance, the surface potential of the metal surface can be expressed by surface charge  $\sigma_{k\omega}$  as follows:

$$V_{k\omega}(r, t) = \frac{2\pi\sigma_{k\omega}}{k} e^{-k|z|} e^{i(kx - \omega t)} \dots\dots\dots (4.1)$$

Where  $\omega$  is the circular frequency of the incident light,  $\sigma_{k\omega}$  is the surface charge of the metal surface, and  $k$  is the wave vector of the incident photon. And the boundary condition of the material interface can be presented as follows:

$$\epsilon_1(\omega)E_z(z = 0^+, \omega) = \epsilon_2(\omega)E_z(z = 0^-, \omega) \dots\dots\dots (4.2)$$

Via the continuous equations, we can obtain a relationship equations:

$$E_z(z = 0^+, \omega) = -E_z(z = 0^-, \omega) \dots\dots\dots (4.3)$$

Then, the surface plasmon resonance condition can be expressed as following equation:

$$\varepsilon_1(\omega) = -\varepsilon_2(\omega) \dots\dots\dots (4.4)$$

It is a consequence of the oscillation of mobile electrons (or called plasma) at the surface of the metal film. These oscillating plasma waves are called surface plasmons. When the wave vector of the incident light matches the wavelength of the surface plasmons, the electrons resonated, hence the term surface plasmon resonance. Then, the coupling of the incident light to the surface plasmons results in a loss of energy and therefore a reduction in the intensity of the reflected light. For gold nanoparticles case, it was observed that revealed a pronounced SPR broad absorption band around 520 nm by the reflection detector measurement.

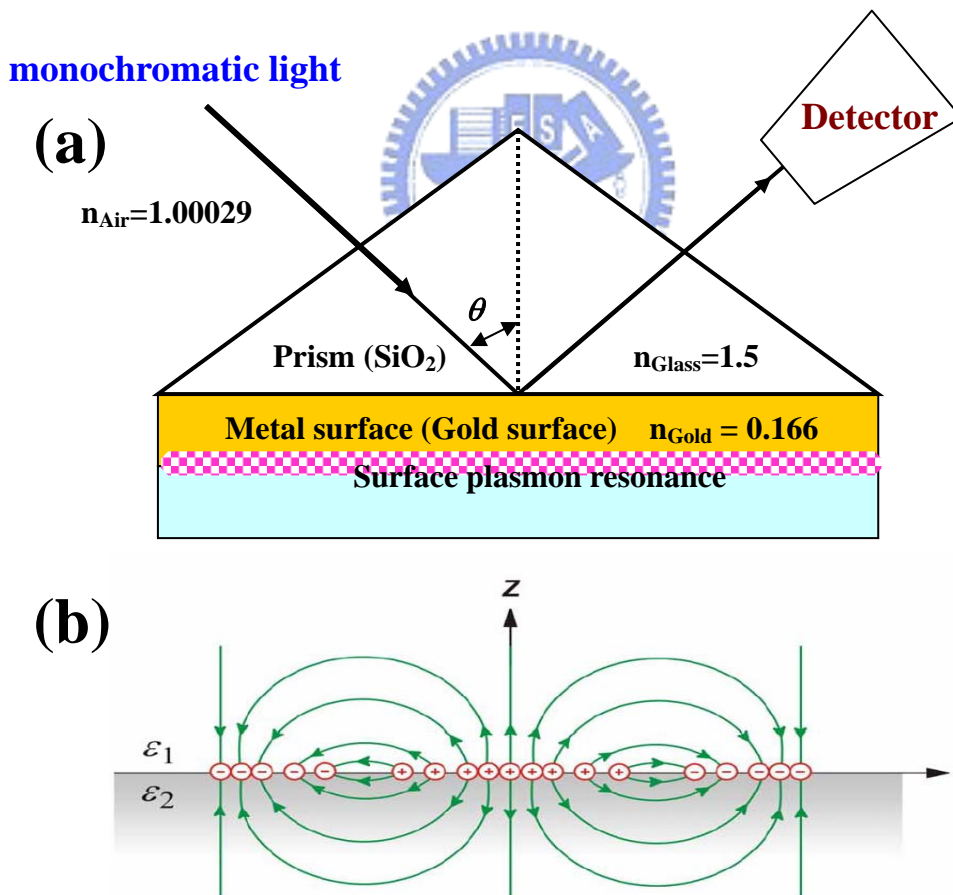


**Figure 4.22** (a) Schematic diagrams of the surface plasmons resonance devices enhanced by gold metal surface. (b) Charge distribution for dipole-dipole coupling resonance.

#### 4.8.2 Small amount of gold nanoparticles was controllable to selective anchored on the desired p-channel surface of SiNWs devices

SPL bond breaking nanolithography owns a lot of potential as a powerful tool in nanofabrication. SPL bond breaking utilizes a conductive tip to pattern / decompose the aminosilane modification SiO<sub>2</sub> surface of substrate. In this section 4.8.2, silicon nanowire device was fabricated for biological detection by E-beam lithography on (100)-oriented p-type SOI wafer and the hydroxyl-terminal surface of SiNW is further modified by silanization procedure. SPL bond breaking effect on amino-functional silanation modified SiO<sub>2</sub> surfaces of p-channel of SiNWs was successfully demonstrated. After SPL bond breaking of AEAPTMS, the small amount of gold nanoparticles are successfully controlled and selectively anchored on the small SPL unexposed region of SiO<sub>2</sub> surfaces of p-channel of SiNWs devices.

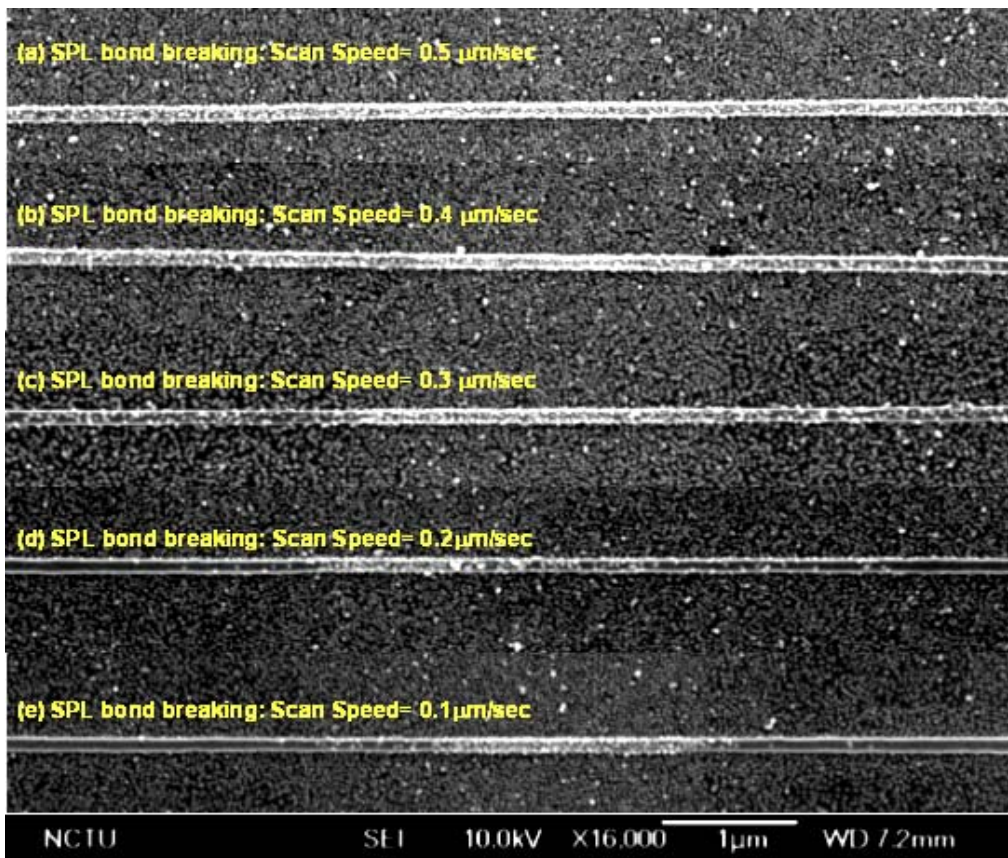


**Figure 4.23** Decomposed efficiency of SPL bond breaking on the p-channel SiO<sub>2</sub> of SiNWs devices at a tip scanning speed from 0.5  $\mu\text{m}/\text{sec}$  to 0.1  $\mu\text{m}/\text{sec}$ . Tip bias, set point, and ambient humidity was maintained on -10 V, 0.5 V, and  $60 \pm 1\%$ , respectively.

Figure 4.23 shows the decomposed efficiency of SPL bond breaking on the p-channel SiO<sub>2</sub> of SiNWs devices at a tip scanning speed from 0.5 μm/sec to 0.1 μm/sec. The tip decomposed bias, set point, and ambient humidity was maintained on -10 V, 0.5 V, and 60 ±1%, respectively.

It was observed clearly that AuNPs selective deposition of SPL bond breaking patterns decreased with the SPL bond breaking reaction time increased. From this result, we can found that the SPL decomposing efficiently at the lower tip scanning speed 0.1 μm/sec condition. This phenomenon was indicated that the SPL electric field-induced decomposing there's not enough time to induce decompose the aminosilane modification surface efficiently as operated at higher tip scanning speed.

Devices base on SiNWs are emerging as a powerful tools for bio-sensing that enable direct sensing electron variation in channel. Figure 4.24 shows that the SEM images of the small amount of gold nanoparticles are successfully controlled and selectively anchored on the SPL unexposed small region of SiO<sub>2</sub> surfaces of p-channel of SiNWs devices. 15nm-gold nanoparticles on the desired small region outside the SPL bond breaking patterns on the p-channel surface of SiNWs devices are clearly observed. And, no gold nanoparticles is found at the remainder SPL bonds breaking patterns on the p-channel surface showing that gold nanoparticles selectively deposited only on the SPL undecomposed patterning region. SPL bond breaking modify the quantity of AEAPTMS on nanowire which reduce AEAPTMS depletion effect in channel. Furthermore, local AuNPs with citrate ions modification on nanowire accumulate the channel due to local surface electric confinement also demonstrated. When the AuNPs anchored on the SiNW surface, the AuNPs act as negative gates, holes accumulation on the SiNW is expected to cause an increase in the electrical conductance to the p-type SiNW due to negative citrate ion on the AuNPs surface. Finally, SPL bond breaking technique is provide a pathway to modify surface to link different functional group, enabling diverse and exciting application in bio-sensing technology and nanoelectronics. Then, we can utilize the SPL bond breaking technique with gold nanoparticles self-assembly method to selective anchor of 15 nm AuNPs on p-channel surface of SiNWs down to few gold particles, and we also can research and develop about the photosensitive characteristics of gold nanoparticles selective anchored on p-channel surface of SiNWs by this novel technique.

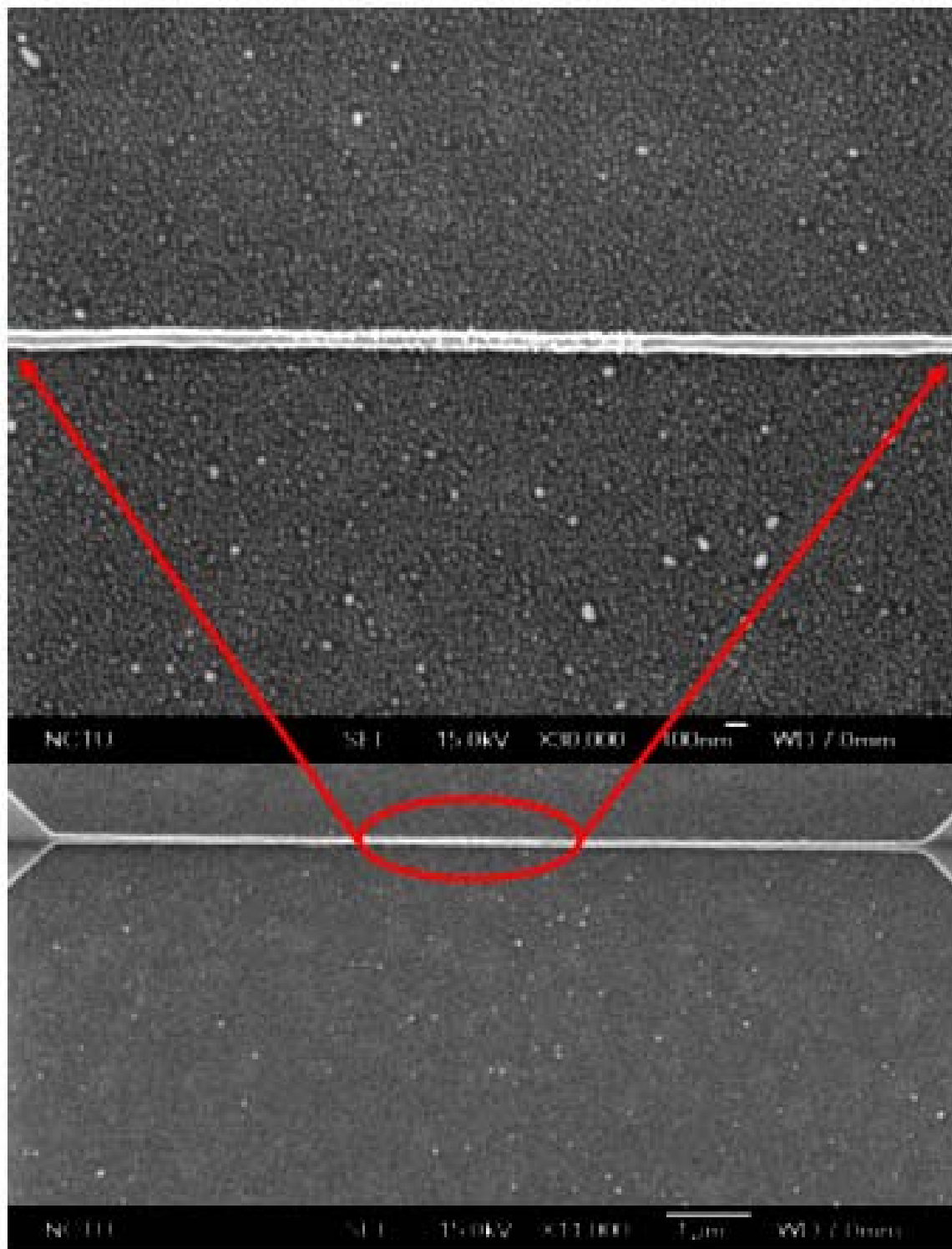


**Figure 4.24** SEM images of gold nanoparticles selective deposition on the SPL unexposed silanation modification regions of (100) p-type silicon nanowires (SiNWs) devices. Nanowire is about 100 nm wide and 10  $\mu$ m long. Inset shows the details of the small amount of gold nanoparticles are successfully controlled and selectively anchored on the small SPL unexposed region of SiO<sub>2</sub> surfaces of p-channel of SiNWs devices.

### 4.8.3 Surface plasmon resonance enhanced the photoconductivity of the p-channel of SiNWs with few amounts of AuNPs

In this section 4.8.3, we will present the use of SPL bond breaking technique to fabricate a small amount of self-assembly photosensitive gold nanoparticles selective anchored on to p-channel surface of silicon nanowire devices. Before the gold nanoparticles selective deposition process, the electrical conductive characteristics of p-type bare SiNWs without AuNPs capping and without any irradiation process at room temperature with sweep of source-drain ( $V_{ds}$ ) bias 10 mV as shown in Figure 4.25. It was found clearly that the conductance was about  $9.62 \mu\text{S}$ .

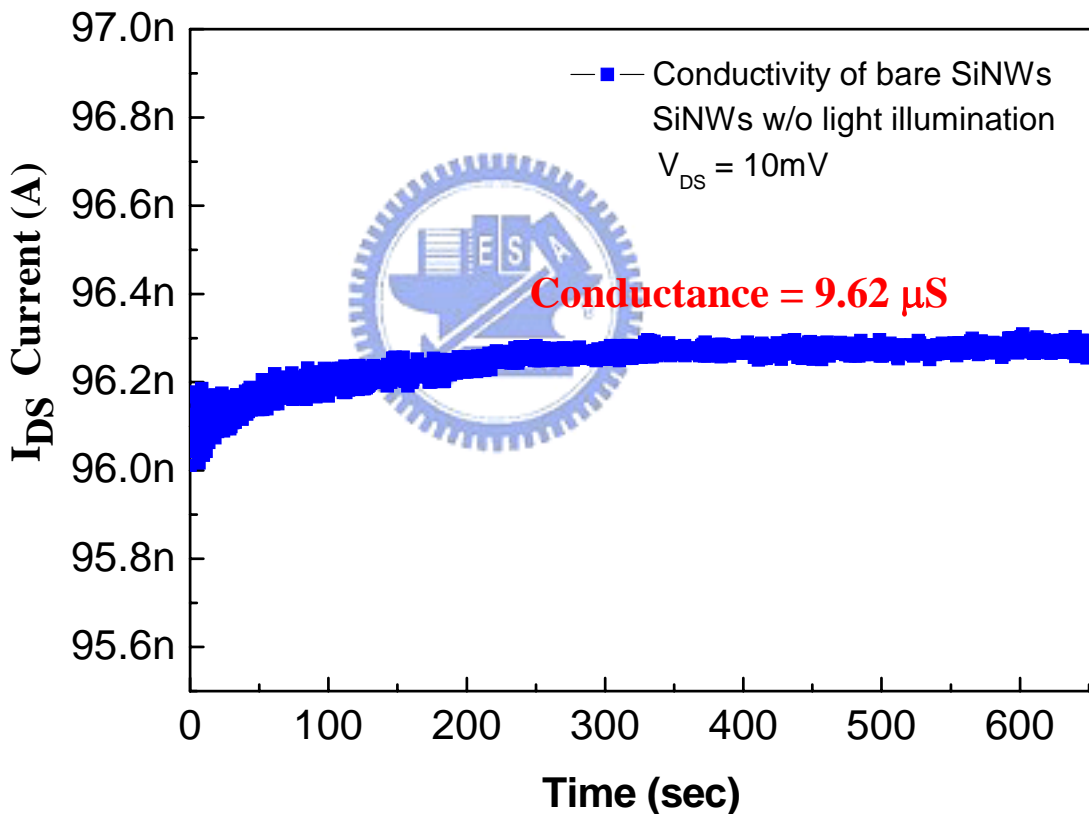


**Figure 4.25** Electrical conductive properties ( $I$ - $V_{ds}$ ) of bare SiNWs without AuNPs capping and without any irradiation process at room temperature with sweep of source-drain ( $V_{ds}$ ) bias 10 mV. It was found that the conductance was about  $9.62 \mu\text{S}$ .

Such the p-type silicon nanowire with few photosensitive gold nanoparticles shows outstanding surface plasmon resonance absorption and following enhanced the photo-

conductivity of the Si-nanowire devices. The schematic diagram of the photoconductivity enhanced on the few AuNPs of p-channel surface of SiNWs devices by surface plasmon resonance effect was shown in the Figure 4.26.

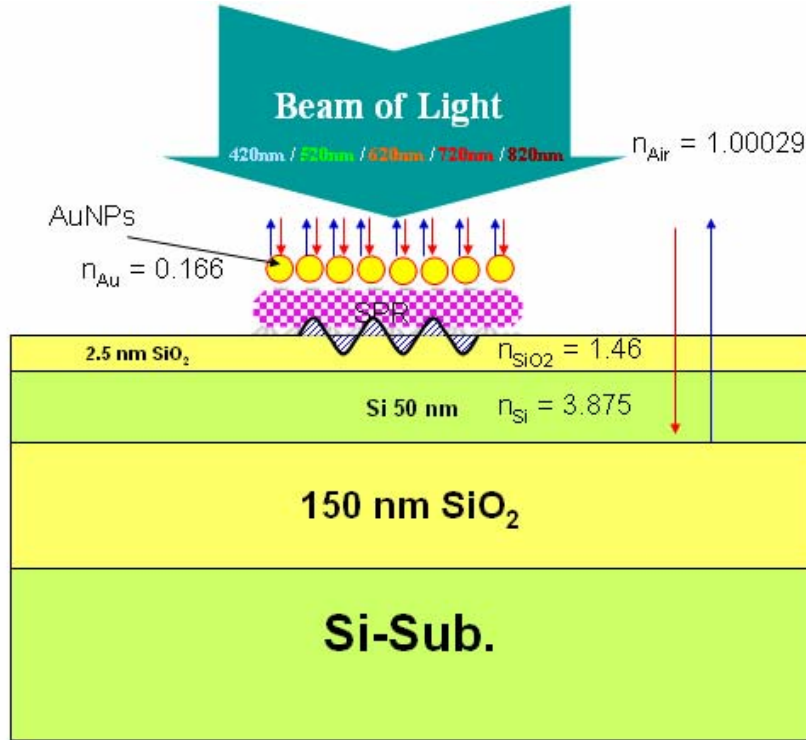


**Figure 4.26** Schematic diagrams of photoconductivity enhanced on the few AuNPs of p-channel surface of SiNWs devices by surface plasmon resonance effect.

In this photoresponse measurement section, the equipments of measuring the photoconductivity characteristics of p-type silicon nanowire devices used by Agilent 4155 semiconductor parameter analyzer. The silicon nanowire devices were fabricated from the p-type doped silicon (100)-SOI wafer. The carrier density of silicon nanowire was equal to the doping concentration of  $5 \times 10^{19}$  atoms/cm<sup>3</sup>. The current value of theory is about 106.8 nA with  $V_{DS} = 10$  mV, length = 10  $\mu$ m,  $\mu_p = 53.4$  cm<sup>2</sup>/v.s, and cross-section area of nanowire was  $2.5 \times 10^{-13}$  cm<sup>2</sup>. The experiment result was 100 nA, which was close to theoretical value, as shown in Figure 4.20. After various chemical modification processes, a clearly change in electrical conductance of the p-type Si nanowires devices can be determined. The voltage of the d.c. source was maintained at 10 mV and the current was measured by a Agilent 4155 semiconductor parameter analyzer. In this study, the tuning wavelength of photoresponse measurements from the visible regions (420 nm) to

near-infrared regions (820 nm) by using the monochromator, and the p-channel surface of SiNWs devices with few AuNPs were conducted under alternate light illumination (light on-state) of different wavelengths and under dark conditions (light off-state). Figure 4.27 shows that the photoconductive properties of p-type bare SiNWs without any AuNPs capping at five different light wavelength irradiation processes at room temperature with sweep of source-drain ( $V_{ds}$ ) bias 10 mV. It was observed that the photoconductive current increased 0.2 nA ~ 0.4 nA. It was suggested that photons of light are absorbed in the silicon nanowire and the photo-electric effect produces electron-hole pairs caused electrons raised from the valence band into the conduction band and photoconductive current increased.

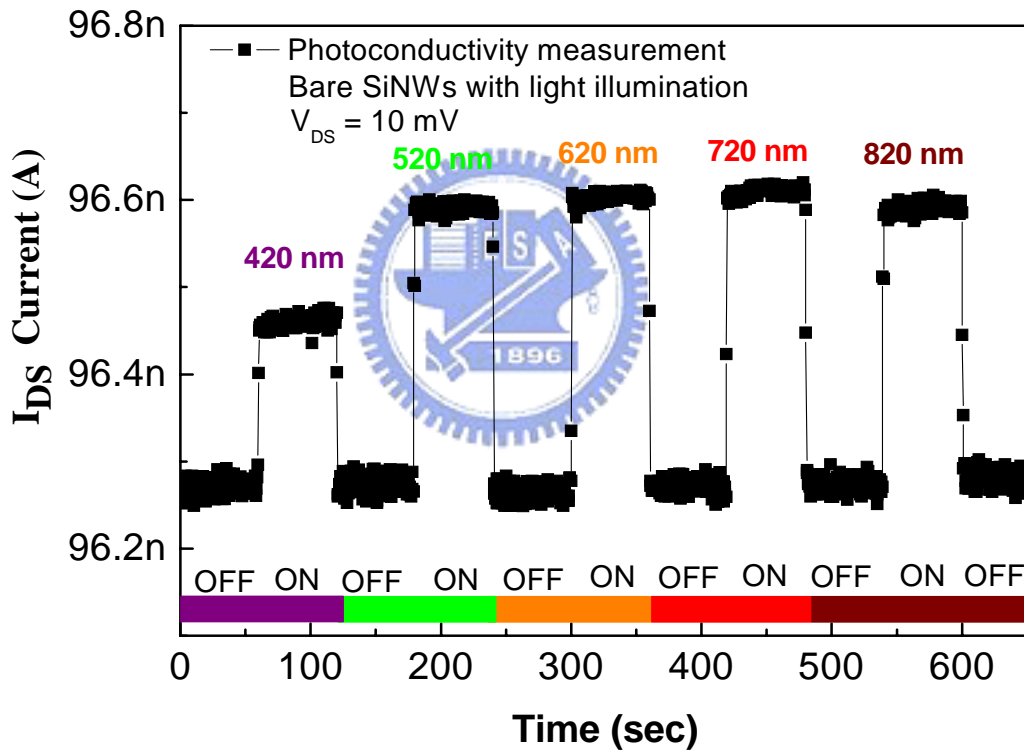


**Figure 4.27** Photoconductive characteristics of p-type bare SiNWs without any AuNPs capping at five different light wavelength irradiation processes at room temperature with sweep of source-drain ( $V_{ds}$ ) bias 10 mV.

After gold nanoparticles selective deposition process, the electrical conductive properties ( $I-V_{ds}$ ) of p-type SiNWs with AuNPs capping at five different light wavelength irradiation processes at room temperature with sweep of source-drain ( $V_{ds}$ ) bias 10 mV as



shown in the Figure 4.28. More interestingly, it was found that noticeable response at wavelength of 520nm and wavelength of 720 nm, respectively, which presents a wavelength-dependent photoresponse in resistance. From the Figure 4.28 compared result, it was found that the photoconductivity is enhanced by surface plasmon resonance, so we must subtract the photoconductivity increase on bare silicon nanowire devices.

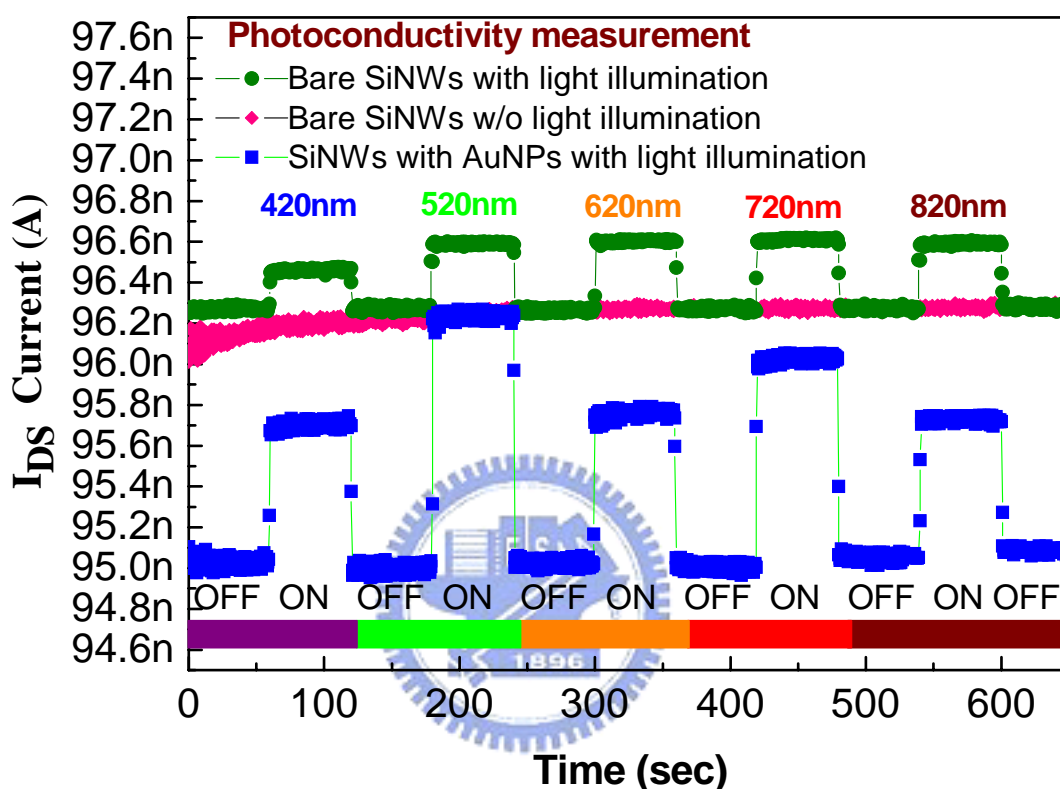


**Figure 4.28** Various photoconductivity characteristic measurements of p-type silicon nanowires devices. Photoconductivity is enhanced by surface plasmon resonance. After AuNPs selective deposition process, it was found that noticeable response at wavelength of 520 nm and wavelength of 720 nm, respectively.

Surface plasmon resonance characteristics of p-type SiNWs with AuNPs capping at five different light wavelength irradiation processes with sweep of source-drain bias 10 mV as shown in the Figure 4.29. It was observed clearly that the photoconductivity behaviour at a surface plasmon resonance wavelength of 520 nm shows a larger difference in resistance between the illumination on and off conditions. The resistance change from 105.22 K $\Omega$  (light off-state) to 104.24 K $\Omega$  (light on-state) that observed using 520 nm light. The

decreased resistance change is nearly 590  $\Omega$  and 480  $\Omega$  that observed using 420 nm light and 620 nm light, respectively. Furthermore, it was also found clearly that the photoconductivity behaviour at the wavelength of 720 nm between the illumination on and off conditions which was suggested that caused by the photo absorption effect of gold-clusters aggregation on the SiO<sub>2</sub> modification surface of SiNWs. In this SPR study, room-temperature photoconductivity responses as a function of time to light illumination for the p-channel surface of SiNWs with few AuNPs selective deposition. We believed that further improvements of the availability of SPR devices could apply ble to both nanoelectronics and nanobiosensors.

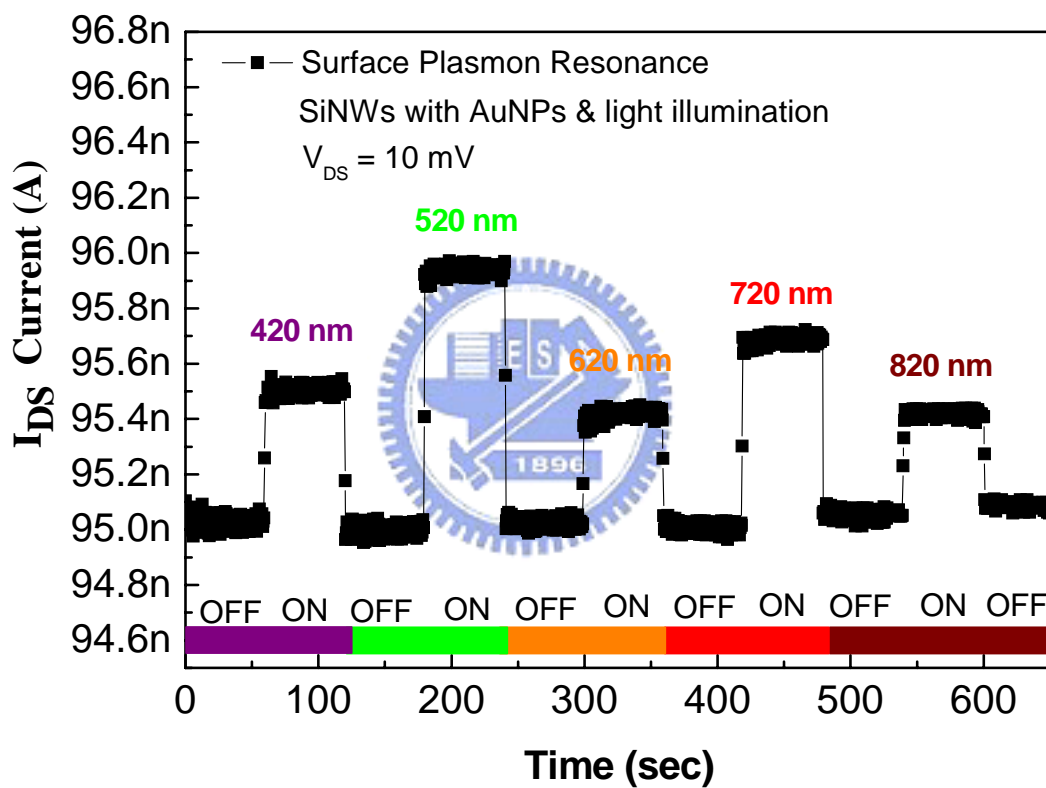


**Figure 4.29** Photoresponse measurements. The surface plasmon resonance characteristics of p-type SiNWs with AuNPs capping at five different light wavelength irradiation processes at 300K with sweep of source-drain ( $V_{ds}$ ) bias 10 mV.

## 4.9 Conclusions

A new approach has successfully demonstrated for the facile patternwise deposition of AuNPs onto a SiO<sub>2</sub> surface with nanometer scale resolution by SPL field-induced bond breaking of AEAPTMS SAMs. The bond breaking effect of AEAPTMS SAMs was conducted by SPL with tip / sample bias 4.0 ~ 6.5 volts on the 2.5 nm thick SiO<sub>2</sub> surface. When tip / sample bias less than 5.0 volts, results exhibit no effective decomposition of AEAPTMS SAMs through the observations of anchoring of AuNPs and the XPS characterization of nitrogen N1s on the unexposed regions.

Also, the bond breaking of AEAPTMS SAMs was realizable with tip/sample bias less than 10 volts for the SiO<sub>2</sub> thickness up to 8 nm in tip scanning speed lower than 0.2 μm/sec. Efficiency of AEAPTMS SAMs bond breaking is limited by the tunneling current, and tip scanning speed is also crucial. The proposed nanofabrication technique works like a negative-tone patterning approach which is capable of binding negative charged nanoparticles or quantum dots.

Distribution densities of gold nanoparticles selective deposition were successfully dominated by using SPL electrical-field-induced chemical bond decomposing technique. It was found that distribution densities of the gold nanoparticles selective deposition on the SPL bond breaking exposed patterns as a function of the bond breaking voltages is decreased exponentially, and it is believed that the proposed novel technique can be applicable to generate interesting gray-level selective patterning.

Furthermore, novel technique has successfully demonstrated for the facile patternwise deposition of AuNPs onto a SiO<sub>2</sub> surface with nanometer scale resolution by SPL field-induced bond breaking of AEAPTMS SAMs. Surface state potential of p-channel of SiNWs device was altered by chemicals with different types of electric charge polarity and can be detected with a very high sensitivity. And it was found clearly that the photoconductivity behaviour at a surface plasmon resonance (SPR) wavelength of 520 nm, and room-temperature photoconductivity responses as a function of time to light illumination for the p-channel surface of SiNWs with few AuNPs selective deposition. We believed that the proposed novel surface modifications of channel of silicon nanowires devices can be widely applied in SPR devices, chemical bio-sensors and nanoelectronics.

## Reference

- [1] A. I. Hochbaum, R. Fan, R. He, P. Yang, “Controlled Growth of Si Nanowire Arrays for Device Integration”, *Nano Lett.* **5**, pp. 457-460, 2005.
- [2] W. P. Wuelfing, R. W. Murray, “Electron Hopping through Films of Arenethiolate Monolayer-Protected Gold Clusters”, *J. Phys. Chem. B* **106**, pp. 3139-3145, 2002.
- [3] S. A. Maier, P. G. Kik, H. A. Atwater, S. Meltzer, E. Harel, B. E. Koel, A. A. G. Requicha, “Local detection of electromagnetic energy transport below the diffraction limit in metal nanoparticle plasmon waveguides”, *Nat. Mater.* **2**, pp. 229-232, 2003.
- [4] J. F. Hicks, F. P. Zamborini, A. J. Osisek, R. W. Murray, “The Dynamics of Electron Self-Exchange between Nanoparticles”, *J. Am. Chem. Soc.* **123**(29) pp. 7048-7053, 2001.
- [5] C. K. Harnett, K. M. Satyalakshmi, and H. G. Craighead, “Low-energy electron-beam patterning of amine-functionalized self-assembled monolayers”, *Appl. Phys. Lett.* **76**(17), pp. 2466-2468, 2000.
- [6] J. L. Plaza, Y. Chen, S. Jacke, R. E. Palmer, “Nanoparticle Arrays Patterned by Electron-Beam Writing: Structure, Composition, and Electrical Properties”, *Langmuir* **21**(4), pp. 1556-1559, 2005.
- [7] Ki-Bum Lee, Jung-Hyurk Lim, and Chad A. Mirkin, “Protein Nanostructures Formed via Direct-Write Dip-Pen Nanolithography”, *J. Am. Chem. Soc.* **125**, pp. 5588-5589, 2003.
- [8] C. -F. Chen, S. -D. Tzeng, M. -H. Lin, and S. Gwo, “Electrostatic Assembly of Gold Colloidal Nanoparticles on Organosilane Monolayers Patterned by Microcontact Electrochemical Conversion”, *Langmuir* **22** (18) 7819-7824, 2006.
- [9] S. Liu, R. Maoz, J. Sagiv, “Planned Nanostructures of Colloidal Gold via Self-Assembly on Hierarchically Assembled Organic Bilayer Template Patterns with In-situ Generated Terminal Amino Functionality”, *Nano Lett.* **4** (5), pp. 845-851, 2004.
- [10] X. Ling, X. Zhu, J. Zhang, T. Zhu, M. Liu, L. Tong, Z. Liu, “Reproducible Patterning of Single Au Nanoparticles on Silicon Substrates by Scanning Probe Oxidation and Self-Assembly”, *J. Phys. Chem. B* **109**(7), pp. 2657-2665, 2005.

- [11] G.-Y. Liu, S. Xu, and Y. Qian, "Nanofabrication of Self-Assembled Monolayers Using Scanning Probe Lithography", *Acc. Chem. Res.* **33** (7), pp. 457-466, 2000.
- [12] E. S. Snow, P. M. Campbell, "Fabrication of Si nanostructures with an atomic force microscope", *Appl. Phys. Lett.* **64**(15), pp. 1932-1934, 1994.
- [13] E. S. Snow, P. M. Campbell, "AFM Fabrication of Sub-10 Nanometer Metal Oxide Devices with in Situ Control of Electrical Properties", *Science* **270**(5242), pp. 1639-1641, 1995.
- [14] F. S. -S. Chien, C.-L. Wu, Y. -C. Chou, T. T. Chen, S. Gwo, and W. -F. Hsieh, "Nanomachining of (110)-oriented silicon by scanning probe lithography and anisotropic wet etching", *Appl. Phys. Lett.* **75**(6), pp. 2429-2431, 1999.
- [15] T. Yoshinobu, J. Suzuki, H. Kurooka, W. C. Moon, H. Iwasaki, "AFM fabrication of oxide patterns and immobilization of biomolecules on Si surface", *Electrochimica Acta* **48**, pp. 3131-3135, 2003.
- [16] A. Ulman, "Formation and Structure of Self-Assembled Monolayers", *Chem. Rev.* **96**(4), pp. 1533-1554, 1996.
- [17] H. -Z. Yu, A. W. Rowe, D. M. Waugh, "Templated Electrochemical Deposition of Zirconia Thin Films on "Recordable CDs" ", *Anal. Chem.* **74**(22), pp. 5742-5747, 2002.
- [18] H. Sugimura, N. Nakagiri, "Nanoscopic Surface Architecture Based on Scanning Probe Electrochemistry and Molecular Self-Assembly", *J. Am. Chem. Soc.* **119**(39), pp. 9226-9229, 1997.
- [19] Y. Masuda, M. Itoh, T. Yonezawa, K. Koumoto, "Low-Dimensional Arrangement of SiO<sub>2</sub> Particles", *Langmuir* **18**(10), pp. 4155-4159, 2002.
- [20] D. Wouters, U. S. Schubert, "Constructive Nanolithography and Nanochemistry: Local Probe Oxidation and Chemical Modification", *Langmuir* **19**(21), pp. 9033-9038, 2003.
- [21] Q. Li, J. Zheng, Z. Liu, "Site-Selective Assemblies of Gold Nanoparticles on an AFM Tip-Defined Silicon Template", *Langmuir* **19**(1), pp. 166-171, 2003.
- [22] S. Hoepfner, R. Maoz, S. R. Cohen, L. Chi, H. Fuchs, J. Sagiv, "Metal Nanoparticles, Nanowires, and Contact Electrodes Self-Assembled on Patterned Monolayer Template- A Bottom-up Chemical Approach", *Adv. Mater.* **14** (15), pp. 1036-1041, 2002.

- [23] R. Martel, Ph. Avouris, I. -W. Lyo, "Molecularly Adsorbed Oxygen Species on Si(111)- (7×7): STM-Induced Dissociative Attachment Studies", *Science* **272**(5260), pp. 385-388, 1996.
- [24] S. -W. Hla, G. Meyer, K. -H. Rieder, " Selective bond breaking of single iodobenzene molecules with a scanning tunneling microscope tip", *Chem. Phys. Lett.* **370**, pp. 431-436, 2003.
- [25] R. P. Gupta, "Electronic structure crystalline and amorphous silicon dioxide", *Phys. Rev. B* **32** (12), pp. 8278-8292, 1985.
- [26] G. Frens, "Controlled nucleation for the regulation of the particle size in monodisperse gold solutions", *Nature*, **241**, pp.20-22, 1973.
- [27] N. M. Ravindra and J. Zhao, "Fowler-Nordheim tunneling in thin SiO<sub>2</sub> films", *Smart Mater. Struct.* **1**, pp. 197-201, 1992.
- [28] N.Nath and A. Chilkoti, "Label-Free Biosensing by Surface Plasmon Resonance of Nanoparticles on Glass: Optimization of Nanoparticle Size", *Anal. Chem.* **76**, pp. 5370-5378, 2004.
- [29] I. Tokareva, S. Minko, J. H. Fendler, and E. Hutter, "Nanosensors Based on Responsive Polymer Brushes and Gold Nanoparticle Enhanced Transmission Surface Plasmon Resonance Spectroscopy", *J. Am. Chem. Soc.* **126**, 15950-15951, 2004.
- [30] S. Srivastava, B. L. Frankamp, and V. M. Rotello, "Controlled Plasmon Resonance of Gold Nanoparticles Self-Assembled with PAMAM Dendrimers", *Chem. Mater.***17**, pp.487-490, 2005.
- [31] H. -Y. Lin, C. -T. Chen, and Y. -C. Chen, "Detection of Phosphopeptides by Localized Surface Plasma Resonance of Titania-Coated Gold Nanoparticles Immobilized on Glass Substrates", *Anal. Chem.* **78**, pp.6873-6878, 2006.
- [32] G. M. Koenig Jr., M. -V. Meli, J. -S. Park, J. J. de Pablo, and N. L. Abbott, "Coupling of the Plasmon Resonances of Chemically Functionalized Gold Nanoparticles to Local Order in Thermotropic Liquid Crystals", *Chem. Mater.* **19**, pp.1053-1061, 2007.

## Chapter 5.

### Summary

In this thesis, the novel methods of directly defined nano-patterns on single-crystal silicon surface, and on silane-modifications surface of silicon substrate by using electric-field-enhanced local anodic surface oxidation with scanning probe microscopy (SPM) have been demonstrated. We have successfully demonstrated accurate linear control of nanostructures fabrication for different linewidth by using the multipixel scanning method of SPL technique with ODE etching process, and feature size of desired nanopattern down to 20 nm can be easily obtained under control. We have successfully demonstrated accurate linear control of nanostructures fabrication for different linewidth from 25 nm to 80 nm by SPL technique. It was indicated that the use of multipixel scanning method of SPL with more potential benefits to perform novel structures for fundamental studies of nanostructure, nano-patterning for linearity studies, and there is the possibility of using these techniques for device nanofabrication and nanoelectronics applications.

We have also successfully demonstrated that using DPN lithography to deposit 1 nm gold salt from an aqueous  $\text{HAuCl}_4$  ink solution onto a  $\text{SiO}_2$  / silicon nanowire induces reduction of the gold ions aggregated to gold nanoclusters by using the 365 nm UV light irradiation in air evidenced and subsequent nucleation to gold nano-clusters. It was found that the decrease in the binding energy and the changes in the width of the Au4f peak corresponding to  $\text{Au}^0$  and the growth of gold nanoclusters can be evidenced. Electrical characteristics demonstrated that the conductance of SiNW increased two times at 0.5 volts of  $V_{ds}$  after DPN of gold nanoclusters. DPN of gold nanoclusters on the oxide surface of silicon nanowires enhanced carriers transport in the channel of n-type silicon nanowires. In addition, DPN of AEAPTMS nanopatterns has also been demonstrated on the  $\text{SiO}_2$  surface. Linewidths down to 60 nm have been successfully produced. In this study, we have successfully deposited gold nanoparticles onto AEAPTMS nanopatterns modified by silanation on a hydroxyl-terminal  $\text{SiO}_2$  surface. The reducing the time of self-assembly in gold selective deposition may be necessary to reduce the distortion of AEAPTMS patterns and gold nanoparticles patterns.

Moreover, a novel approach has successfully demonstrated for the facile patternwise deposition of gold nanoparticles onto a SiO<sub>2</sub> surface with nanometer scale resolution by SPL field-induced bond breaking of AEAPTMS SAMs. The proposed nanofabrication technique works like a negative-tone patterning approach which is capable of binding negative charged nanoparticles or quantum dots. It was found that distribution densities of gold nanoparticles selective deposition were dominated by the additional SPL electrical-field-induced chemical bond decomposing effect. Distribution densities of the gold nanoparticles selective deposition on the SPL bond breaking exposed patterns as a function of the bond breaking voltages is decreased exponentially. It is believed that the proposed novel technique can be applicable to generate interesting gray-level selective patterning.

Furthermore, chemical modifications of channel surface gating effect of SiNWs devices were demonstrated successfully by modifying the surface states of p-channel of SiNWs devices. Surface state potential of p-channel of SiNWs device was altered by chemicals with different types of electric charge polarity, and can be detected with a very high sensitivity. And, it was found clearly that the photoconductivity behaviour at a surface plasmon resonance wavelength of 520 nm, and room-temperature photoconductivity responses as a function of time to light illumination for the p-channel surface of SiNWs with few AuNPs selective deposition. Because of their nature, gold nano-particles have been widely used for a variety of bio-medical applications. We believed that the proposed novel surface modifications of channel of silicon nanowires devices and SPL nanofabrication technique can be widely further applied in SPR devices, nanobiochemical sensors and nanoelectronics.



## 國立交通大學 電子物理研究所

姓 名：吳家豪

性 別：男

出生年月日：民國 62 年 9 月 4 日

籍 貫：台灣省雲林縣

地 址：雲林縣斗六市內環路 609 號

學歷：

畢業學校	學位	起 訖 年 月
國立交通大學 電子物理所	理學博士	91 年 9 月 ~ 96 年 6 月
國立雲林科技大學 電子所	工學碩士	86 年 9 月 ~ 88 年 6 月
私立大葉工學院 電機系	工學學士	83 年 9 月 ~ 86 年 6 月
正修工商專科學校 電子科	專士	78 年 9 月 ~ 83 年 6 月
雲林縣立斗六國民中學	中學	75 年 9 月 ~ 78 年 6 月

經歷：

服務單位	職位	起 訖 年 月
國家同步輻射研究中心	助理研究員	89 年 1 月 ~ 96 年 4 月
行政院同步輻射研究中心	研究助理	88 年 7 月 ~ 88 年 10 月
雲林科技大學電子工程所	研究助理	87 年 8 月 ~ 88 年 6 月
		年 月 ~ 年 月

# 自 傳

我叫吳家豪，出生於雲林縣斗六市，我是一個在淳樸鄉下長大的孩子，家中成員有父母親和一個哥哥和一個姐姐。雖然童年時代的物質生活較困乏，但父母親卻給了我豐足的精神生活！我們家中人口簡單家境小康，生活十分單純，父親已經從職場上退休，而母親則負責照料全家的生活所需。大哥是一位眼科驗光師，而二姐則是在雲林縣立文化局擔任舞台總監一職。家中的孩子總也不負父母的期望，在各自領域皆有優秀表現，所以我也期許自己能 and 他們一樣成為專業的人才。

父母對於我們孩子的教育是不留餘力的，對於小孩有興趣的事物會全力支持。從小我就對新奇的事物以及電子科技的產品有一定的興趣，喜歡享受學習科學的樂趣，因此我常夢想能成為與跟科技同步發展的專精科技人才。我的個性沈穩而內向，喜好旅遊、閱讀、攝影、園藝植栽等休閒活動。在求學的過程中，父母非常尊重我的想法，在興趣與學習合而為一的理念下，中學畢業後，我選擇了自己喜歡的正修電子工程科系來就讀，並在這個領域中發揮所長，並以第一名優異成績畢業。之後我插班大學念的也是大葉的電機工程學系，主要的學習項目也大部分集中在電子、半導體有關知識。由於個性使然，凡事都喜歡追根究底，因此，在學校時便朝向新知識喜歡學習研究新事物和挑戰不同領域的知識，因此每每有新的學習機會，我都會勇於學習與嘗試，並且從中學到不少的經驗，由於我個人在大學求學階段對於相關基礎科學與基礎理論的專業知識相當重視，也由於這樣的經驗，讓我在面對不同的工作環境與工作內容都可以在最短的時間內上手。在民國 86 年以全校第一名優異成績畢業，同年，我也榮獲了中國工程師學會頒發的『十大優秀工程學生獎』，以及國科會所頒發的『大專學生專題研究創作獎』。在研究所攻讀碩士學位期間受到學校創新的學習風氣、務

實的教學方法，以及老師們十分尊重學生們的思維想法，讓我在學生生涯中受益頗深，同時也讓我學會可以站在不同的角度去思考事情，這樣的訓練讓在往後自主及邏輯思考增益不少。

碩士畢業後，我選擇了國家同步輻射研究中心元件科技小組的國防訓儲的工作，跟隨許鈺宗教授從事奈米微結構製程研發已有八年以上的工作經驗，除了具備有半導體製程相關領域的專業知識外，本人對於 STM、AFM、SEM、XRD、XRL 等相關儀器設備也有六年以上的操作維護經驗，同時也有多項產學合作計畫的執行經驗，讓我獲益匪淺。而創新研究與不停學習，是個人生命成長的重要源動力。民國 91 年獲單位核准在職進修並順利考取交通大學電子物理研究所博士班就讀，經由交大奈米科技研究所教授許鈺宗博士以及交大電子物理所教授趙天生博士兩位指導教授多年來的關心照顧、悉心指導與啟發，使得敝人在專業領域上受益良多，個人並於 93 年度、94 年度及 95 年度皆榮獲國防部頒發績優國防訓儲人員獎的殊榮。近年來，從事奈米級掃描探針微影技術研發以及奈米級結構元件之研發工作。研究重點著眼於利用掃描式探針微影技術並結合 X 光微影蝕刻技術來替代高操作成本的電子束直寫系統，藉由此種先進的微影蝕刻技術可研發製作出特殊奈米級的閘極結構及元件，期許未來將能在奈米技術研發能力建置上建構一堅實的奈米生醫科技應用平台。

吳 家 豪 於交通大學

June 25, 2007

## Publications List

### (A) Journal Paper

- (01) **C. H. Wu**, J. T. Sheu, and T. S. Chao, “Scanning probe lithography of self-assembled AEAPTMS Monolayers on the SiO<sub>2</sub> surface”, Jpn. J. Appl. Phys. **46**(9B), 2007. (in press)
- (02) J. T. Sheu, **C. H. Wu**, and T. S. Chao, “Selective deposition of gold particles on DPN patterns on silicon dioxide surface”, Jpn. J. Appl. Phys. **45**(4B), pp.3693-3697, 2006.
- (03) C.-P. Li, **C. H. Wu**, K. -H. Wei, J. T. Sheu, T. Y. Huang, U. S. Jeng, and K. S. Liang, “The Effect of Nanoscale Confinement on the Collective Electron Transport Behavior in Au Nanoparticles Self-Assembled in a Nanostructured Poly(styrene-**b**-4vinylpyridine) Diblock Copolymer Ultra Thin Film”, accepted by Advanced Functional Materials, 2007. (in press)
- (04) **吳家豪**, 許鈺宗, “利用掃描式沾水筆探針微影技術研製奈米級分子層薄膜結構”, 科儀新知雜誌第 146 期 (第 26 卷第 6 期), PP.25-31, 2005.
- (05) T. Y. Cheng, **C. H. Wu**, and J. T. Sheu, “Fabrication of Nano-scaled Alumina Template Mask by Using Self - assembly Anodic Oxidation Method”, WSEAS Trans. on Electronics , Vol **1**(1) , pp.60-63, 2004..
- (06) 許鈺宗, **吳家豪**, “掃描探針顯微技術研製矽奈米結構”, 電子與材料雜誌第 18 期, pp.39-47, 2003.
- (07) J. T. Sheu, K. S. You, **C. H. Wu**, and K. M. Chang , “Single-Electron Transistor Structures Based on a SOI Silicon Nanowire Fabricated by Scanning Probe Lithography and Wet Etching”, J. Vac. Sci. Technol. B **20**(6), Nov / Dec, pp. 2824-2828, 2002.

- (08) J. T. Sheu and **C. H. Wu**, “Silicon Nanomachining by Scanning Probe Lithography and Anisotropic Wet Etching”, Chapter 8 of Microfluidics & BioMems and Materials and Process Integration, editor Francis Tay, Kluwer publishing, 2001.
- (09) B. -R. Huang, **C. H. Wu** and K. Y. Yang, “Polycrystalline diamond films for X-ray lithography mask”, Mater. Sci. Eng. B, **75**, pp. 61-67, 2000.
- (10) B. -R. Huang, **C. H. Wu** and R. F. Sheu, “The annealing effect on the electrical property of the Al/undoped diamond film”, Diamond and Related Materials 9, pp. 73-81, 2000.
- (11) B. -R. Huang, **C. H. Wu**, W. Z. Ke, “Surface analysis of boron-doped polycrystalline diamond films deposited by a microwave plasma chemical vapor deposition system”, Mater. Chem. Phys., **59**, pp. 143-148, 1999.
- (12) B. -R. Huang, J. T. Sheu and **C. H. Wu**, “Bilayer SiN<sub>x</sub>/ Diamond Films for X-ray Lithography Mask”, Jap. J. Appl. Phys., **38**(11), pp. 6530- 6534, 1999.
- (13) B. -R. Huang and **C. H. Wu**, “Electrical Conduction Mechanism of Al Contacts and Undoped Polycrystalline Diamond Films”, Jap. J. Appl. Phys., **38**(10), pp.6039-6046, 1999.
- (14) B. -R. Huang, K. Y. Yang, **C. H. Wu**, W. S. Peng, “The Oxygenated Phenomenon of the Undoped Large-Grain and Small-Grain Polycrystalline Diamond Films”, Mater. Chem. Phys., **57**(1), pp.41-46, 1998.

#### **(B) Conference Paper**

- (01) J. T. Sheu, **C. H. Wu**, P. C. Huang, and T. S. Chao, “Electrical Characteristics and Optical Responses of SiNWs with Gold Nanoparticles”, Proceedings of IEEE 2007 Silicon Nanoelectronics Workshop, Japan, 2007. (SNW 2007).
- (02) J. T. Sheu, **C. H. Wu**, and H. H. Liu, “Low Energy Electron Bond Breaking of

- Self-assembled AEAPTMS Monolayers on the SiO<sub>2</sub> Surfaces”, *accepted by the International Electron Devices & Materials Symposia 2006 (IEDMS 2006).*
- (03) J. T. Sheu, **C. H. Wu**, and T. S. Chao, “Scanning probe lithography of self-assembled AEAPTMS monolayers on the SiO<sub>2</sub> surfaces”, *accepted by the 2006 International Microprocesses and Nanotechnology Conference (MNC 2006).*
- (04) J. T. Sheu, **C. H. Wu** and T. S. Chao, “Selective deposition of gold particles on DPN patterns on silicon dioxide surface”, the International Conference on solid state devices and materials (SSDM 2005), pp.786-787, September 13-15, 2005.
- (05) J. T. Sheu, **C. H. Wu**, H. H. Liu and T. S. Chao, “Preparation of nano- scale patterns on the silicon oxide surface by dip-pen nanolithography”, IEEE-NANO 2005 Conference, 2005.
- (06) J. T. Sheu, **C. H. Wu**, H. H. Liu, W. H. Hung and T. S. Chao, “Impact of UV-induced Production of Gold nanoclusters on the Oxide Surface of Silicon Nanowires by Dip-Pen Lithography”, the 49<sup>th</sup> International Conference on Electron, Ion, and Photon Beam Technology & Nanofabrication, May 31-June 3 , Florida, USA, 2005.
- (07) **C. H. Wu**, H. H. Liu, J. T. Sheu, T. S. Chao, “Nano-scale directly patterning on silicon oxide surface by using dip-pen nanolithography technique.” The 12<sup>th</sup> Symposium on Nano Device Technology 2005, May 4-5, Hsinchu, Taiwan, 2005.
- (08) T. Y. Cheng, **C. H. Wu**, J. T. Sheu, “Fabrication of nano-scaled alumina template mask by using self-assembly anodic oxidation method”, The 4<sup>th</sup> WSEAS Int.Conf. on Nanoelectronics and Nanotechnology, (ICONN2004), January 14-16, 2004.
- (09) J. T. Sheu, S. P. Yeh, **C. H. Wu**, K. S. You and J. Y. Lin, “Fabrication of Ultrahigh-density Nanopyramid Arrays on (100) Silicon Wafer using Scanning Probe Lithography and Anisotropic etching”, ICMAT, Jun. 27~ Jul. 4, 2003.

- (10) J. T. Sheu, S. P. Yeh, **C. H. Wu**, K. S. You and J. Y. Lin, “Nano-scale Patterning of Titanium Thin Film with Local Oxidation of Scanning Probe Microscope”, ICMAT 2003, Jun. 27~ Jul. 4, 2003.
- (11) J. T. Sheu, S. P. Yeh, **C. H. Wu**, K. S. You and J. Y. Lin, “Fabrication of Ultrahigh-Density Nano-pyramid Arrays (NPAs) on (100) Silicon Wafer Using Scanning Probe Lithography and Anisotropic Wet Etching”, IEEE-NANO 2002 Conference, page 277, 2002.
- (12) J. T. Sheu, S. P. Yeh, **C. H. Wu**, K. S. You and J. Y. Lin, “Nanometer-scale patterning on titanium film with local oxidation of scanning probe microscope”, IEEE-NANO 2002 Conference, page 363, 2002.
- (13) **C. H. Wu**, J. T. Sheu, K. S. You, and K. M. Chang, “Fabrication of silicon nanowire with scanning probe lithography and wet etching process”, Symposium on Nano Device Technology 2002, May 2-3, Hsinchu, Taiwan, 2002.
- (14) J. T. Sheu, S. P. Yeh, **C. H. Wu**, and J. Y. Lin, “Nanometer-scale patterning on titanium film with local oxidation of scanning probe microscope”, Symposium on Nano Device Technology 2002, May 2-3, Hsinchu, Taiwan, 2002.
- (15) J. T. Sheu, K. S. You, **C. H. Wu**, and K. M. Chang , “Single-electron transistor structures based on a SOI silicon nanowire fabricated by scanning probe lithography and wet etching”, *accepted by the 46<sup>th</sup> International Conference on Electron, Ion, and Photon Beam Technology & Nanofabrication 2002.*